Efficient computation of the modal outgoing Green's kernel for the scalar wave equation in helioseismology

Hélène Barucq, Florian Faucher, Damien Fournier, Laurent Gizon, Ha Pham

To cite this version:

Hélène Barucq, Florian Faucher, Damien Fournier, Laurent Gizon, Ha Pham. Efficient computation of the modal outgoing Green's kernel for the scalar wave equation in helioseismology. [Research Report] RR-9338, Inria Bordeaux Sud-Ouest; Magique 3D; Max-Planck Institute for Solar System Research. 2020, pp.1-81. hal-02544701

HAL Id: hal-02544701
https://hal.science/hal-02544701v1

Submitted on 16 Apr 2020

Efficient computation of the modal outgoing Green's kernel for the scalar wave equation in helioseismology

Hélène Barucq, Florian Faucher, Damien Fournier, Laurent Gizon,
Ha Pham

ISSN 0249-6399   ISRN INRIA/RR--9338--FR+ENG

RESEARCH REPORT
N° 9338
April 2020
Project-Team Magique-3D

Efficient computation of the modal outgoing Green's kernel for the scalar wave equation in helioseismology

Hélène Barucq*, Florian Faucher†, Damien Fournier‡, Laurent Gizon‡§¶, Ha Pham*

Project-Team Magique-3D

Research Report n° 9338 — April 2020 — 81 pages

---

* Inria Project-Team Magique 3D, E2S–UPPA, CNRS, Pau, France.
† Faculty of Mathematics, University of Vienna, Oskar-Morgenstern-Platz 1, A-1090 Vienna, Austria.
‡ Max-Planck-Institut für Sonnensystemforschung, Justus-von-Liebig-Weg 3, 37077 Göttingen, Germany.
§ Institut für Astrophysik, Georg-August-Universität Göttingen, Friedrich-Hund-Platz 1, 37077 Göttingen, Germany.
¶ Center for Space Science, NYUAD Institute, New York University Abu Dhabi, PO Box 129188, Abu Dhabi, UAE.

RESEARCH CENTRE
BORDEAUX – SUD-OUEST

200 avenue de la Vieille Tour
33405 Talence Cedex

Abstract: In this project, we provide an algorithm to compute efficiently and accurately the full outgoing modal Green's kernel for the scalar wave equation in local helioseismology under spherical symmetry. The cost of computing a full Green function is well-known to be expensive and has prevented its extensive usage in local helioseismology. It is however necessary in order to interpret properly the measurements. One application is the calculation of synthetic helioseismic observables such as the cross-covariance or the power spectrum. Usually, it is supposed that the observations are coming from a single height – the "solar surface" – which requires only the Green kernel at the surface of the Sun. While yielding satisfactory comparison with helioseismic data at low frequencies, more realistic observables take into account contributions from all depths. This approach requires a full Green kernel, i.e. its values at all source and receiver depths. In this work, we propose a two-step algorithm which with two simulations gives a full kernel for each harmonic mode and frequency. Our method also accounts for the singularity of the Green kernel analytically and avoids discretization with a Dirac source directly. This feature does not only help to reduce the need for mesh refinement around the source, and but also provides more accurate values of the Green's kernel in this region. We also demonstrate numerically that using integrated simulated observables leads to a significant travel-time difference compared to using just single-depth observables. In addition, our algorithm is coupled with exact Dirichlet-to-Neumann boundary condition, thus provides optimal accuracy in approximating the outgoing Green kernel. We also evaluate the performance of the high-frequency approximations of the nonlocal radiation boundary conditions in terms of helioseismic quantities. Until now, these comparisons were only carried out under pure `Atmo` assumption, and analyzed in terms of relative error of numerical solution in the atmosphere.

Key-words: modal Green kernel, local helioseismology, solar model `S+Atmo`, solar model `Val-C`, Hybridizable Discontinuous Galerkin discretization (HDG), observables, travel-time, expected cross-covariance, power spectrum, data analysis, radiation boundary condition, Whittaker functions.

Calcul efficace du noyau de Green modal sortant pour l'équation des ondes scalaire en héliosismologie

Résumé : En héliosismologie, la fonction de Green associée à l'équation des ondes scalaire permet de représenter des observables importants tels que la corrélation croisée ou les spectres de puissance. Elle joue donc un rôle central dans l'interprétation des mesures et son calcul est crucial. Toutefois, les algorithmes de calcul existants ont des coûts de calcul encore trop élevés pour en faire une utilisation extensive en héliosismologie locale. Pour contourner cette difficulté, on suppose que les observations sont effectuées à une altitude fixe qui représente en quelque sorte une "surface solaire" et ainsi, on se contente d'utiliser la fonction de Green définie à la surface. Bien que cela donne des comparaisons satisfaisantes avec les données héliosismiques à basses fréquences, générer des observables plus réalistes demande de prendre en compte les contributions de l'intérieur du Soleil, c'est-à-dire à différentes profondeurs. Pour cela, on a besoin de la fonction de Green complète, c'est à dire, sa valeur doit être estimée pour toutes les sources et à toutes les positions de récepteurs. Dans ce travail, nous proposons un algorithme en deux étapes qui permet, à partir de seulement deux simulations, de construire le noyau de Green complet. Notre méthode prend en compte la singularité du noyau sans avoir à discrétiser la source qui est une distribution de Dirac. La méthode numérique mise en oeuvre repose sur une formulation HDG du problème écrit en supposant la symétrie sphérique du soleil. Notre algorithme est focalisé sur la partie régulière du champ d'onde et ainsi il ne nécessite pas un raffinement du maillage autour de la source tout en nous donnant des valeurs plus précises pour les récepteurs proches de la source. Nous illustrons numériquement comment l'utilisation d'intégrales pour les simulations change de façon significative le temps de trajet par rapport aux solutions à profondeur fixe.Nous effectuons des simulations pour deux modèles de Soleil qui sont couplés à une condition de radiation sortante utile pour tronquer l'atmosphère du Soleil et définir ainsi un domaine de calcul. Quand notre algorithme est couplé avec la condition aux limites Dirichlet-to-Neumann exacte, nous obtenons une précision optimale des quantités héliosismiques covariance et spectre de puissance. Nous comparons également la qualité des observables en considérant différentes approximations haute-fréquences de la condition de radiation non-locale, toujours pour le calcul des mêmes quantités héliosismiques.

Mots-clés : Noyau de Green modal, héliosismologie locale, modèle solaire `S+Atmo`, modèle solaire `Val-C`, discrétisation Galerkin hybride (HDG), observables, temps de parcours, covariance croisée, spectre de puissance, analyse de données, condition aux limites de radiation, fonctions de Whittaker.

Contents

1 Introduction

In this project, we propose an algorithm to compute efficiently and accurately the full outgoing modal Green's kernel for the scalar wave equation in local helioseismology under spherical symmetry. The goal of local helioseismology is to reconstruct the interior of the Sun from observations of oscillations of the acoustic waves at the surface due to convection. Due to the stochastic nature of the observations, the helioseismic quantities (or products) of interest are the expectation value of the cross-covariance between any two points at the surface or the power spectrum. In order to interpret the observations, one needs to define a wave equation to model the propagation of acoustic wave equation in the Sun, written as $\mathcal{L}\psi = \mathfrak{s}$; and its outgoing Green's kernel, denoted by $\mathcal{G}(\mathbf{x},\mathbf{y};\omega)$, $\mathbf{x},\mathbf{y} \in \mathbb{R}^3$, is the key ingredient to compute synthetic observables and helioseismic products, cf. Section 8 for a detailed discussion on this quantities. Spherical symmetry allows for the decomposition of $\mathcal{G}$ into spherical harmonic basis, and the task of computing the 3D kernel is parallelly decomposed into that of outgoing modal Green kernels, denoted by $\mathcal{G}_\ell(r,s;\omega)$, in terms of scaled depth[1] $r, s > 0$, for each spherical modes ℓ and frequencies ω. By the 'full' modal Green kernel, we mean the knowledge of $\mathcal{G}_\ell$ on a $[r_{\min}, r_{\max}] \times [r_{\min}, r_{\max}]$ where $r_{\min} > 0$ is numerically small and $r_{\max}$ is a height in the atmosphere.

Current results in local helioseismology assume that the Sun has a surface that is well defined, in $r = 1$, and work with simulated observables which are obtained from the solution of the wave equation at the surface of the Sun. In this approach, calculating helioseismic products requires at most[2] the values of the Green kernel for sources placed in $s = 1$, i.e. $\mathcal{G}_\ell(1, r)$. However, with the Sun being a plasma, the observed oscillations are not just coming from the "surface" but represent an average over all depths

---

[1] They are scaled by the radius of the Sun $R_\odot$ such that $r = 1$ corresponds to the position $R_\odot$.

[2] In fact, under simplifying assumption of sources, the expected value of the cross-covariance and the power spectrum are given by $\mathcal{G}_\ell(1,1)$, e.g. [3, 14]. See also discussion in Section 8.

weighted by the level of transparency (opacity). The computation of the helioseismic products now requires the full Green function as defined above. Knowledge of a full Green function is also required to interpret multi-height HMI (Helioseismic and Magnetic Imager) data [27] or to image the solar interior using helioseismic holography [35]. With its importance as explained, the full Green kernel, is well-known to be computationally expensive if the traditional method of computing the Green kernel is employed as each simulation only gives the values of the Green kernel for one fixed source position. Our proposed algorithm provides, in using only two implementations, the full Green function, for each spherical mode ℓ and frequency ω, thus in a square domain rather than just the union of two lines in the domain of definition of $\mathcal{G}_\ell$.

To develop in details the method of computation, we first specify our working equation. With the background of the Sun characterized by the density ρ and the sound speed c, both assumed to be spherically symmetric, we start our investigation with the same scalar wave equation as in [3], and denote by $\mathcal{G}$ its physical Green kernel,

$$-\nabla\cdot\left(\frac{1}{\rho(|\mathbf{x}|)}\nabla\,\mathcal{G}(\mathbf{x},\,\mathbf{y})\right)\;-\;\frac{\sigma^2(|\mathbf{x}|)}{\rho(|\mathbf{x}|)\;\mathrm{c}^2(|\mathbf{x}|)}\mathcal{G}(\mathbf{x},\,\mathbf{y})\;=\;\delta(\mathbf{x}-\mathbf{y})\,, \tag{1.1}$$

with δ the Dirac function. Here, the 'physical' property is to be determined by the conjugate problem. The quantity σ denotes the *complex frequency* and contains a model of attenuation γ such that:

$$\sigma^2(|\mathbf{x}|)\;=\;\omega^2\;+\;2\,\mathrm{i}\,\omega\,\gamma\big(|\mathbf{x}|,\omega\big)\,,\qquad\text{with } \omega>0 \text{ the angular frequency.} \tag{1.2}$$

However, similarly to [5, 4, 1], we work with conjugated equation obtained by Liouville change of unknown, since the latter offers a natural setting to define the unique *physical* (also called "outgoing" or "radiation") kernel G, solution to

$$\left(-\Delta_{\mathbf{x}}\;-\;\frac{\sigma^2(|\mathbf{x}|)}{\mathrm{c}^2(|\mathbf{x}|)}\;+\;\mathsf{q}(|\mathbf{x}|)\right)G(\mathbf{x},\,\mathbf{y})\;=\;\delta(\mathbf{x}-\mathbf{y})\,,\qquad\text{with}\quad \mathsf{q}\;:=\rho^{1/2}\,\Delta\,\rho^{-1/2}\,. \tag{1.3}$$

From G, the physical Green kernel for the original problem (1.1) is defined by

$$\mathcal{G}(\mathbf{x},\,\mathbf{y})\;:=\;\rho^{1/2}(\mathbf{x})\,\rho^{1/2}(\mathbf{y})\,G(\mathbf{x},\,\mathbf{y})\,. \tag{1.4}$$

Under spherical symmetry, where the physical parameters only depend on the radius, one works with the modal function G_ℓ, which is a fundamental solution of,

$$\left(-\frac{d^2}{dr^2}\;-\;\frac{\sigma^2(r)}{\mathrm{c}^2(r)}\;+\;\mathsf{q}(r)\;+\;\frac{\ell(\ell+1)}{r^2}\right)G_\ell\;=\;\delta(r-s)\,, \tag{1.5}$$

with $r=|\mathbf{x}|$ and s denotes the radial source position.

To obtain the modal Green function numerically, the current approach is to directly discretize (1.5) using, e.g., a finite element or finite difference method, cf. [15, 3, 8]. Since each resolution in this approach only gives the value of the Green function for a fixed source, it would thus be expensive to employ it directly to give the "complete" Green kernel which requires arbitrarily high number of sources. Additionally, unlike in applications such as seismology or inverse scattering in which one is mostly interested in the far-field or the backscattered data obtained away from the source, in helioseismology, values at the same height of the source are particularly important. However, the presence of the Dirac reduces the numerical accuracy of the response in the region around the source. To overcome this problem, one usually refines the mesh around the source when solving (1.5) leading to additional computational cost, cf. [8, 14, 3]. With solar background, it is particularly expensive, since this extra-refinement comes in addition to the one needed to capture the profile of Sun's background beneath its surface.

The procedure we propose in this work is based on a well-known formula for Green kernel of the ODE and comprises of two steps. One first obtains solutions of two boundary value problems with zero source: one regular solution in a neighborhood of the origin and an outgoing one in an exterior neighborhood. They are then 'patched together' by a Heaviside function to give the global modal Green kernel. The importance here is that while these solutions are regular, the singularity of the Green kernel is captured *exactly* by the Heaviside function. Working with only regular solutions removes the need to refine the mesh around the source position. In another word, with only two problems, one instantly obtains the value of the modal Green kernel on a rectangle region away from the origin, and thus the 3D Green kernel on a product of two punctured spheres. While the two-step procedure can be used with second-order formulation (of the wave equation), it is more compatible with a first-order formulation. In our work, the algorithm is implemented with Hybridizable Discontinuous Galerkin (HDG) discretization, which, with unknowns being the numerical trace (boundary values), provides readily the derivatives of the solution, needed for the calculation of the Wronskian in the aforementioned Green's reconstruction formula. This offers an advantage to second-order formulation which leads to a loss order of precision for the derivatives computed from values of the displacement via a high-order finite difference scheme.

A second novelty of the work is in the numerical implementation and computation of the outgoing Green's kernel, and the investigation of the influence of radiation boundary conditions (RBC) on helioseismic products for realistic background. We carry out a comparison of the RBCs obtained in [4, 5] to those in [3] for background `S+Atmo` and `S+Val-C` model in terms of power spectrum and time-distance diagram. Until now, these comparisons were only carried out under pure `Atmo` assumption, and analyzed in terms of relative error of numerical solution in the atmosphere. With the exact D-t-N coefficient as reference, our investigation reconfirms that, among the high-frequency approximations of the nonlocal RBC coefficent, those obtained in [4, 5] are more accurate than those in [3]. However, what is new in our study is the highly accentuated difference in precision order of the two families in presence of a physical background like that of the Sun. Those in [4, 5] produce helioseismic products with improved precision, with three orders of magnitude difference compared to those in [3]. In particular, our study narrows further to a comparison between $\mathbf{Z}_{\texttt{S-HF-1a}}$ and $\mathbf{Z}^{\ell}_{\texttt{A-HF-1}}$. The first one is independent of ℓ while the second one is not. Another fundamental difference is in the different wavenumbers that were used in high-frequency approximations to obtain them. Coefficients that are independent of ℓ are extremely useful, since they are first choices for RBC to be used in discretization schemes in 3D for not containing tangential differential operators. However being independent of ℓ means that in general they are expected to provide less accuracy than those dependent on ℓ. Our numerical investigations show that $\mathbf{Z}_{\texttt{S-HF-1a}}$ gives a substantial improvement compared to $\mathbf{Z}^{\ell}_{\texttt{A-HF-1}}$ in terms of helioseismic products, and thus provides a reliable RBC for future considerations with 3D discretizations.

In terms of applications in helioseismology, our work is the first to compute the complete and high-definition kernel for the solar model `S`, ([9]) with either ideal atmospheric pressure, thus called `S+Atmo`, or with atmospheric model `VAL-C` [34], called `S+VAL-C`. In particular, G_ℓ is known on $[\epsilon, r_{\max}] \times [\epsilon, r_{\max}]$ for a position $r_{\max}$ in the atmosphere in the `S+Atmo`, or in the chromosphere of the Sun for `S+VAL-C`. We also note that this is the first time, that the modal Green kernel for the `S+Atmo` model is computed using the exact Dirichlet-to-Neumann coefficient of [5]. Using this full kernel, we compute the power spectrum for harmonic modes ℓ up to 2000 and frequency up to 12 mHz. The full Green kernel also allows us to compute helioseismic products with integrated simulated observables. We demonstrate numerically that using latter type of simulated observables leads to a significant travel-time difference compared to surface observables.

The report is organized as follows. In Section 4, with justification given by the work of [2], we define the physical Green kernel G and its harmonic expansion. We also explain the basis for the two approaches using first-order system. The various RBCs are recalled and compared using the error with respect to the analytical solution in Section 5. In Section 6, the method of HDG is explained, and is validated in Section 7 using pure `Atmo` equation and its analytical solutions. In Section 7, also working with the same toy equation, we show numerical results to validate the second approach. After, a preparatory discussion to introduce the working notions and the helioseismic observables in Section 8, we compute the complete Green kernel for `S+Atmo` and `S+Val-C+Atmo` together with the resulting helioseismic products in Section 9. In this section, RBCs are compared in terms of helioseismic observables and the importance of the full Green kernel to compute helioseismic products is emphasized.

2 Preliminaries and notations

Let us give the symbols and notations used thorough the report, in particular, we place ourselves in the context of helioseismology, that is, working with solar quantities. Each quantity is specifically introduced at its first occurrence in the document.

Square root branch $(\,\cdot\,)^{1/2}$ uses the principal argument with $\mathrm{Arg}(z) \in (-\pi, \pi]$.

2.1 Physical parameters

$R_\odot$ is the radius of the Sun given in m, $R_\odot = 695\,510\,000$ m.

R is the (non-scaled) position along the Sun's radius.

r is the scaled radius, $r = R/R_\odot$.

R_a denotes the radial position (in meter) where the atmosphere begins, usually $R_a = R_\odot + 500$km.

$\mathsf{r}_a = R_a/R_\odot$ is the scaled radius where the atmosphere begins.

f is the frequency in Hz; in solar applications, the frequency typically ranges from 0 to 11 mHz.

ρ is solar density (in $\mathrm{kg\,m^{-3}}$), and $\uprho$ denotes the dimensionless density.

c is the background solar sound speed (given in $\mathrm{m\,s^{-1}}$).

$\mathfrak{c}$ is the scaled solar sound speed given in $\mathrm{s^{-1}}$, $\mathfrak{c} = \mathrm{c}/R_\odot$.

α is the inverse density scale height defined by $\alpha = -\frac{\partial_R \rho}{\rho}$ and $\upalpha$ is the dimensionless version, $\upalpha = -\frac{\partial_r \uprho}{\uprho}$.

$H = \upalpha^{-1}$ is the dimensionless density scale height.

Under the assumption that the quantities attain a limit at infinity, we define

$$\upalpha_\infty \;:=\; \lim_{r\to\infty} \upalpha(r)\,, \qquad \upalpha'_\infty \;:=\; \lim_{r\to\infty} d_r \upalpha(r)\,. \tag{2.1}$$

In particular, in the `Atmo` model,

$$\upalpha_\infty = 6663.62\,, \qquad \upalpha'_\infty = 0\,. \tag{2.2}$$

This value of α_∞ is also used in [3, Section 4.3.3].

2.2 Representation of the attenuation

The attenuation is encoded in (1.1) with the complex frequency σ, specifically with the term γ. In the context of the solar scalar waves, it can for instance be taken as a constant with

$$\frac{\gamma}{2\pi} \;=\; 20\,\mu\mathrm{Hz}\,, \qquad \text{constant solar attenuation.} \tag{2.3}$$

As an alternative, it can be represented with the power law [15, Eq. (79)] such that

$$\gamma(\omega) = \gamma_0 \left|\frac{\omega}{\omega_0}\right|^{\beta}\,. \tag{2.4}$$

In [3, Eq. (4.14)], this formula is employed with

$$\frac{\gamma_0}{2\pi} = 8.58\mu\mathrm{Hz}\,, \qquad \frac{\omega_0}{2\pi} = 3\mathrm{mHz}\,, \qquad \beta = 5.77\,. \tag{2.5}$$

While ω_0 and β remains the same in [15, Eq. (79)], γ_0 takes the value

$$\frac{\gamma_0}{2\pi} = 4.29\mu\mathrm{Hz}\,. \tag{2.6}$$

2.3 Legendre functions

Legendre functions are solutions to the *Legendre differential equations*

$$\frac{d}{dt}\,(1-t^2)\,\frac{d}{dt}\,P \;+\; \ell(\ell+1)\,P \;=0. \tag{2.7}$$

Solutions that are polynomials of degree ℓ in t are call the *Legendre polynomials* and denoted by $P_\ell(t)$. They are given by, cf. [25, Theorem 9.9]

$$\boxed{\mathrm{P}_\ell(t) \;=\; \frac{(-1)^\ell}{2^\ell\,\ell!}\,\frac{d^\ell}{dt^\ell}\,(1-t^2)^\ell \;=\; \frac{1}{2^\ell\,\ell!}\,\frac{d^\ell}{d\,t^\ell}(t^2-1)^\ell\,, \qquad \ell=0,1,2,\ldots} \tag{2.8}$$

They have the orthogonality property,

$$\int_{-1}^{1}\mathrm{P}_n(t)\,\mathrm{P}_m(t)\,dt \;=\; \frac{2}{2n+1}\,\delta_{nm}\,. \tag{2.9}$$

They also satisfy the recursive relation, cf. [29, Eqn 1.119 p. 22],

$$(\ell+1)\,P_{\ell+1}(t) \;-\; (2\ell+1)\,t\,\mathrm{P}_\ell(t) \;+\; \ell\,\mathrm{P}_{\ell-1}(t) \;=\; 0 \quad,\quad \ell=1,2, \tag{2.10}$$

and

$$\mathrm{P}_0(t)=1 \quad,\quad \mathrm{P}_1(t)=t\,. \tag{2.11}$$

Thus

$$\mathrm{P}_\ell(1) \;=\; 1 \quad,\quad \mathrm{P}_\ell(-t) \;=\; (-1)^\ell\,\mathrm{P}_\ell(t) \quad\Rightarrow\quad \mathrm{P}_\ell(-1) \;=\; (-1)^\ell\,. \tag{2.12}$$

We will also need the following result:

$$\boxed{\frac{1}{(4\pi)^2}\sum_\ell\sum_{\ell'}(2\ell+1)(2\ell'+1)\int \mathrm{P}_\ell(\cos\theta_{\hat{\boldsymbol{r}}_1\cdot\hat{\boldsymbol{r}}})\mathrm{P}_{\ell'}(\cos\theta_{\hat{\boldsymbol{r}}_2\cdot\hat{\boldsymbol{r}}})d\hat{\boldsymbol{r}} = \sum_\ell\frac{2\ell+1}{4\pi}\mathrm{P}_\ell(\cos\theta_{\hat{\boldsymbol{r}}_1\cdot\hat{\boldsymbol{r}}_2}).} \tag{2.13}$$

Proof. To prove it, we use the addition theorem of spherical harmonics (2.27) (twice) and the orthonormality of the spherical harmonics (2.26)

$$\frac{1}{(4\pi)^2}\sum_\ell\sum_{\ell'}(2\ell+1)(2\ell'+1)\int \mathrm{P}_\ell(\cos\theta_{\hat{\boldsymbol{r}}_1\cdot\hat{\boldsymbol{r}}})\mathrm{P}_{\ell'}(\cos\theta_{\hat{\boldsymbol{r}}_2\cdot\hat{\boldsymbol{r}}})d\hat{\boldsymbol{r}} \tag{2.14}$$

$$=\sum_\ell\sum_{\ell'}\sum_m\sum_{m'}\overline{\mathrm{Y}_\ell^m(\theta_1,\phi_1)}\mathrm{Y}_{\ell'}^{m'}(\theta_2,\phi_2)\int\overline{\mathrm{Y}_\ell^m(\theta,\phi)}\mathrm{Y}_{\ell'}^{m'}(\theta,\phi)\sin\theta d\theta d\phi \tag{2.15}$$

$$=\sum_\ell\sum_m\overline{\mathrm{Y}_\ell^m(\theta_1,\phi_1)}\mathrm{Y}_\ell^m(\theta_2,\phi_2) \tag{2.16}$$

$$=\sum_\ell\frac{2\ell+1}{4\pi}\mathrm{P}_\ell(\cos\theta_{\hat{\boldsymbol{r}}_1\cdot\hat{\boldsymbol{r}}_2}). \tag{2.17}$$

□

The *associated Legendre functions*, or *Ferrer's functions* are defined as, cf. [29, Eq. (1.138) p. 24] or [25, Section 9.3.1 p. 238],

$$\boxed{\mathrm{P}_\ell^m(t) \;:=\; (1\;-\;t^2)^{m/2}\,\frac{d^m}{dt^m}\mathrm{P}_\ell(t)\,,\quad m=0,1,\ldots,\ell} \tag{2.18}$$

From [29, Eqn. (1.147) p. 24], we have

$$\|\mathrm{P}_\ell^m(\cdot)\|^2_{L^2([-1,1])} \;=\; \int_{-1}^{1}(\mathrm{P}_\ell^m(t))^2\,dt \;=\; \frac{(\ell\,+\,m)!}{(\ell\,+\,\frac{1}{2})\,(\ell-m)!}\,. \tag{2.19}$$

Thus one can introduce the normalized version

$$\mathrm{N}_\ell^m(t) \;:=\; \frac{\mathrm{P}_\ell^m(t)}{\|\mathrm{P}_\ell^m(\cdot)\|_{L^2([-1,1])}} \tag{2.20}$$

thus

$$\boxed{\mathrm{N}_\ell^m(t) \;=\; \sqrt{\frac{(\ell+\frac{1}{2})\,(\ell-m)!}{(\ell+m)!}}\,\mathrm{P}_\ell^m(t) \;=\; \sqrt{\frac{(\ell+\frac{1}{2})\,(\ell-m)!}{(\ell+m)!}}\;(1\;-\;t^2)^{m/2}\,\frac{d^m}{dt^m}\mathrm{P}_\ell(t)\,.} \tag{2.21}$$

Remark 1 (Comparison with Legendre definition in `Matlab`)**.** *This is taken from* `https://fr.mathworks.com/help/matlab/ref/legendre.html`

1. *The definition of Legendre polynomial* P_ℓ *in* **`Matlab`** *agrees with* (2.8)*.*
2. *However, for the* associated Legendre function*, it is different from* (2.18) *by* $(-1)^m$*. The* **`Matlab`** *associated Legendre* $[\mathrm{P}_n^m]_{\texttt{Matlab}}(t)$ *is computed by the intrinsic function* **`legendre(n,X)`** *which gives for all values of* $m=0,1,\ldots,n$*,*

$$[\mathrm{P}_\ell^m]_{\texttt{Matlab}}(t) \;:=\; (-1)^m\,(1\;-\;t^2)^{m/2}\,\frac{d^m}{dt^m}\mathrm{P}_\ell(t)\,, \qquad m=0,1,\ldots,\ell \tag{2.22}$$

   thus

$$[\mathrm{P}_\ell^m]_{\texttt{Matlab}}(t) \;=\; (-1)^m\,\mathrm{P}_\ell^m(t)\,.$$

3. *For their (fully) normalized associated Legendre function, the* **`Matlab`** *intrinsic function puts back* $(-1)^m$*, leading to the same definition*

$$[\mathrm{N}_\ell^m]_{\texttt{Matlab}}(t) \;=\; (-1)^m\sqrt{\frac{(\ell+\frac{1}{2})\,(\ell-m)!}{(\ell+m)!}}\,[\mathrm{P}_\ell^m]_{\texttt{Matlab}}(t) \;=\; \sqrt{\frac{(\ell+\frac{1}{2})\,(\ell-m)!}{(\ell+m)!}}\,(1\;-\;t^2)^{m/2}\,\frac{d^m}{dt^m}\mathrm{P}_\ell(t)\,. \tag{2.23}$$

   thus

$$[\mathrm{N}_\ell^m]_{\texttt{Matlab}}(t) \;=\; \mathrm{N}_\ell^m(t)$$

   This is obtained in **`Matlab`** *by calling the intrinsic function* **`legendre(n,X,‘norm’)`***.* △

2.4 Spherical harmonics

We denote the spherical coordinates by (r,θ,ϕ) with $0\leq\theta\leq\pi$ the colatitude angle, while $0\leq\phi\leq 2\pi$ is the longitudinal angle. The m-th *spherical harmonic* function of order ℓ is defined as [28, 14.30.1], see also [11, Theorem 2.7] or [25, Eqn. 9.37 p. 238],

$$\boxed{\begin{gathered}\mathrm{Y}_\ell^m(\theta,\phi) \;:=\; \mathrm{N}_\ell^m(\cos\theta)\,\frac{e^{\mathrm{i}\,m\,\phi}}{\sqrt{2\pi}} \;=\; \sqrt{\frac{(2\ell+1)}{4\pi}\,\frac{(\ell-|m|)!}{(\ell+|m|)!}}\;\mathrm{P}_\ell^{|m|}(\cos\theta)\;e^{\mathrm{i}\,m\,\phi}\\ m=-\ell,\ldots,\ell\,,\quad \ell=0,1,2,\ldots\end{gathered}} \tag{2.24}$$

where P_ℓ^m are the *associated Legendre functions* defined in (2.18). They satisfy

$$\Delta_{\mathbb{S}^1}\,\mathrm{Y}_\ell^m \;=\; -\ell(\ell+1)\,\mathrm{Y}_\ell^m\,. \tag{2.25}$$

The $\{\mathrm{Y}_\ell^m\}_{\substack{m=-\ell,\ldots,\ell\\ \ell=0,1,2,\ldots}}$ form a complete orthononal system in $L^2(\mathbb{S}^2)$, cf. [25, Theorem 9.11 p. 238],

$$\int_{\mathbb{S}^1}\mathrm{Y}_n^m(\hat{\mathbf{x}})\,\overline{\mathrm{Y}_{\tilde{n}}^{\tilde{m}}(\hat{\mathbf{x}})}\,\mathrm{d}\sigma_{\mathbb{S}^1}(\hat{\mathbf{x}}) \;=\; \delta_{m\tilde{m}}\,\delta_{n\tilde{n}}\,, \tag{2.26}$$

where we note that $d\sigma_{\mathbb{S}^1}=\sin\theta\,d\phi\,d\theta$.

In this report, we use the following properties of the spherical harmonics

- the addition theorem, cf. [11, 2.29],

$$\boxed{\sum_{m=-\ell}^{\ell} \mathrm{Y}_\ell^m(\theta_{\mathbf{x}},\phi_{\mathbf{x}})\,\overline{\mathrm{Y}_\ell^m(\theta_{\mathbf{y}},\phi_{\mathbf{y}})} \;=\; \frac{2\ell+1}{4\pi}\mathrm{P}_\ell(\cos\theta_{\mathbf{x}\cdot\mathbf{y}})\,,} \tag{2.27}$$

where $\theta_{\mathbf{x}\cdot\mathbf{y}}$ is the angle between $\mathbf{x}$ and $\mathbf{y}$, i.e.

$$\cos\theta_{\mathbf{x}\cdot\mathbf{y}} \;=\; \frac{\mathbf{x}\cdot\mathbf{y}}{|\mathbf{x}|\,|\mathbf{y}|}\,. \tag{2.28}$$

- the Gaunt formula [13, 4.6.3] in order to compute the integral of the product of three spherical harmonics

$$\mathrm{Gaunt}(\ell,\ell',\ell'',m,m',m'') := \int_{\mathbb{S}^1} \mathrm{Y}_\ell^m(\hat{\boldsymbol{r}})\mathrm{Y}_{\ell'}^{m'}(\hat{\boldsymbol{r}})\mathrm{Y}_{\ell''}^{m''}(\hat{\boldsymbol{r}})\,\mathrm{d}\sigma_{\mathbb{S}^1}(\hat{\boldsymbol{r}}) \tag{2.29}$$

$$= \frac{4\pi}{\alpha_\ell\alpha_{\ell'}\alpha_{\ell''}} \begin{pmatrix} \ell & \ell' & \ell'' \\ 0 & 0 & 0 \end{pmatrix} \begin{pmatrix} \ell & \ell' & \ell'' \\ m & m' & m'' \end{pmatrix}, \tag{2.30}$$

where $\alpha_\ell = \sqrt{4\pi/(2\ell+1)}$ and the terms in parenthesis correspond to the Wigner-3j symbol, see e.g. [13, p. 45]. The Wigner-3j is non-zero only if $m'' = -m - m'$ and $|\ell-\ell'| < \ell'' < \ell+\ell'$.

2.5 Whittaker functions

For $\ell = 0, 1, 2, \ldots$, we consider a subclass of *Whittaker* functions which are solutions to

$$\partial_z^2 W \;+\; \Big(-\frac{1}{4} + \frac{\kappa}{z} + \frac{\frac{1}{4} - (\frac{1}{2}+\ell)^2}{z^2}\Big) W \;=\; 0\,, \qquad \kappa\in\mathbb{C}\,,\, \mu\in\mathbb{C}\,. \tag{2.31}$$

A fundamental pair of solutions to (2.31) in an unbounded domain is given by the *second Whittaker functions* W,

$$\mathrm{W}_{\kappa,\ell+\frac{1}{2}}(z)\,, \qquad \mathrm{W}_{-\kappa,\ell+\frac{1}{2}}(e^{-\mathrm{i}\pi}z)\,, \qquad -\tfrac{\pi}{2} \leq \mathrm{Arg}(z) < \tfrac{3\pi}{2}\,. \tag{2.32}$$

On the other hand, a fundamental pair of solutions near origin $\mathcal{M}$ and W,

$$\mathcal{M}_{\kappa,\ell+\frac{1}{2}}(z)\,, \qquad \mathrm{W}_{\kappa,\ell+\frac{1}{2}}(z)\,, \qquad |\mathrm{Arg}\,z| \leq \pi\,, \tag{2.33}$$

are defined with,

$$\mathcal{M}_{\kappa,\ell+\frac{1}{2}}(z) \;:=\; e^{-\frac{1}{2}z}\, z^{\ell+1} \frac{1}{\Gamma(2\ell+2)} \sum_{k=0}^{\infty} \frac{(\ell+1-\kappa)_k}{(2\ell+2)_k} \frac{z^k}{k!}\,, \tag{2.34}$$

and for κ with $\kappa-\ell-1 \neq 0, 1, 2, \ldots$, cf. [28, 13.14.8],

$$\begin{aligned} \mathrm{W}_{\kappa,\ell+\frac{1}{2}}(z) \;=\; -\frac{e^{-\frac{1}{2}z}\, z^{\ell+1}}{(2\ell+1)!\;\Gamma(-\ell-\kappa)} \Bigg(\sum_{k=1}^{2\ell+1} \frac{(2\ell+1)!\;(k-1)!}{(2\ell+1-k)!\;(\kappa-\ell)_k}\, z^{-k} \\ - \sum_{k=0}^{\infty} \frac{(\ell+1-\kappa)_k}{(2\ell+2)_k\;k!}\, z^k\, \big[\ln z \;+\; \boldsymbol{\psi}(\ell+1-\kappa+k) \;-\; \boldsymbol{\psi}(1+k) \;-\; \boldsymbol{\psi}(2\ell+2+k)\big]\Bigg). \end{aligned} \tag{2.35}$$

$\mathcal{M}$ is referred to as the *regular Whittaker* $\mathcal{M}$ or the *Buchholtz function* $\mathcal{M}$. It is the regular version of the second Whittaker function[3],

$$\mathcal{M}_{\kappa,\ell+\frac{1}{2}}(z) \;=\; \frac{\mathrm{M}_{\kappa,\ell+\frac{1}{2}}(z)}{\Gamma(2\ell+2)} \;=\; \frac{\mathrm{M}_{\kappa,\ell+\frac{1}{2}}(z)}{(2\ell+1)!}\,. \tag{2.36}$$

---

[3] It is what is given by the intrinsic `Matlab` routine `whittakerM(a,b,z)`.

The derivative of $\mathrm{M}_{\kappa,\mu}$ and $\mathrm{W}_{\kappa,\mu}$ can be obtained by the following connection formulae, [4],

$$\mathrm{M}'_{\kappa,\ell+1/2}(z) \;=\; \left(-\frac{1}{2} \,-\, \frac{\ell}{z}\right)\mathrm{M}_{\kappa,\ell+1/2}(z) \,+\, \frac{(2\ell+1)}{\sqrt{z}}\,\mathrm{M}_{\kappa-\frac{1}{2},\ell}(z)\,; \tag{2.37a}$$

$$\mathrm{W}'_{\kappa,\ell+1/2}(z) \;=\; \left(\frac{1}{2} \,-\, \frac{\ell}{z}\right)\mathrm{W}_{\kappa,\ell+1/2}(z) \,-\, \frac{1}{\sqrt{z}}\,\mathrm{W}_{\kappa+\frac{1}{2},\ell}(z)\,; \tag{2.37b}$$

$$\mathrm{W}'_{\kappa,\ell+1/2}(z) \;=\; \left(\frac{1}{2} \,-\, \frac{\kappa}{z}\right)\mathrm{W}_{\kappa,\ell+1/2}(z) \,-\, \frac{1}{z}\,\mathrm{W}_{\kappa+1,\ell+1/2}(z)\,. \tag{2.37c}$$

Further discussions are given in Appendix B.1.

3 Conjugate wave equation with dimensionless coefficients

We choose 3D coordinate system with the Sun placed at the origin, and denoted by $\check{\mathbf{x}}$ positions in this system. With $R_\odot$ denoting the radius of the Sun, we introduced the scaled coordinates,

$$\mathbf{x} \;=\; \frac{\check{\mathbf{x}}}{R_\odot}\,, \qquad R = |\check{\mathbf{x}}|\,. \tag{3.1}$$

We have

$$\nabla_{\mathbf{x}} \;=\; R_\odot \nabla_{\check{\mathbf{x}}}\,. \tag{3.2}$$

We introduce scaled radius which is dimensionless,

$$r = \frac{R}{R_\odot}\,. \tag{3.3}$$

Define associated density function

$$r \;\mapsto\; \mathsf{\rho}(r) \;=\; \rho(R_\odot\, r)\,. \tag{3.4}$$

The dimensionless inverse density scale height is defined by

$$\mathsf{\alpha}(r) \;:=\; -\frac{\partial_r \mathsf{\rho}(r)}{\mathsf{\rho}(r)}\,. \tag{3.5}$$

The dimensionless density scale follows:

$$H(r) \;:=\; \mathsf{\alpha}^{-1}\,. \tag{3.6}$$

Since $\partial_r = R_\odot \partial_R$, in comparing $\mathsf{\alpha}$ to α defined by

$$\alpha(R) \;:=\; -\frac{\partial_R\, \rho(R)}{\rho(R)}\,, \tag{3.7}$$

which is of unit m^{-1}, we have

$$\partial_r \mathsf{\rho} \;=\; \frac{R_\odot}{\mathfrak{c}_\rho}\,\partial_r \rho \quad\Rightarrow\quad \alpha \;=\; -\frac{\partial_R \rho}{\rho} \;=\; \frac{\mathfrak{c}_\rho}{R_\odot}\,\frac{\partial_r \mathsf{\rho}}{\mathfrak{c}_\rho\, \mathsf{\rho}} \;=\; \frac{1}{R_\odot}\,\mathsf{\alpha}\,. \tag{3.8}$$

In using the scaled sound speed

$$\mathfrak{c} \;:=\; \frac{\mathrm{c}}{R_\odot}, \tag{3.9}$$

we render dimensionless the quantity

$$\frac{\sigma}{\mathfrak{c}}\,. \tag{3.10}$$

3.1 Original problem

We recall the main equation

$$-\nabla\cdot\left(\frac{1}{\rho}\nabla\,\check{\mathfrak{u}}\right)\;-\;\frac{\sigma^2}{\rho\,c^2}\,\check{\mathfrak{u}}\;=\;\check{\mathfrak{f}}\,,\qquad\text{with}\quad\sigma^2\;=\;\omega^2\,+\,2\,\mathrm{i}\,\omega\,\gamma\,. \tag{3.11}$$

We first write the field $\mathfrak{u}$ and the right-hand side $\check{\mathfrak{f}}$ in terms of the scaled radius:

$$\mathfrak{u}(\mathbf{x})\;:=\;\check{\mathfrak{u}}(R_\odot\,\mathbf{x})\,,\qquad\mathfrak{f}(\mathbf{x})\;:=\check{\mathfrak{f}}(R_\odot\,\mathbf{x}). \tag{3.12}$$

Using (3.2), we have

$$-\frac{1}{R_\odot^2}\nabla\cdot\left(\frac{1}{\uprho}\nabla\,\mathfrak{u}\right)\;-\;\frac{\sigma^2}{\uprho\,(\mathfrak{c}\,R_\odot)^2}\,\mathfrak{u}\;=\;\mathfrak{f}\,. \tag{3.13}$$

Multiply both sides with $R_\odot^2$, we obtain

$$-\nabla\cdot\left(\frac{1}{\uprho}\nabla\,\mathfrak{u}\right)\;-\;\frac{\sigma^2}{\uprho\,\mathfrak{c}^2}\,\mathfrak{u}\;=\;R_\odot^2\,\mathfrak{f}\,. \tag{3.14}$$

3.2 Conjugated problem with dimensionless coefficients

Similarly to [5], we work with the *conjugated* problem by introducing the change of unknown,

$$u(\mathbf{x})\;=\;\uprho^{-1/2}\,\mathfrak{u}(\mathbf{x})\,. \tag{3.15}$$

We define the dimensionless potential q,

$$\mathsf{q}(\mathbf{x})\;:=\;\uprho^{1/2}\,\Delta_{\mathbf{x}}\,\uprho^{-1/2}\,. \tag{3.16}$$

The conjugated equation with dimensionless coefficients is

$$\boxed{-\Delta_{\mathbf{x}}u\;-\;\frac{\sigma^2}{\mathfrak{c}^2}\,u\;+\;\mathsf{q}\,u\;=\;g\,,} \tag{3.17}$$

with right-hand-side

$$g\;=\;\uprho^{1/2}R_\odot^2\,\mathfrak{f}\,. \tag{3.18}$$

4 Discussion on Green function

While the original equation is given in (1.1) and (3.14), we work with the conjugated version, given in (3.17) in three dimensions after adimensionalization. Then, following the spherical symmetry, the solution is decomposed onto the one-dimensional *modal* ones, over the domain $[0,\,r_{\max}]$, with $r_{\max}>1$, using the adimensionalized version where the position $r=1$ corresponds with the Sun's "surface". In terms of boundary conditions, a Neumann-like one holds in 0, cf. Section 4, while radiation boundary conditions are imposed in $r_{\max}$, [3, 5].

Denote the Green kernel of the original problem with dimensionless coefficients by

$$\left(-\nabla_{\mathbf{x}}\cdot(\uprho^{-1}\nabla_{\mathbf{x}}u)\;-\;\frac{\sigma^2}{\uprho\,\mathfrak{c}^2}\right)\mathcal{G}(\mathbf{x},\mathbf{s})\;=\;\delta(\mathbf{x}-\mathbf{s})\,, \tag{4.1}$$

and that of the conjugate problem by,

$$\left(-\Delta_{\mathbf{x}}\;-\;\frac{\sigma^2(r)}{\mathfrak{c}^2(r)}\;+\;\mathsf{q}\right)G\;=\;\delta(\mathbf{x}-\mathbf{s}) \tag{4.2}$$

with

$$\mathsf{q}(r) \;=\; \frac{\alpha^2(r)}{4} \,+\, \frac{\alpha'(r)}{2} \,+\, \frac{\alpha(r)}{r}\,. \tag{4.3}$$

They are related by

$$\boxed{\mathcal{G}(\mathbf{x},\mathbf{y}) \;=\; \rho^{1/2}(\mathbf{x})\,\rho^{1/2}(\mathbf{y})\,G(\mathbf{x},\mathbf{y})\,.} \tag{4.4}$$

For more details on the transformation, cf. e.g. [5, 1] and [4, Appendix a].

Assumption 1. *The sound speed $\mathfrak{c}$ and attenuation coefficient γ are bounded functions, which are constant outside of a compact set with $\mathfrak{c}_\infty$ and γ_∞ denoting their respective values on the exterior domain. We assume that*

$$\mathrm{Supp}\,(\mathfrak{c}-\mathfrak{c}_\infty) \qquad \textit{is compact} \qquad \textit{(Assumption 1a)}\,, \tag{4.5a}$$

$$\mathrm{Supp}\,(\gamma-\gamma_\infty) \qquad \textit{is compact} \qquad \textit{(Assumption 1b)}\,. \tag{4.5b}$$

Assumption 2. *We assume that the background density ρ is such that $\alpha = -\rho'/\rho$ satisfies*

$$\begin{aligned} \alpha(r) \,&\in\, \mathcal{C}^1(\mathbb{R}_+) \,\cap\, L^\infty(\mathbb{R}_+)\,, \qquad && \lim_{r\to\infty} \alpha \;=\; \alpha_\infty\,, \\ \textit{and} \quad \alpha'(r) \;&=\; (1\,+\,r)^{-(1+\epsilon)}\,, && \epsilon > 0. \end{aligned} \tag{4.6}$$

Note that the background quantities $\mathfrak{c}$ and ρ for the Sun using model `S+Atmo` or `S+Val-C+Atmo` satisfy these assumptions. Under Assumption 2, the potential q has a finite limiting value denoted by q_∞, such that

$$\lim_{r\to\infty} \mathsf{q} \;=\; \mathsf{q}_\infty \;=\; \frac{\alpha_\infty^2}{4}\,. \tag{4.7}$$

Assumption 3. *As r tends to 0, we assume that*

$$\lim_{r\to 0}\, r^2 \left(\frac{\sigma^2(r)}{\mathfrak{c}^2(r)} \,+\, \mathsf{q}(r) \right) \;=\; 0. \tag{4.8}$$

Under Assumptions 1 to 3, we can apply the result of [2, Theorem 6.2] to obtain the physical Green kernel. To state the proposition, we introduce the following notation. Define potential Q_ℓ,

$$\frac{Q_\ell(r)}{r^2} \;=\; -\frac{\sigma^2(r)}{\mathfrak{c}^2(r)} \,+\, \mathsf{q}(r) \,+\, \frac{\ell(\ell+1)}{r^2} \;=\; -\frac{\sigma^2(r)}{\mathfrak{c}^2(r)} \,+\, \frac{\alpha^2(r)}{4} \,+\, \frac{\alpha'(r)}{2} \,+\, \frac{\alpha(r)}{r} \,+\, \frac{\ell(\ell+1)}{r^2}\,, \tag{4.9}$$

and operator L_ℓ,

$$\mathsf{L}_\ell \;:=\; -\frac{d^2}{dr^2} \,+\, \frac{Q(r)}{r^2} \;=\; -\frac{d^2}{dr^2} \,-\, \frac{\sigma^2(r)}{\mathfrak{c}^2(r)} \,+\, \mathsf{q}(r) \,+\, \frac{\ell(\ell+1)}{r^2}\,. \tag{4.10}$$

Proposition 1 (Expansion of Green kernel)**.** *Under Assumption 1–Assumption 3, the Schwartz's kernel G of the resolvent $\mathcal{R} \;:=\; (-\Delta - \kappa^2 + \mathsf{q})^{-1}$ can be written as an expansion in spherical harmonic basis with*

$$G(\mathbf{x}\,,\,\mathbf{y}) \;=\; \frac{1}{|\mathbf{x}|\,|\mathbf{y}|} \sum_{\ell=0}^{\infty} \sum_{m=-\ell}^{\ell} G_\ell^m(|\mathbf{x}|\,,|\,\mathbf{y}|)\; \mathrm{Y}_\ell^m(\hat{\mathbf{y}})\; \overline{\mathrm{Y}_\ell^m(\hat{\mathbf{x}})}\,, \qquad \mathbf{x},\mathbf{y} \textit{ not on the z-axis} \tag{4.11a}$$

$$\overset{(2.27)}{=} \;\frac{1}{4\,\pi\,|\mathbf{x}|\,|\mathbf{y}|} \sum_{\ell=0}^{\infty} (2\ell\,+\,1)\; G_\ell(|\mathbf{x}|\,,|\,\mathbf{y}|)\,\mathrm{P}_\ell(\cos\theta_{\mathbf{x}\cdot\mathbf{y}})\,, \tag{4.11b}$$

where $G_\ell^m(r,s) = G_\ell$, i.e., independent of m, is the unique distributional solution to

$$\mathsf{L}_\ell\, G_\ell \;=\; \delta(r-s)\,, \tag{4.12}$$

satisfying the boundary condition,

$$\lim_{r\to 0} \, r^{-(\ell+1)} \, G_\ell(r) \,=\, 1\,, \tag{4.13}$$

at $r=0$, and the asymptotic relation at infinity,

$$G_\ell \,=\, e^{\mathrm{i}\varphi(r,\mathsf{k})}\,\big(1 \,+\, \mathsf{o}(1)\big) \qquad \text{as } r \to \infty\,. \tag{4.14}$$

In (4.14), the phase function is defined for some $r_0 > 0$ as,

$$\varphi(r) \,:=\, \int_{r_0}^{r} \sqrt{\mathsf{k}^2 \,-\, \frac{\alpha}{s}}\,\mathrm{d}s \,=\, \mathsf{k}r \,-\, \frac{\alpha}{2\mathsf{k}}\,\log r \,+\, \mathsf{k}^{-2}\mathsf{o}(1)\,, \tag{4.15}$$

where

$$\mathsf{k} \,=\, \sqrt{\frac{\sigma^2}{\mathfrak{c}_\infty^2} \,-\, \frac{\alpha_\infty^2}{4}}\,. \tag{4.16}$$

Furthermore, if $\tilde{\psi}_\ell$ and ψ_ℓ are two homogeneous solutions to $\mathsf{L}_\ell w \,=\, 0$ on $(0,s)$ and (s,∞) respectively with $\tilde{\psi}_\ell$ satisfying BC (4.13) at $r=0$, and ψ_ℓ condition (4.14) as $z\to\infty$, we have

$$G_\ell^m(r,s) \,=\, \frac{-\mathrm{H}(s-r)\,\psi(r)\,\tilde{\psi}(s) \,-\, \mathrm{H}(r-s)\,\tilde{\psi}(r)\,\psi(s)}{\mathcal{W}(s)}\,. \tag{4.17}$$

Here, H *denoting the Heaviside function and $\mathcal{W}(s) := \mathcal{W}\{\psi(s),\tilde{\psi}(s)\}$, denotes the Wronskian.*

4.1 Remarks on boundary conditions

4.1.1 Boundary condition at zero

Using the Frobenius theory, e.g. [10, Theorem 4 p.165], the indicial equation at $r=0$ for (4.10) is,

$$\lambda^2 \,+\, \lambda \,+\, \lim_{r\to 0} r^2 \left(\frac{\sigma^2(r)}{\mathfrak{c}^2(r)} \,+\, \mathsf{q}(r)\right) \,+\, \ell(\ell+1) \,=\, 0\,. \tag{4.18}$$

Under assumption (4.8), this simplifies to

$$\lambda^2 \,-\, \lambda \,-\, \ell(\ell+1) \,=\, 0 \qquad \Rightarrow \qquad \lambda = -\ell \quad \text{or} \quad \lambda = \ell+1\,. \tag{4.19}$$

The regular solution at $r=0$ is given by $\lambda = \ell+1$, which explains the boundary condition (4.13). In the case of (4.8), or other regular singular ODE with indicial roots of opposite signs, (4.13) can be replaced by the boundary condition

$$\lim_{r\to 0} \, r\,\frac{d}{dr}\left(\frac{G_\ell(r)}{r}\right) \,=\, 0\,, \tag{4.20}$$

which also selects the regular solution at $r=0$. This can be seen as follows.

A generic solution on the neighborhood of zero is a linear combination of a function that decays in $r^{\ell+1}$ and one that blows up in $r^{-\ell}$; in particular, cf. [10, Theorem 4 p.165],

$$w(r) \,=\, \mathsf{a}\,\left(r^{-\ell}\,h(r) \,+\, \mathsf{c}\,(\log r)\,r^{\ell+1}\,g(r)\right) \,+\, \mathsf{b}\,r^{\ell+1}\,g(r) \quad , \quad r>0\,, \tag{4.21}$$

for some constants a,b and c, and functions $g(r)$ and $h(r)$ which are C^1 up to $r=0$ with $g(0)\neq 0$, and $h(0)\neq 0$. The presence of the log term is due to the integral difference of the two indicial exponents, i.e. $(\ell+1)-(-\ell)\in\mathbb{N}$. We have

$$\begin{aligned} r\,\frac{d}{dr}\frac{w}{r} \,=\, &\mathsf{a}\,\left((-\ell-1)\,r^{-\ell-1}\,h(r) \,+\, \mathsf{c}\,r^{\ell}\,g(r) \,+\, (\ell)\,\mathsf{c}\,(\log r)\,r^{\ell}\,g(r)\right) \,+\, \mathsf{b}\,\ell\,r^{\ell}\,g(r) \\ &+\, \mathsf{a}\,\left(r^{-\ell}\,h'(r) \,+\, \mathsf{c}\,(\log r)\,r^{\ell+1}\,g'(r)\right) \,+\, \mathsf{b}\,r^{\ell+1}\,g'(r)\,. \end{aligned} \tag{4.22}$$

For w of the form (4.21), in order for $\lim_{r\to 0} r\,(w(r)/r)' < \infty$, the constant a has to be zero. In fact, (4.20) is a stronger condition, and requires that this finite value is exactly zero, which is indeed satisfied by w of the form (4.21) with $\mathsf{a} = 0$,

$$\lim_{r\to 0} r\left(\frac{w(r)}{r}\right)' \;=\; \lim_{r\to 0}\left(\mathsf{b}\,\ell\,r^{\ell}\,g(r) \;+\; \mathsf{b}\,r^{\ell+1}\,g'(r)\right) \;=\; 0 \quad , \quad \ell \geq 0\,. \tag{4.23}$$

Remark 2. *One can also consider a condition such that* $\lim_{r\to 0} r^2 (w/r)' < \infty$*, which also selects the regular family, i.e. which forces* $\mathsf{a} = 0$ *when* $\ell > 0$*. However, unlike the condition* $\lim_{r\to 0} r(w/r)' < \infty$*, this condition does not imply* $\mathsf{a} = 0$ *at* $\ell = 0$*; in another word, it admits both the regular and singular families,*

$$r^2\,\frac{d}{dr}\frac{w}{r} \;=\; \mathsf{a}\,\left((-1)\,h(r) \;+\; \mathsf{c}\,r\,g(r)\right) \;+\; \mathsf{a}\,\left(r\,h'(r) \;+\; \mathsf{c}\,(\log r)\,r^2\,g'(r)\right) \;+\; \mathsf{b}\,r^2\,g'(r)\,. \tag{4.24}$$

However, in using $h(0) \neq 0$*, then the stronger condition* $\lim_{r\to 0} r^2(w/r)' = 0$ *still rules out the singular family for all* $\ell \in \mathbb{N} \cup \{0\}$*.* △

In addition to being ℓ-independent, the condition (4.20) is more natural and is simpler to implement in a discretization scheme, in the sense that it will lead to a Dirichlet-type boundary condition as shown below.

4.1.2 Outgoing boundary condition

For the numerical discretization on finite domain, we need to replace the outgoing condition (4.14) by one on an artificial boundary. The condition (4.14) is replaced exactly by the exterior Dirichlet-to-Neumann operator, see discussion in [5, Section 4.1]. In particular in the case of the solar atmosphere, if ρ and $\mathfrak{c}$ are extended according to the `Atmo` model on $(r_{\max}, \infty)$, then we have an explicit expression for the D-t-N coefficient (cf. [5]),

$$\mathbf{Z}^{\ell}_{\mathrm{DtN}}(r) \;:=\; -2\,\mathrm{i}\,\mathsf{k}\,\frac{\mathrm{W}'_{-\frac{\mathrm{i}\alpha}{2\mathsf{k}},\ell+1/2}(-2\mathrm{i}\mathsf{k}r)}{\mathrm{W}_{-\frac{\mathrm{i}\alpha}{2\mathsf{k}},\ell+\frac{1}{2}}(-2\mathrm{i}\mathsf{k}r)}\,, \tag{4.25}$$

where W is the Whittaker's special function, cf. [5, 4], and k is defined by (4.16). The outgoing condition (4.14) is then replaced by

$$\partial_n G_\ell \;=\; \mathbf{Z}^{\ell}_{\mathrm{DtN}}(r)\,G_\ell\,. \tag{4.26}$$

Under more general assumptions of extensions, one does not have explicit description of the D-t-N. However, if the extension still maintains the structure of V_{ω,γ_∞} as discussed in Assumptions 1 to 3, since we are working mode by mode, one can use the *nonlocal* radiation boundary condition, which is an approximate condition,

$$\mathbf{Z}^{\ell}_{\mathrm{nonlocal}}(r) \;=\; \mathrm{i}\left(\frac{\sigma^2(r)}{\mathfrak{c}^2(r)} \;-\; \mathsf{q}(r) \;-\; \frac{\ell(\ell+1)}{r^2}\right)^{1/2}\,. \tag{4.27}$$

We will also investigate the performance of other approximate radiation conditions listed in Section 5.

4.2 Numerical calculation of the Green function

With $r_{\max} > \mathsf{r}_a$, we consider the numerical calculation of the modal Green kernel (4.12),

$$\mathsf{L}_\ell\,G_\ell \;=\; \delta(r-s)\,; \tag{4.28a}$$

$$\lim_{r\to 0} r\left(\frac{G_\ell}{r}\right)' \;=\; 0\,; \tag{4.28b}$$

$$G'_\ell(r_{\max}) \;=\; \mathbf{Z}_\bullet(r_{\max})\,G_\ell(r_{\max})\,. \tag{4.28c}$$

We recall the notation in (4.9) and (4.10),

$$\mathsf{L}_\ell \;=\; -\frac{d^2}{dr^2} \;+\; \frac{Q_\ell}{r^2} \quad \text{with} \quad \frac{Q_\ell(r)}{r^2} \;=\; -\frac{\sigma^2(r)}{\mathfrak{c}^2(r)} \;+\; \mathsf{q}(r) \;+\; \frac{\ell(\ell+1)}{r^2}\,. \tag{4.29}$$

4.2.1 Approach 1

We rewrite the working ODE (4.28) in first-order formulation in order to apply the Hybridizable Discontinuous Galerkin (HDG) discretization method discussed in Section 6. Denote by $\tilde{G}_\ell = G_\ell / r$ then $\tilde{G}$ solves[4]

$$\begin{aligned} -\frac{d}{dr}\left(r^2\,\frac{d}{dr}\,\tilde{G}\right) \,+\, Q_\ell\,\tilde{G}_\ell \,&=\, r\,\delta(r-s)\,; \\ \lim_{r\to 0} r\,\tilde{G}' \,=\, 0 \quad , \quad \tilde{G}'(r) \,&=\, \left(-\tfrac{1}{r} \,+\, \mathbf{Z}_\bullet\right)\tilde{G} \quad \text{at } r = r_{\max}\,, \end{aligned} \tag{4.30}$$

In using the first-order formulation, cf. Subsection 6.1, problem (4.30) is written as,

$$\begin{cases} -r\,(r\,v)' \,+\, Q(r)\,w \,=\, r^2\,\delta(r-s) \quad \text{on }]0, r_{\max}[\;; & (4.31\text{a}) \\ r\,w' \,-\, w \,=\, r\,v \quad \text{on }]0, r_{\max}[\;; & (4.31\text{b}) \\ \lim_{r\to 0} v \,=\, 0\,; & (4.31\text{c}) \\ v \,=\, \left(-\tfrac{1}{r} \,+\, \mathbf{Z}_\bullet\right) w \quad \text{at } r = r_{\max}\,. & (4.31\text{d}) \end{cases}$$

In our applications, we also use the generic right-hand side $g = r\delta(r-s)$, cf. (4.30), and $u = \tilde{G}_\ell = G_\ell/r$. The numerical value of G_ℓ is obtained from the second component of (v, w) which solves (4.31), on $[0, r_{\max}]$, i.e., $G_\ell \,=\, w$.

Remark 3. *With each implementation, i.e. with a fixed value of* $s \in (0, r_{\max})$*, one obtains the value of the Green kernel* $G_\ell(r, s)$ *on the vertical segment* $[0, r_{\max}] \times s_0$*, and its symmetric reflection across the diagonal* $r = s$*. In short, we obtain for each computation with a fixed source* s*, the value of* G_ℓ *on*

$$[0\,,\, r_{\max}]_r \,\times\, \{s_0\} \qquad \bigcup \qquad \{s_0\}_r \,\times\, [0\,,\, r_{\max}]_s\,. \tag{4.32}$$

One can take advantage of the multiple right-hand sides features of direct solver such as `MUMPS` *to calculate at the same time and obtain the value of* G_ℓ *on several vertical line segments (and hence their symmetric reflexion). This however requires the use of the same domain discretization for all of the right-hand sides.*

△

4.2.2 Approach 2

We make use of the formula (4.17). Consider $0 < a < b < r_{\max}$, and $\mathsf{r}_a < r_{\max}$. We construct the regular homogeneous solution ψ on $[0, b]$ and the Green function G_ℓ is then obtained on domain defined (4.17) (see also Figure 1).

Step 1a Compute $\psi(t)$ on $[0, b]$. The numerical value of ψ and ψ' are obtained from (v, w) which

---

[4] This can be seen as follows.

$$-d_r^2\,(\tilde{G}_\ell r) \,+\, \frac{Q_\ell}{r^2}\,\tilde{G}_\ell\,r \,=\, \delta(r-s) \qquad \Rightarrow \qquad -r\tilde{G}_\ell'' \,-2\tilde{G}' \,+\, \frac{Q_\ell}{r^2}\,r\,\tilde{G}_\ell \,=\, \delta(r-s)$$

$$\Rightarrow \quad -\tilde{G}_\ell'' \,-\, 2\frac{\tilde{G}'}{r} \,+\, \frac{Q_\ell}{r^2}\,\tilde{G}_\ell \,=\, r^{-1}\,\delta(r-s) \qquad \Rightarrow \qquad -r^2\tilde{G}'' \,-\, 2r\tilde{G}' \,+\, Q_\ell\,\tilde{G}_\ell \,=\, r\,\delta(r-s)$$

In using that $(r^2\tilde{G}')' = r^2\tilde{G}'' + 2r\tilde{G}'$, we obtain $-(r^2\,\tilde{G}')' \,+\, Q_\ell \,=\, r\,\delta(r-s)$. We carry out the same calculation to obtain the RBC for $\tilde{G}$. Since $G_\ell' \,=\, \left(r\,\tilde{G}_\ell\right)' \,=\, r\,\tilde{G}_\ell' \,+\, \tilde{G}_\ell$. At $r = r_{\max}$, we replace G_ℓ' in using this identity to obtain,

$$r_{\max}\,\tilde{G}_\ell'(r_{\max}) \,+\, \tilde{G}_\ell(r_{\max}) \,=\, \mathbf{Z}_\bullet(r_{\max})\,r_{\max}\,\tilde{G}_\ell(r_{\max}) \quad \Rightarrow \quad \tilde{G}_\ell'(r_{\max}) \,=\, \left(-\tfrac{1}{r_{\max}} \,+\, \mathbf{Z}_\bullet(r_{\max})\right)\tilde{G}_\ell(r_{\max})\,.$$

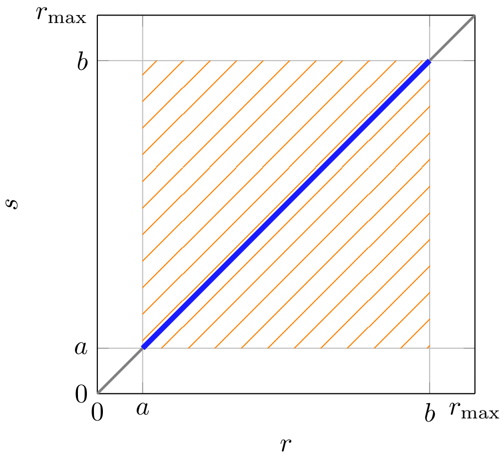

Figure 1: Domain of definition (shaded region) of modal Green kernel $G_\ell(r,s)$ obtained via Approach 2 by gluing together two homogeneous solution ψ to (4.33) on $[0,b]$ and $\tilde{\psi}$ to (4.35) on $[a,r_{\max}]$ by formula (4.17). In contrast, in Approach 1, with each resolution of (4.31) for a fixed source s_0, one obtains the value of the G_ℓ only on the horizontal segment $[0,r_{\max}]\times s_0$ and its reflection across the diagonal $\{r=s\}$.

solves

$$\begin{cases} -r\,(r\,v)' \;+\; Q(r)\,w \;=\; 0 \quad \text{on }]0,b[\;; & (4.33a)\\ r\,w' \;-\; w \;=\; r\,v \quad \text{on }]0,b[\;; & (4.33b)\\ v\,(r=0) \;=\; 0\;; & (4.33c)\\ w \;=1 \quad \text{at } r=b\;, & (4.33d) \end{cases}$$

by letting

$$\psi(t) \;=\; w(t) \quad , \quad \psi'(t) \;=\; v \;+\; \frac{w}{r}\,. \tag{4.34}$$

The second identity comes from the definition of v and w in (6.2), $u=\dfrac{w}{r}$ and $v=ru'$ thus $v=r\left(\dfrac{w}{r}\right)'=w'-\dfrac{w}{r}$.

Step 1b Compute $\tilde{\psi}(t)$ on $[a,r_{\max}]$ in a similar way. In particular, the numerical values of $\tilde{\psi}$ and $\tilde{\psi}'$ are obtained from (v,w) which solves

$$\begin{cases} -r\,(r\,v)' \;+\; Q(r)\,w \;=\; 0 \quad \text{on }]a,r_{\max}[\;; & (4.35a)\\ r\,w' \;-\; w \;=\; r\,v \quad \text{on }]a,r_{\max}[\;; & (4.35b)\\ w \;=1 \quad \text{at } r=a\;; & (4.35c)\\ v \;=\; \left(-\tfrac{1}{r} \;+\; \mathbf{Z}_{\bullet}\right) w \quad \text{at } r=r_{\max}\;, & (4.35d) \end{cases}$$

by letting

$$\tilde{\psi}(t) \;=\; w(t) \quad , \quad \tilde{\psi}'(t) \;=\; v \;+\; \frac{w}{r}\,. \tag{4.36}$$

Step 2 We put together the value of ψ on $[0,b]$ and $\tilde{\psi}$ on $[a,r_{\max}]$ to obtain

$$G_\ell(r,s) \;=\; \frac{-\mathrm{H}(s-r)\,\psi(r)\,\tilde{\psi}(s) \;-\; \mathrm{H}(r-s)\,\tilde{\psi}(r)\,\psi(s)}{\mathcal{W}\{\psi(s)\,,\,\tilde{\psi}(s)\}}\,. \tag{4.37}$$

on

$$\Omega \;:=\; \big([a\,,\,r_{\max}]_r \;\times\; [0,b]_s\big) \;\bigcup\; \big([0\,,\,b]_r \;\times\; [a\,,\,r_{\max}]_s\big)\,. \tag{4.38}$$

Remark 4. *This approach offers the following advantages.*

- *The functions ψ and $\tilde{\psi}$ are regular on their corresponding domain of computation, and there are no singular sources. Because of the second reason, one does not need to refine the mesh around the singularities of the source.*
- *One can take advantage of the feature of the HDG method which gives readily the derivative of the solution.* △

5 Radiation boundary conditions

In this section, we recall the different radiation coefficient $\mathbf{Z}_\bullet$ derived in the literature. They comprise of new coefficients derived in [4] and [5], and old ones in [3]. A preliminary comparison of their efficiency was given in [4, 5], using the exterior Dirichlet problem under `Pure Atmo` assumptions (listed in (5.8)) and high-order finite difference. Since the corresponding solution for each $\mathbf{Z}_\bullet$ can be described explicitly in terms of Whittaker functions, we revisit this problem and present a comparison based on analytical errors.

5.1 Radiation boundary conditions

The choice of radiation boundary conditions $\mathbf{Z}_\bullet$ is investigated in [5, 3, 4] where several possibilities are given to compromise between complexity and accuracy. Let us first review those different conditions, where the exponent ℓ indicates that the condition depends on the mode, which means its implementation in dimension higher than one is difficult. Overall, eleven conditions have been derived. We recall k is defined in (4.16),

$$\mathsf{k} \,=\, \sqrt{\frac{\sigma^2}{\mathfrak{c}_\infty^2} - \frac{\alpha_\infty^2}{4}}\,. \tag{5.1}$$

1. The reference coefficient $\mathbf{Z}^\ell_{\text{DtN}}$ corresponds with the exact Dirichlet-to-Neumann condition, with

$$\mathbf{Z}^\ell_{\text{DtN}} \,:=\, -2\,\mathrm{i}\,\mathsf{k}\,\frac{\mathrm{W}'_{-\chi,\ell+\frac{1}{2}}(-2\,\mathrm{i}\,\mathsf{k}\,r_{\max})}{\mathrm{W}_{-\chi,\ell+\frac{1}{2}}(-2\,\mathrm{i}\,\mathsf{k}\,r_{\max})}\,. \tag{5.2}$$

   It makes use of the Whittaker's function W, and of

$$\chi \,=\, \frac{\mathrm{i}\alpha}{2\mathsf{k}} \,=\, \frac{\mathrm{i}\,\alpha\,\mathfrak{c}^2}{2\,\sigma^2}\,, \qquad \text{where } \alpha \,=\, \alpha_\infty \,=\, \alpha(r_{\max})\,. \tag{5.3}$$

2. The nonlocal modal radiation coefficient $\mathbf{Z}^\ell_{\text{nonlocal}}$ is given by

$$\begin{aligned}\mathbf{Z}^\ell_{\text{nonlocal}} \,&=\, \mathrm{i}\,\frac{\sigma}{\mathrm{c}_\infty}\left(1 - \frac{\mathrm{c}_\infty^2}{\sigma^2}\left(\frac{\alpha_\infty^2}{4} + \frac{\alpha_\infty}{r_{\max}} + \frac{\ell(\ell+1)}{r_{\max}^2}\right)\right)^{1/2}\\ &=\, \mathrm{i}\,\mathsf{k}\left(1 \,-\, \frac{\alpha_\infty}{r}\,\frac{1}{\mathsf{k}^2} \,-\, \frac{\ell(\ell+1)}{(r_{\max}\,\mathsf{k})^2}\right)^{1/2}\,.\end{aligned}$$

3. The `HF`-family gives rise to five conditions, such that

$$\begin{aligned}\mathbf{Z}_{\texttt{S-HF-0}} \,&=\, \mathrm{i}\,\mathsf{k}\,,\\ \mathbf{Z}_{\texttt{S-HF-1a}} \,&=\, \mathrm{i}\,\mathsf{k} \,-\, \frac{\mathrm{i}}{2\,\mathsf{k}}\,\frac{1}{r_{\max}}\alpha_\infty\,,\\ \mathbf{Z}^\ell_{\texttt{S-HF-1b}} \,&=\, \mathrm{i}\,\mathsf{k} \,-\, \frac{\mathrm{i}}{2\,\mathsf{k}}\,\frac{1}{r_{\max}}\left(\alpha_\infty + \frac{\ell(\ell+1)}{r_{\max}}\right)\,,\\ \mathbf{Z}_{\texttt{A-HF-0}} \,&=\, \mathrm{i}\,\frac{\sigma}{\mathrm{c}_\infty}\,,\\ \mathbf{Z}^\ell_{\texttt{A-HF-1}} \,&=\, \mathrm{i}\,\frac{\sigma}{\mathrm{c}_\infty} \,+\, \frac{\mathrm{c}_\infty}{2\,\mathrm{i}\,\sigma}\left(\frac{\ell(\ell+1)}{r_{\max}^2} + \frac{\alpha_\infty}{r_{\max}} + \frac{\alpha_\infty^2}{4}\right)\,.\end{aligned} \tag{5.4}$$

4. The `SAI`-family adds two conditions:

$$\begin{aligned}\mathbf{Z}_{\texttt{SAI-0}} &= \mathrm{i}\,\mathsf{k}\left(1 - \frac{\alpha_\infty}{r_{\max}}\frac{1}{\mathsf{k}^2}\right)^{1/2};\\ \mathbf{Z}^{\ell}_{\texttt{SAI-1}} &= \mathrm{i}\mathsf{k}\left(1 - \frac{\alpha_\infty}{r_{\max}}\frac{1}{\mathsf{k}^2}\right)^{1/2} - \frac{\mathrm{i}}{2}\frac{\frac{\ell(\ell+1)}{r_{\max}^2\,\mathsf{k}}}{\left(1 - \frac{\alpha_\infty}{r_{\max}}\frac{1}{\mathsf{k}^2}\right)^{1/2}}\,.\end{aligned} \tag{5.5}$$

5. The RBC condition is

$$\mathbf{Z}_{\texttt{A-RBC-1}} := \frac{1}{r_{\max}} + \mathbf{Z}_{\texttt{S-HF-0}}\,. \tag{5.6}$$

6. We finally include a “naive” condition analogous in the spirit of Sommerfeld condition:

$$\mathbf{Z}_{\texttt{Naive}} := \frac{1}{r_{\max}} + \frac{\alpha_\infty}{2} + \mathrm{i}\frac{\sigma}{\mathrm{c}_\infty}\,. \tag{5.7}$$

5.2 Analytic solutions depending on the radiation condition

To investigate the efficiency of the radiation boundary conditions introduced above in approximating the outgoing solution, we compare with respect to the exact one given using $\mathbf{Z}^{\ell}_{\mathrm{DtN}}$. To extract the analytic solution, we consider the problem where the condition at the origin is replaced by a unitary Dirichlet one in $r_{\min} \neq 0$, and we use a homogeneous medium parameter, such that, in particular, $\alpha(r) = \alpha_\infty$ and $\alpha' = 0$. Therefore, we consider the problem

$$\begin{cases}\left(-\dfrac{d^2}{dr^2} - \mathsf{k}^2 + \dfrac{\alpha_\infty}{r} + \dfrac{\ell(\ell+1)}{r^2}\right)w = 0\,, & \text{in }]r_{\min}, r_{\max}[\,,\\ w(r_{\min}) = 1\,, & \\ \dfrac{dw}{dr}(r_{\max}) = \mathbf{Z}_\bullet\, w(r_{\max})\,. &\end{cases} \tag{5.8}$$

This problem is obtained from (4.28a) and (4.29) using the potential

$$\frac{Q^{\mathrm{Atmo}}_{\ell}}{r^2} = -\mathsf{k}^2 + \frac{\alpha_\infty}{r} + \frac{\ell(\ell+1)}{r^2}\,. \tag{5.9}$$

This is recalled in Subsection 7.1.

We denote the corresponding solution to (5.8) by $w_{\mathbf{Z}_\bullet,\ell,\omega} = w_{\mathbf{Z}_\bullet}$, where the *reference* solution is given by $\mathbf{Z}^{\ell}_{\mathrm{DtN}}$. As already mentioned, in [5, 4], we have carried out a preliminary study of this problem, using finite difference discretization schemes and comparing the solutions $w_{\mathbf{Z}_\bullet,\ell,\omega}$. In the following, we provide an *analytical* evaluation of the efficiency of the radiation boundary conditions.

Let us first give the analytical form of $w_{\mathbf{Z}_\bullet}$. On $[1,\infty)$, a basis of linearly independent solutions is

$$\mathrm{W}_{-\chi\,,\,\ell+1/2}(-2\mathrm{i}\mathsf{k}r)\,, \qquad \mathrm{W}_{\chi\,,\,\ell+1/2}(2\mathrm{i}\mathsf{k}r)\,, \tag{5.10}$$

with χ given in (5.3). Thus, we have

$$w_{\mathbf{Z}_\bullet} = a_{\mathbf{Z}_\bullet,\ell}\,\mathrm{W}_{-\chi,\ell+1/2}(-2\,\mathrm{i}\,\mathsf{k}\,r) + b_{\mathbf{Z}_\bullet,\ell}\,\mathrm{W}_{\chi,\ell+1/2}(2\,\mathrm{i}\,\mathsf{k}\,r)\,, \tag{5.11}$$

and

$$w'_{\mathbf{Z}_\bullet} = -2\,\mathrm{i}\,\mathsf{k}a_{\mathbf{Z}_\bullet,\ell}\,\mathrm{W}'_{-\chi,\ell+1/2}(2\mathrm{i}\mathsf{k}\,r) + 2\,\mathrm{i}\,\mathsf{k}\,b_{\mathbf{Z}_\bullet,\ell}\,\mathrm{W}'_{\chi,\ell+1/2}(2\mathrm{i}\mathsf{k}r)\,.$$

The coefficients $a_{\mathbf{Z}_\bullet,\ell} = a_{\mathbf{Z}_\bullet}$ and $b_{\mathbf{Z}_\bullet,\ell} = b_{\mathbf{Z}_\bullet}$ are determined by the boundary conditions such that, for (5.8),

$$\mathsf{A}_{\mathbf{Z}_\bullet,\ell}\begin{pmatrix}a_\ell\\ b_\ell\end{pmatrix} = \begin{pmatrix}1\\0\end{pmatrix}, \tag{5.12}$$

with matrix

$$\begin{aligned}\mathsf{A}_{\mathbf{Z}_\bullet,\ell} \;:=\;& \begin{pmatrix} \mathrm{W}_{-\chi,\ell+1/2}(-2\,\mathrm{i}\,\mathrm{k}\,r_{\min}) & \mathrm{W}_{\chi,\ell+1/2}(2\,\mathrm{i}\,\mathrm{k}\,r_{\min}) \\ -2\mathrm{k}\mathrm{i}\mathrm{W}'_{-\chi,\ell+1/2}(-2\,\mathrm{i}\,\mathrm{k}\,r_{\max}) & 2\mathrm{k}\mathrm{i}\mathrm{W}'_{\chi,\ell+1/2}(2\,\mathrm{i}\,\mathrm{k}\,r_{\max}) \end{pmatrix} \\ &-\;\mathbf{Z}_\bullet \begin{pmatrix} 0 & 0 \\ \mathrm{W}_{-\chi,\ell+1/2}(2\,\mathrm{i}\,\mathrm{k}\,r_{\max}) & \mathrm{W}_{\chi,\ell+1/2}(2\,\mathrm{i}\,\mathrm{k}\,r_{\max}) \end{pmatrix}.\end{aligned} \tag{5.13}$$

The reference solution is given by the unique solution to (5.8) with $\mathbf{Z}^{\ell}_{\mathrm{DtN}}$, and is given by

$$w_{\mathrm{ref}}(r) \;=\; w_{\mathbf{Z}^{\ell}_{\mathrm{DtN}}}(r) \;=\; \frac{\mathrm{W}_{-\chi,\ell+1/2}(-2\,\mathrm{i}\,\mathrm{k}\,r)}{\mathrm{W}_{-\chi,\ell+1/2}(-2\,\mathrm{i}\,\mathrm{k}\,\mathrm{r}_{\min})}\,, \tag{5.14}$$

which verification is given in the following proposition.

Proposition 1. *The exact solution to* (5.8) *with* $\mathbf{Z}^{\ell}_{DtN}$ *is given by* (5.14)*.*

Proof. We first rewrite the second row of $\mathsf{A}_{\mathtt{DtN}}$, by substituting $\mathbf{Z}^{\ell}_{\mathrm{DtN}}$ in (5.13) by its explicit expression of (5.2). We have

$$[\mathsf{A}_{\mathtt{DtN}}]_{21} \;=\; -2\mathrm{k}\mathrm{i}\mathrm{W}'_{-\chi,\ell+1/2}(-2\,\mathrm{i}\,\mathrm{k}\,r_{\max}) \;-\; \left(-2\,\mathrm{i}\,\mathrm{k}\,\frac{\mathrm{W}'_{-\chi,\ell+\frac{1}{2}}(-2\,\mathrm{i}\,\mathrm{k}\,r_{\max})}{\mathrm{W}_{-\chi,\ell+\frac{1}{2}}(-2\,\mathrm{i}\,\mathrm{k}\,r_{\max})}\right)\mathrm{W}_{-\chi,\ell+1/2}(2\,\mathrm{i}\,\mathrm{k}\,r_{\max})\,. \tag{5.15}$$

We obtain readily that $[\mathsf{A}_{\mathtt{DtN}}]_{21} \;=\; 0$.

We next consider the $(2,2)$ component. We have

$$\begin{aligned}[\mathsf{A}_{\mathtt{DtN}}]_{22} \;&=\; 2\mathrm{k}\mathrm{i}\mathrm{W}'_{\chi,\ell+1/2}(2\,\mathrm{i}\,\mathrm{k}\,r_{\max}) \;-\; \left(-2\,\mathrm{i}\,\mathrm{k}\,\frac{\mathrm{W}'_{-\chi,\ell+\frac{1}{2}}(-2\,\mathrm{i}\,\mathrm{k}\,r_{\max})}{\mathrm{W}_{-\chi,\ell+\frac{1}{2}}(-2\,\mathrm{i}\,\mathrm{k}\,r_{\max})}\right)\mathrm{W}_{\chi,\ell+1/2}(2\,\mathrm{i}\,\mathrm{k}\,r_{\max}); \\ &=\; 2\mathrm{k}\mathrm{i}\frac{\mathrm{W}'_{\chi,\ell+1/2}(2\,\mathrm{i}\,\mathrm{k}\,r_{\max})\,\mathrm{W}_{-\chi,\ell+1/2}(-2\,\mathrm{i}\,\mathrm{k}\,r_{\max}) \;+\; \mathrm{W}_{-\chi,\ell+1/2}(-2\,\mathrm{i}\,\mathrm{k}\,r_{\max})\mathrm{W}_{\chi,\ell+1/2}(2\,\mathrm{i}\,\mathrm{k}\,r_{\max})}{\mathrm{W}_{-\chi,\ell+1/2}(-2\,\mathrm{i}\,\mathrm{k}\,r_{\max})}\,.\end{aligned} \tag{5.16}$$

We next observe that the denominator of the right-hand side is given by the Wronskian,

$$\begin{aligned}&\mathcal{W}\{\,\mathrm{W}_{\chi,\ell+1/2}(2\,\mathrm{i}\,\mathrm{k}\,r)\;,\;\mathrm{W}_{-\chi,\ell+1/2}(-2\,\mathrm{i}\,\mathrm{k}\,r)\,\} \\ &\quad=\; \det\begin{pmatrix} \mathrm{W}_{\chi,\ell+1/2}(2\,\mathrm{i}\,\mathrm{k}\,r) & \mathrm{W}_{-\chi,\ell+1/2}(-2\,\mathrm{i}\,\mathrm{k}\,r) \\ 2\mathrm{i}\mathrm{k}\mathrm{W}'_{\chi,\ell+1/2}(2\,\mathrm{i}\,\mathrm{k}\,r) & -2\mathrm{k}\mathrm{i}\mathrm{W}'_{-\chi,\ell+1/2}(-2\,\mathrm{i}\,\mathrm{k}\,r)\end{pmatrix} \\ &\quad=\; -2\,\mathrm{k}\,\mathrm{i}\,\mathrm{W}_{\chi,\ell+1/2}(2\,\mathrm{i}\,\mathrm{k}\,r)\,\mathrm{W}'_{-\chi,\ell+1/2}(-2\,\mathrm{i}\,\mathrm{k}\,r) \;-\; \mathrm{W}_{-\chi,\ell+1/2}(-2\,\mathrm{i}\,\mathrm{k}\,r)\,2\,\mathrm{i}\,\mathrm{k}\,\mathrm{W}'_{\chi,\ell+1/2}(2\,\mathrm{i}\,\mathrm{k}\,r)\,.\end{aligned}$$

On the other hand, by [28, 13.14.30], the Wronskian has value

$$\mathcal{W}\{\,\mathrm{W}_{\chi,\ell+1/2}(2\,\mathrm{i}\,\mathrm{k}\,r)\,,\,\mathrm{W}_{-\chi,\ell+1/2}(e^{-\pi\mathrm{i}}\,2\,\mathrm{i}\,\mathrm{k}\,r)\,\} \;=\; e^{\mathrm{i}\pi\chi}\,. \tag{5.17}$$

We thus obtain

$$[\mathsf{A}_{\mathtt{DtN}}]_{22} \;=\; \frac{-e^{\chi\pi\mathrm{i}}}{\mathrm{W}_{\chi,\ell+1/2}(2\,\mathrm{i}\,\mathrm{k}\,r_{\max})}\,. \tag{5.18}$$

Putting together the above computations, we obtain the simplified form of $\mathsf{A}_{\mathbf{Z}^{\ell}_{\mathrm{DtN}}}$,

$$\mathsf{A}_{\mathbf{Z}^{\ell}_{\mathrm{DtN}}} \;:=\; \begin{pmatrix} \mathrm{W}_{-\chi,\ell+1/2}(-2\,\mathrm{i}\,\mathrm{k}\,r_{\min}) & \mathrm{W}_{\chi,\ell+1/2}(2\,\mathrm{i}\,\mathrm{k}\,r_{\min}) \\ 0 & \dfrac{-e^{\chi\pi\mathrm{i}}}{\mathrm{W}_{\chi,\ell+1/2}(2\,\mathrm{i}\,\mathrm{k}\,r_{\max})}\,. \end{pmatrix} \tag{5.19}$$

As a result of which, we have

$$\begin{pmatrix} a_{\mathbf{Z}^{\ell}_{\mathrm{DtN}}} \\ b_{\mathbf{Z}^{\ell}_{\mathrm{DtN}}} \end{pmatrix} \;=\; \mathsf{A}^{-1}_{\mathbf{Z}^{\ell}_{\mathrm{DtN}}}\begin{pmatrix}1\\0\end{pmatrix} \;=\; \begin{pmatrix} \frac{1}{\mathrm{W}_{-\chi,\ell+1/2}(-2\,\mathrm{i}\,\mathrm{k}\,\mathrm{r}_{\min})} \\ 0 \end{pmatrix} \tag{5.20}$$

which leads to the form of solution in (5.14).

□

5.3 Analytic evaluation of the boundary condition efficiency

The efficiency of the choice of $\mathbf{Z}_\bullet$ is assessed by comparing the coefficients $a_{\mathbf{Z}_\bullet,\ell}$ and $b_{\mathbf{Z}_\bullet,\ell}$ which define the analytic solution from (5.11). They are compared with the reference ones given by (5.20). We introduce the following norms to evaluate the difference,

$$\begin{aligned}\check{\mathfrak{e}}_{\mathbf{Z}_\bullet,\ell} &= \frac{|a_{\mathbf{Z}_\bullet,\ell} - a_{\mathbf{Z}^\ell_{\mathrm{DtN}},\ell}|^2 \,+\, |b_{\mathbf{Z}_\bullet,\ell}|^2}{|a_{\mathbf{Z}^\ell_{\mathrm{DtN}},\ell}|^2}\,,\\ \mathfrak{e}_{\mathbf{Z}_\bullet,\ell} &= \frac{\|u_{\mathbf{Z}^\ell_{\mathrm{DtN}},\ell} \,-\, u_{\mathbf{Z}_\bullet,\ell}\|_{L^2(r_{\min},r_{\max})}}{\|u_{\mathbf{Z}^\ell_{\mathrm{DtN}},\ell}\|_{L^2(r_{\min},r_{\max})}}\,.\end{aligned} \tag{5.21}$$

In Figures 2 and 3, we picture the error norm $\check{\mathfrak{e}}_{\mathbf{Z}_\bullet}$ respectively without ($\gamma = 0$) and with ($\gamma = 10^{-4}$) attenuation, where the coefficients a_ℓ and b_ℓ are computed for all choices of impedance conditions using (5.12) and (5.13). The computations use an interval between $r_{\min} = 0.95$ and $r_{\max} = 1.05$, with the values of the parameters extracted from the Atmo model, for the scaled radius:

$$\text{the (scaled) velocity is} \qquad \mathfrak{c} = c/R_\odot = 9.87 \times 10^{-6}\,\mathrm{s}^{-1} \qquad \text{and} \quad \alpha_\infty = 6663.62. \tag{5.22}$$

In the figures, we investigate for the modes ℓ between 0 and 1000 and frequency $\omega/(2\pi)$ between 5.5 and 12 mHz.

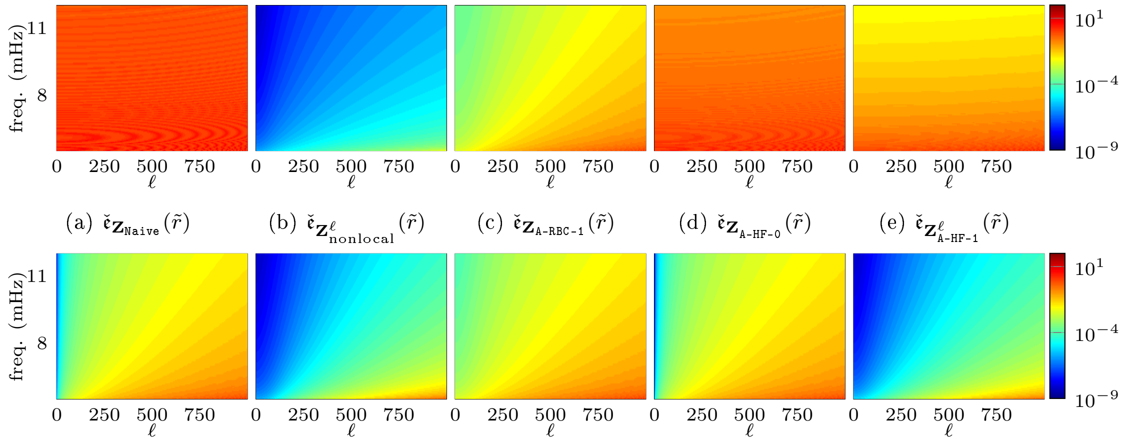

(a) $\check{\mathfrak{e}}_{\mathbf{Z}_{\texttt{Naive}}}(\tilde{r})$ (b) $\check{\mathfrak{e}}_{\mathbf{Z}^\ell_{\mathrm{nonlocal}}}(\tilde{r})$ (c) $\check{\mathfrak{e}}_{\mathbf{Z}_{\texttt{A-RBC-1}}}(\tilde{r})$ (d) $\check{\mathfrak{e}}_{\mathbf{Z}_{\texttt{A-HF-0}}}(\tilde{r})$ (e) $\check{\mathfrak{e}}_{\mathbf{Z}^\ell_{\texttt{A-HF-1}}}(\tilde{r})$

(g) $\check{\mathfrak{e}}_{\mathbf{Z}_{\texttt{SAI-0}}}(\tilde{r})$ (h) $\check{\mathfrak{e}}_{\mathbf{Z}^\ell_{\texttt{SAI-1}}}(\tilde{r})$ (i) $\check{\mathfrak{e}}_{\mathbf{Z}_{\texttt{S-HF-0}}}(\tilde{r})$ (j) $\check{\mathfrak{e}}_{\mathbf{Z}_{\texttt{S-HF-1a}}}(\tilde{r})$ (k) $\check{\mathfrak{e}}_{\mathbf{Z}^\ell_{\texttt{S-HF-1b}}}(\tilde{r})$

Figure 2: Comparison of the error norm $\check{\mathfrak{e}}_{\mathbf{Z}_\bullet}$ (5.21) for the different choices of boundary conditions, using constant `Atmo` parameters (5.22) without attenuation ($\gamma = 0$).

The error in the coefficients $a_{\mathbf{Z}_\bullet,\ell}$ and $b_{\mathbf{Z}_\bullet,\ell}$ (Figures 2 and 3) represents well the error for the global solution u (Figure 4). We observe the robustness of the different choices of impedance conditions: $\mathbf{Z}^\ell_{\mathrm{nonlocal}}$ gives the smaller error while $\mathbf{Z}^\ell_{\texttt{SAI-1}}$ and $\mathbf{Z}^\ell_{\texttt{S-HF-1b}}$ also behave well. In the family of conditions that do not depend on ℓ, $\mathbf{Z}_{\texttt{SAI-0}}$ and $\mathbf{Z}_{\texttt{S-HF-1a}}$ appears the most effective. We note that all conditions have difficulties for high ℓ at low frequencies, and that $\mathbf{Z}_{\texttt{Naive}}$ and $\mathbf{Z}_{\texttt{A-HF-0}}$ perform poorly for any combination of ω and ℓ. This analytical evaluation of the efficiency confirms perfectly the numerical evaluation we provided in [5].

6 Numerical implementation using HDG

For the discretization of the problem using inhomogeneous parameters, we use the Hybridizable Discontinuous Galerkin (HDG) method, which works with first-order problems. Namely, the HDG method gives access to the solution and its derivative with the same accuracy, such that we are able to readily compute

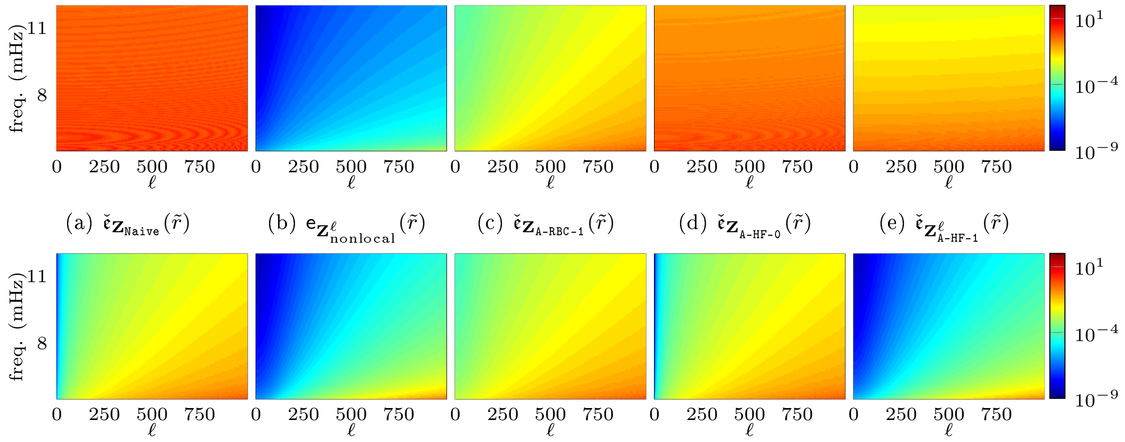

(a) $\check{\mathfrak{e}}_{\mathbf{Z}_{\texttt{Naive}}}(\tilde r)$ (b) $\mathfrak{e}_{\mathbf{Z}^{\ell}_{\text{nonlocal}}}(\tilde r)$ (c) $\check{\mathfrak{e}}_{\mathbf{Z}_{\texttt{A-RBC-1}}}(\tilde r)$ (d) $\check{\mathfrak{e}}_{\mathbf{Z}_{\texttt{A-HF-0}}}(\tilde r)$ (e) $\check{\mathfrak{e}}_{\mathbf{Z}^{\ell}_{\texttt{A-HF-1}}}(\tilde r)$

(g) $\check{\mathfrak{e}}_{\mathbf{Z}_{\texttt{SAI-0}}}(\tilde r)$ (h) $\check{\mathfrak{e}}_{\mathbf{Z}^{\ell}_{\texttt{SAI-1}}}(\tilde r)$ (i) $\check{\mathfrak{e}}_{\mathbf{Z}_{\texttt{S-HF-0}}}(\tilde r)$ (j) $\check{\mathfrak{e}}_{\mathbf{Z}_{\texttt{S-HF-1a}}}(\tilde r)$ (k) $\check{\mathfrak{e}}_{\mathbf{Z}^{\ell}_{\texttt{S-HF-1b}}}(\tilde r)$

Figure 3: Comparison of the error norm $\check{\mathfrak{e}}_{\mathbf{Z}_\bullet}$ (5.21) for the different choices of boundary conditions, using constant `Atmo` parameters (5.22) with attenuation $\gamma = 10^{-4}$.

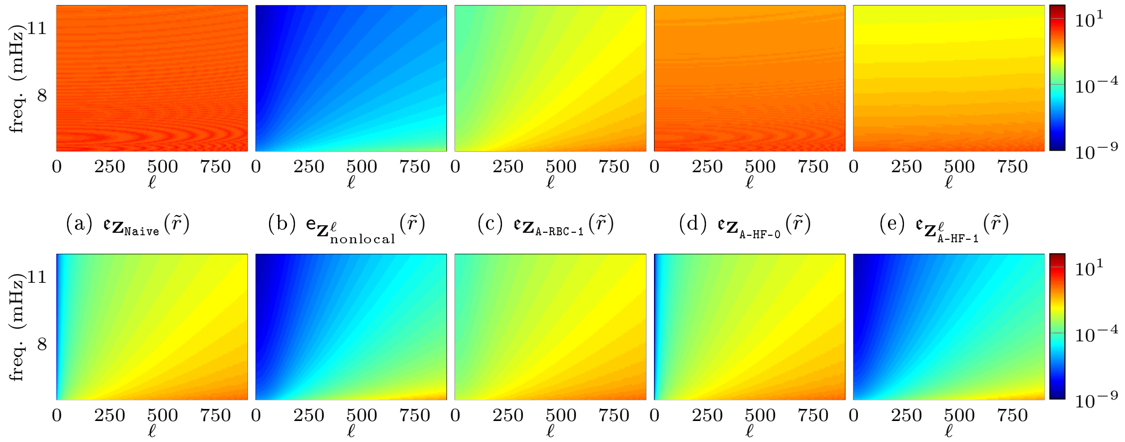

(a) $\mathfrak{e}_{\mathbf{Z}_{\texttt{Naive}}}(\tilde r)$ (b) $\mathfrak{e}_{\mathbf{Z}^{\ell}_{\text{nonlocal}}}(\tilde r)$ (c) $\mathfrak{e}_{\mathbf{Z}_{\texttt{A-RBC-1}}}(\tilde r)$ (d) $\mathfrak{e}_{\mathbf{Z}_{\texttt{A-HF-0}}}(\tilde r)$ (e) $\mathfrak{e}_{\mathbf{Z}^{\ell}_{\texttt{A-HF-1}}}(\tilde r)$

(g) $\mathfrak{e}_{\mathbf{Z}_{\texttt{SAI-0}}}(\tilde r)$ (h) $\mathfrak{e}_{\mathbf{Z}^{\ell}_{\texttt{SAI-1}}}(\tilde r)$ (i) $\mathfrak{e}_{\mathbf{Z}_{\texttt{S-HF-0}}}(\tilde r)$ (j) $\mathfrak{e}_{\mathbf{Z}_{\texttt{S-HF-1a}}}(\tilde r)$ (k) $\mathfrak{e}_{\mathbf{Z}^{\ell}_{\texttt{S-HF-1b}}}(\tilde r)$

Figure 4: Comparison of the error norm $\mathfrak{e}_{\mathbf{Z}_\bullet}$ (5.21) for the different choices of boundary conditions, using constant `Atmo` parameters (5.22) without attenuation ($\gamma = 0$).

the Wronskian in the Approach 2. In addition, the global system is built for the numerical trace, that is, it is only made of the degrees of freedom which are on the skeleton of the mesh (on the interfaces), hence reducing the size of the linear system compared to standard DG method. We detail below the numerical implementation.

6.1 First-order formulation

From (4.30), a prototype of the equations we have to solve is

$$-\left(r^2\,u'\right)' \,+\, Q_\ell\,u \,=\, g\,; \tag{6.1a}$$

$$\lim_{r\to 0} r\,u' \,=\, 0\,; \tag{6.1b}$$

$$u'(r) \,=\, \left(-\tfrac{1}{r} \,+\, \mathbf{Z}_\bullet\right) u \quad \text{at } r = r_{\max}\,. \tag{6.1c}$$

This is encountered in Approach 1, in which the generic right-hand side g, takes the form $r\delta(r-s)$. For Approach 2, $g=0$ and other types of boundary conditions are used, see Table 1.

We derive in details how (6.1) is written in first order formulation. The problems in Approach 2 are derived similarly with the only difference being the boundary conditions discussed in Table 1. We introduce the new variables w and v, where we omit the index ℓ for clarity:

$$\boxed{w \,:=\, r\,u \quad , \qquad v \,:=\, r\,u' \,, \qquad\qquad \text{first-order variables.}} \tag{6.2}$$

With this choice of variables, since

$$(r^2\,u')' \,=\, (r\,v)' \,, \tag{6.3}$$

equation (6.1a) is rewritten as

$$-\,(r\,v)' \,+\, \frac{Q_\ell}{r}\,w \,=\, g \quad \Rightarrow \quad -r\,(r\,v)' \,+\, Q_\ell\,w \,=\, r\,g\,. \tag{6.4}$$

The relation between w and v is given as,

$$rw' \,=\, ru \,+\, r^2u' \quad \Rightarrow \quad rw' \,=\, w + rv\,. \tag{6.5}$$

The radiation condition in terms of (w,v) is obtained by multiplying both sides of (6.1c) by $r_{\max}$, and by using the definition of w and v. In short, the first-order problem associated with (6.1) is given in terms of w and v by,

$$\boxed{\begin{cases} -\,r(r\,v)' \,+\, Q\,w \,=\, r\,g\,, \\ r\,w' \,-\, w \,=\, r\,v\,, \\ \lim\limits_{r\to 0}\, v \,=\, 0\,, \qquad\qquad v(r_{\max}) \,=\, \Big(-\dfrac{1}{r_{\max}} + \mathbf{Z}_\bullet\Big)\, w(r_{\max})\,. \end{cases}} \tag{6.6}$$

Here, the boundary conditions have been re-written accordingly, and we give in Table 1 the correspondence between the conditions given in terms of u and the ones in terms of $(w,\,v)$ in the first-order formulation.

Boundary conditions	Second-order for u	First-order for $(w,\,v)$, (6.6)
Dirichlet in r_0	$u(r_0) \,=\, \mathfrak{g}$	$w(r_0) = r_0\,\mathfrak{g}$
Limit at the origin	$\lim_{r\to 0}\, r\,u' \,=\, 0$	$\lim_{r\to 0}\, v \,=\, 0$
Radiation boundary condition in $r_1 \neq 0$	$u' \,=\, (-1/r + \mathbf{Z}_\bullet)u$	$v \,=\, (-1/r + \mathbf{Z}_\bullet)w$

Table 1: Correspondence between the boundary conditions in terms of u (second-order formulation) and in terms of $(w,\,v)$ (first-order formulation).

6.2 Domain partition and jump operator

We consider a non-overlapping partition of the one-dimensional domain $\Omega := [r_{\min},\, r_{\max}]$, in N elements K_e:

$$[r_{\min}\,,\, r_{\max}] \,=\, \bigcup_{e=1}^{N} K_e\,, \tag{6.7}$$

such that the discretized domain is composed of $N+1$ nodes $\{\mathsf{r}_i\}_{i=1}^{N+1}$. We denote by Σ the set of nodes, using Σ^B to denote the boundary nodes (that is, the two nodes that coincide with $r_{\min}$ and $r_{\max}$) and Σ^I for the interior ones, between two elements K_e:

$$\Sigma \,=\, \bigcup_{e=1}^{N} \partial K_e\,, \qquad \Sigma^B \,=\, \{r_{\min},\, r_{\max}\}\,, \qquad \Sigma^I = \Sigma \setminus \Sigma^B\,. \tag{6.8}$$

At a node (i.e., interface point) r shared by elements K^- and K^+, we define the jump, denoted by squared brackets, of a scalar function v by

$$\llbracket v \rrbracket|_{\mathsf{r}} := \big(\lim_{r \to \mathsf{r}^+} v\big)\, \nu_{\partial K^+}(\mathsf{r}) + \big(\lim_{r \to \mathsf{r}^-} v\big)\, \nu_{\partial K^+}(\mathsf{r})\,. \tag{6.9}$$

Here we denote by $\nu_{\partial K}$ the *outward* pointing normal vector of K defined along ∂_K. For an interval $K = [a, b]$ with $a < b$ then $\partial_K = \{a, b\}$ and our convention is $\nu_K(a) = -1$ and $\nu_K(b) = 1$.

At the boundary nodes of the domain, we use the same notation of the jump to refer to the trace on the boundary. In particular, for the left boundary point, we have

$$\llbracket v \rrbracket|_{\mathsf{r}_{\min}} := \big(\lim_{r \to \mathsf{r}_{\min}^+}\big)\, \nu_{\partial K}(\mathsf{r}_{\min}) = \lim_{r \to \mathsf{r}_{\min}^+} v(r)\,, \tag{6.10}$$

while for a right boundary point,

$$\llbracket v \rrbracket|_{\mathsf{r}_{\max}} := \big(\lim_{r \to \mathsf{r}_{\max}^-}\big)\, \nu_{\partial K}(\mathsf{r}_{\max}) = -\lim_{r \to \mathsf{r}_{\max}^-} v(r)\,. \tag{6.11}$$

6.3 Derivation of the HDG problem

In the HDG method, one considers the variational solution (w, v) of (6.6) on each interval K_e together with the selected boundary conditions at the end nodes (Σ^B) from Table 1. On the interior nodes (Σ^I) a *conservativity condition* is imposed:

$$\llbracket w \rrbracket\big|_{\Sigma^I} = 0\,, \qquad \llbracket v \rrbracket\big|_{\Sigma^I} = 0\,. \tag{6.12}$$

For the sake of clarity, we shall refer to a discretized element by K instead of K_e in the following.

6.3.1 Volume problem

Let us write the variational formulation for (6.6) on an interval K by integrating against a test function ϕ to obtain the *continuous local problem*:

$$\begin{cases} -\displaystyle\int_K (rv)'\, r\,\phi + \int_K Q\, w\, \phi = \int_K r\, g\, \phi\,, \\ \displaystyle\int_K r\, w'\phi - \int_K w\, \phi = \int_K r\, v\, \phi\,, \end{cases} \tag{6.13}$$

where we define

$$\frac{Q(r)}{r^2} = -\frac{\sigma^2}{\mathfrak{c}^2} + \frac{\alpha^2}{4} + \frac{\alpha'}{2} + \frac{\alpha}{r} + \frac{\ell(\ell+1)}{r^2}\,. \tag{6.14}$$

We carry out integration by parts to obtain

$$\begin{cases} \displaystyle\int_K r\, v\, (r\,\phi)' + \int_K Q\, w\, \phi - \sum_{\mathsf{r} \in \partial K} (r^2\,\phi)|_{\mathsf{r}}\, (v\, \nu_{\partial K})|_{\mathsf{r}} = \int_K r\, g\, \phi\,; \\ -\displaystyle\int_K w\, (r\,\phi)' - \int_K w\, \phi + \sum_{\mathsf{r} \in \partial K} (r\,\phi)|_{\mathsf{r}}\, (w\, \nu_{\partial K})|_{\mathsf{r}} = \int_K r\, v\, \phi\,. \end{cases} \tag{6.15}$$

We now define the approximation variables w_h and v_h respectively for $w|_{\overset{\circ}{K}}$ and $v|_{\overset{\circ}{K}}$. For the traces, $w|_{\partial K}$ and $v|_{\partial K}$ are respectively approximated by $\widehat{w}$ and $\widehat{v}$. The quantities $\widehat{w}$ and $\widehat{v}$ are further called the *numerical traces*. These numerical traces (at the nodes) are then expressed in terms of the auxiliary unknown λ and of the traces of w_h and v_h, and a penalization parameter τ^K,

$$\begin{aligned} \widehat{w\,\nu_{\partial K}} &= \lambda\, \nu_{\partial K} \quad , \quad r \in \partial K\,; \\ \widehat{v\,\nu_{\partial K}} &= v_h\, \nu_{\partial K} + \tau^K\, (w_h - \lambda)\, \nu_{\partial_K} \quad , \quad r \in \partial K\,. \end{aligned} \tag{6.16}$$

Here, λ, acts like a Lagrange multiplier and will play the role of the unknown in our global system.

By incorporating the approximation variables in (6.15), we have

$$\begin{cases} \displaystyle\int_K r\, v_h\, (r\,\phi)' \;+\; \int_K Q\, w_h\, \phi \;-\; \sum_{\mathsf{r}\in\partial K} (r^2\,\phi)|_{\mathsf{r}}\, \widehat{v\,\nu_{\partial K}}|_{\mathsf{r}} = \int_K r\, g\, \phi\,; \\ \displaystyle -\int_K w_h\, (r\,\phi)' \;-\; \int_K w_h\, \phi \;+\; \sum_{\mathsf{r}\in\partial K} (r\,\phi)|_{\mathsf{r}}\, \widehat{w\,\nu_{\partial K}}|_{\mathsf{r}} \;=\; \int_K r\, v\, \phi\,. \end{cases} \tag{6.17}$$

We further rewrite by using (6.16) to replace the numerical traces $\widehat{w}$ and $\widehat{v}$ such that

$$\begin{cases} \displaystyle\int_K r\, v_h\, (r\,\phi)' \;+\; \int_K Q\, w_h\, \phi \;-\; \sum_{\mathsf{r}\in\partial K} (r^2\;\phi)|_{\mathsf{r}} \Big(v_h\, \nu_{\partial K} \;+\; \tau^K\, (w_h \;-\; \lambda)\, \nu_{\partial_K} \Big)\Big|_{\mathsf{r}} \;=\; \int_K r\, g\, \phi\,; \\ \displaystyle -\int_K w_h\, (r\,\phi)' \;-\; \int_K w_h\, \phi \;+\; \sum_{\mathsf{r}\in\partial K} \big(r\,\phi\,\lambda\,\nu_{\partial K} \big)\Big|_{\mathsf{r}} \;=\; \int_K r\, v\, \phi\,. \end{cases} \tag{6.18}$$

We rewrite the first equation by carrying the (reverse) integration-by-parts to absorb the boundary term in v_h,

$$\begin{aligned} &\int_K r\, v_h\, (r\,\phi)' - \sum_{\mathsf{r}\in\partial K} (r^2\;\phi)|_{\mathsf{r}}\, \big(v_h\, \nu_{\partial K} \;+\; \tau^K\, (w_h \;-\; \lambda)\, \nu_{\partial_K}\big)|_{\mathsf{r}} \\ &\qquad = \; - \int_K (r\, v_h)'\, r\, \phi - \sum_{\mathsf{r}\in\partial K} (r^2\;\phi)|_{\mathsf{r}}\, \tau^K\, \big(w_h\, \nu_{\partial_K} \;-\; \lambda\, \nu_{\partial_K}\big)|_{\mathsf{r}}\,. \end{aligned} \tag{6.19}$$

The approximate local problem is given as

$$\begin{cases} \displaystyle -\int_K (r\, v_h)'\, r\, \phi \;+\; \int_K Q\, w_h\, \phi \;-\; \sum_{\mathsf{r}\in\partial K} (r^2\;\phi)|_{\mathsf{r}}\, \tau^K\, \big(w_h\, \nu_{\partial_K} \;-\; \lambda\, \nu_{\partial_K}\big)|_{\mathsf{r}} \;=\; \int_K r\, g\, \phi\,; & \text{(6.20a)} \\ \displaystyle -\int_K w_h\, (r\,\phi)' \;-\; \int_K w_h\, \phi \;+\; \sum_{\mathsf{r}\in\partial K} (r\,\phi\,\lambda\,\nu_{\partial K})|_{\mathsf{r}} \;=\; \int_K r\, v\, \phi\,. & \text{(6.20b)} \end{cases}$$

We see that the volume problem is local (independent) on each cell. We shall later sum over the cells to build the global linear system for λ.

6.3.2 Interface and boundary problems

The local interface and boundary problems are now derived from the conservativity equation (6.12)

$$[\![\widehat{v}]\!]|_{\mathsf{r}} \;=\; 0\,, \qquad \mathsf{r} \in \Sigma^I\,. \tag{6.21}$$

and the boundary conditions. We first rewrite these jumps more explicitly in terms of the numerical trace.

1. **Jump at an interior node**: Consider an interior point r shared by the element K^- on the left and K^+ on the right. Using (6.16), the jump is given as

$$[\![\,\widehat{v}\,]\!]\Big|_{\mathsf{r}} \;=\; \Big(v_h^{K^+} \;+\; \tau^{K^+}\, w_h^{K^+} \;-\tau^{K^+}\,\lambda \Big)\, \nu^{K^+}(\mathsf{r}) \;+\; \big(v_h^{K^-} \;+\tau^{K^-}\, w_h^{K^-} \;-\tau^{K^-}\,\lambda\big)\, \nu^{K^-}(\mathsf{r})\,, \tag{6.22}$$

   where we denote

$$\lim_{r\to\mathsf{r}^+} v_h = v_h^{K^+}\,, \qquad \lim_{r\to\mathsf{r}^+} w_h = w_h^{K^+}\,, \qquad \text{and} \qquad \nu_{\partial K^+} = \nu^{K^+}\,, \qquad \nu_{\partial K^-} = \nu^{K^-}\,. \tag{6.23}$$

2. **Jump condition at a boundary node**: For a boundary point r, the jump is given by

$$[\![\,\widehat{v}\,]\!]\Big|_{\mathsf{r}} := \Big(v_h^K \;+\; \tau^K\, w_h^K \;-\tau^K\,\lambda \Big)\, \nu^K(\mathsf{r})\,. \tag{6.24}$$

Then, one can replace with the boundary conditions listed in Table 1. For instance, the radiation boundary condition writes as

$$[\![\widehat{v}]\!]\big|_{\mathsf{r}_{N+1}} = \left(-\frac{1}{\mathsf{r}_{N+1}} + \mathbf{Z}_{\bullet}\right) \left(\widehat{w}\,\nu_{\partial\Omega}\right)\big|_{\mathsf{r}_{N+1}} \qquad \text{with} \quad \mathsf{r}_{N+1} = r_{\max}. \tag{6.25}$$

We are now ready to derive the local problems associated to the nodes. We distinguish between an interior element and a boundary one. It is convenient to refer to the two nodes of an element K_e by

$$\mathsf{r}^{(e,1)} \;<\; \mathsf{r}^{(e,2)}\,, \tag{6.26}$$

We write the restrictions of v_h, w_h and λ to an element K_e as

$$v_h^{K_e} \quad , \quad w_H^{K_e}\,, \qquad \lambda^{K_e} = \lambda|_{K_e} = \begin{pmatrix}\lambda^{(e,1)}\\ \lambda^{(e,2)}\end{pmatrix}\,. \tag{6.27}$$

Local problem for an interior element Consider interior interval K_e, it means that $e = 2,\ldots,N-1$. The interval K_e has a neighbor K_{e-1} on the left and K_{e+1} on the right. The two nodes of the element K_e are further referred to as $\mathsf{r}^{(e,1)}$ and $\mathsf{r}^{(e,2)}$ for the left and right nodes respectively. The conservativity condition (6.12) is written as, using the notation of (6.27) for λ,

$$\begin{cases} \left(v_h^{K_e} \;+\; \tau^{K_e}\, w_h^{K_e} \;-\; \tau^{K_e}\,\lambda^{(e,1)}\right)\,\nu^{K_e}\big(\mathsf{r}^{(e,1)}\big) \\ \qquad\qquad + \left(v_h^{K_{e-1}} \;+\; \tau^{K_{e-1}}\, w_h^{K_{e-1}} \;-\; \tau^{K_{e-1}}\,\lambda^{(e-1,2)}\right)\,\nu^{K_{e-1}}\big(\mathsf{r}^{(e,1)}\big) \;=\; 0\,; \\ \left(v_h^{K_{e+1}} \;+\; \tau^{K_{e+1}}\, w_h^{K_{e+1}} \;-\tau^{K_{e+1}}\,\lambda^{(e+1,2)}\right)\,\nu^{K_{e+1}}\big(\mathsf{r}^{(e,2)}\big) \\ \qquad\qquad + \left(v_h^{K_e} \;+\; \tau^{K_e}\, w_h^{K_e} \;-\; \tau^{K_e}\,\lambda^{(e,2)}\right)\,\nu^{K_e}\big(\mathsf{r}^{(e,2)}\big) \;=\; 0\,. \end{cases} \tag{6.28}$$

Local problem for a boundary interval Specific to one-dimensional case, there are only two boundary elements, labeled to as K_1 and K_N. One of the two nodes of the boundary element is an interior one, where the conservativity condition is imposed. On the nodal boundary, one imposes the selected boundary condition from Table 1. For instance, at the element K_1 where the limit at the origin $\lim_{r\to 0} v = 0$ is imposed, we have

$$\begin{cases} \left(v_h^{K_1} \;+\; \tau^{K_1}\, w_h^{K_1} \;-\; \tau^{K_1}\,\lambda^{(1,1)}\right)\,\nu^{K_1}\big(\mathsf{r}^{(1,1)}\big) \;=\; 0\,; \\ \big(v_h^{K_2} \;+\; \tau^{K_2}\, w_h^{K_2} \;-\tau^{K_2}\,\lambda^{(2,1)}\big)\,\nu^{K_2}\big(\mathsf{r}^{(1,2)}\big) \\ \qquad\qquad + \big(v_h^{K_1} \;+\; \tau^{K_e}\, w_h^{K_1} \;-\tau^{K_e}\,\lambda^{(e,2)}\big)\,\nu^{K_e}\big(\mathsf{r}^{(1,2)}\big) \;=\; 0\,. \end{cases} \tag{6.29}$$

At the element K_N where the radiation boundary condition is imposed, we have

$$\begin{cases} \left(v_h^{K_N} \;+\; \tau^{K_N}\, w_h^{K_N} \;-\; \tau^{K_N}\,\lambda^{(N,1)}\right)\,\nu^{K_N}\big(\mathsf{r}^{(N,1)}\big) \\ \qquad\qquad + \left(v_h^{K_{N-1}} \;+\; \tau^{K_{N-1}}\, w_h^{K_{N-1}} \;-\; \tau^{K_{N-1}}\,\lambda^{(N-1,2)}\right)\,\nu^{K_{N-1}}\big(\mathsf{r}^{(N,1)}\big) \;=\; 0\,; \\ \left(v_h^{K_N} \;+\; \tau^{K_N}\, w_h^{K_N} \;-\; \tau^{K_N}\,\lambda^{(N,2)}\right)\,\nu^{K_N}\big(\mathsf{r}^{(N,2)}\big) \;=\; \left(-\dfrac{1}{\mathsf{r}^{(N,2)}} + \mathbf{Z}_{\bullet}\right)\; w_h^{K_N}\,\nu^{K_N}\big(\mathsf{r}^{(N,2)}\big)\,. \end{cases} \tag{6.30}$$

6.3.3 Statement of the approximate problem

Using the HDG method, the approximate problem is the following.

Find (w_h, v_h, λ) that solves

1. The local volume problem (6.20) on each interval K_e for $e = 1, \dots N$,
2. together with the interface/nodal problem made of (6.28) and of the appropriate boundary conditions such as, e.g., (6.29) and (6.30).

6.4 Discretization

6.4.1 Domain partition and discretization basis

Partition We start by creating a partition of the interval $[r_{\min}, r_{\max}]$ with nodes $\mathsf{r}_1 = 0, \dots, \mathsf{r}_{N+1} = r_{\max}$, which set is denoted by $\Sigma = \{\mathsf{r}_1, \dots, \mathsf{r}_{N+1}\}$.

1. This gives the N elements/intervals K_e for $e = 1, \dots N$, with
$$K_e = [\mathsf{r}^{(e,1)}, \, \mathsf{r}^{(e,2)}] = [\mathsf{r}_e \, , \; \mathsf{r}_{e+1}] \quad \text{of length } h_e = \mathsf{r}_{e+1} - \mathsf{r}_e \, . \tag{6.31}$$
2. Assign the discretization order (polynomial order) for each interval K_e. Denote this sequence by $\mathsf{p}_1 \, , \, \dots, \, , \, \mathsf{p}_N$.
3. On the element K_e, associated with polynomial degree p_e and m_e local degrees of freedom, denote the associated basis on K_e by
$$\phi_1^e \, , \; \dots \; , \; \phi_\ell^e \, , \; \dots \; , \; \phi_{m_e}^e \, . \tag{6.32}$$
Using the Lagrange polynomials basis, we have $m_e \; = \; \mathsf{p}_e + 1$.

Discrete unknowns The unknowns are represented as a polynomial on each element K_e such that
$$w_h^{K_e} \; := \; \sum_{\ell=1}^{m_e} \mathsf{W}_\ell^{K_e} \phi_\ell^{K_e} \, ; \qquad v_h^{K_e} \; := \; \sum_{\ell=1}^{m_e} \mathsf{V}_\ell^{K_e} \phi_\ell^{K_e} \, . \tag{6.33}$$

The numerical trace is represented by a vector $\boldsymbol{\lambda}$ of length $N+1$ with
$$\boldsymbol{\lambda} \; = \; \big(\lambda_1, \dots, \lambda_3, \dots, \lambda_{N+1}\big) \, . \tag{6.34}$$

Note that here we have a global indexing for $\boldsymbol{\lambda}$. Since we are in one dimension, the number of degrees of freedom for $\boldsymbol{\lambda}$ is $N_{\text{dof}} \; := \; N+1$. The restriction of $\boldsymbol{\lambda}$ to the interval K_e is
$$\boldsymbol{\lambda}^e \; := \; \boldsymbol{\lambda}|_{K_e} \; = \; \begin{pmatrix} \lambda^{(e,1)} \\ \lambda^{(e,2)} \end{pmatrix} \, . \tag{6.35}$$

For a generic element K, we also use notation for the restriction of $\boldsymbol{\lambda}$,
$$\boldsymbol{\lambda}|_K \; = \; \begin{pmatrix} \lambda_1^K \\ \lambda_2^K \end{pmatrix} \, . \tag{6.36}$$

Connectivity map The connection map relates the global indexing of $\boldsymbol{\lambda}$ to the nodes of an element. We define
$$\beta(e,i) = 2(e-1) + i \quad , \quad 1 \leq e \leq N \; , \; i = 1,2 \tag{6.37}$$
such that the global index for the node i of the element e is given by $\beta(e,i)$. The above definition also implies,
$$\beta(e,2) \; = \; \beta(e,1) \, + \, 1 \quad , \quad 1 \leq e \leq N \, . \tag{6.38}$$

We define the *connectivity operator* $\mathcal{A}$ which gives the restriction to an element K^e,
$$\mathcal{A} \; := \; \begin{pmatrix} \mathcal{A}^1 \\ \vdots \\ \mathcal{A}^N \end{pmatrix} \tag{6.39}$$

Its components are defined as follows. With operator β defined in (6.37), we have,

$$\begin{aligned} &\text{for a vector of length } N_{\text{dof}} \ \mathbf{x} = \begin{pmatrix} x_1 \\ \vdots \\ x_{N_{\text{dof}}} \end{pmatrix}, \\ \mathcal{A}^e\,\mathbf{x} \ &= \ \begin{pmatrix} x_j \\ x_{j+1} \end{pmatrix} \quad \text{where} \quad j \text{ is such that} \quad j = \beta(e,1)\,. \end{aligned} \tag{6.40}$$

That $j+1 = \beta(e,2)$ is due to (6.38).

We also give the action of its transpose that goes from a local index to the global one (for the degree of freedom of the numerical trace $\boldsymbol{\lambda}$),

$$(\mathcal{A}^e)^t \begin{pmatrix} a \\ b \end{pmatrix} \ = \ a\,\mathbf{e}_j \ + \ b\,\mathbf{e}_{j+1}\,. \tag{6.41}$$

Here, $\mathbf{e}_i$ is the column unit vector of size m_K whose components are zero except at position i, we have:

$$\mathbb{e}_i\,, \quad \mathbf{e}_i \qquad \text{elementary row and column unit vector respectively.} \tag{6.42}$$

6.4.2 Discretization of the local problem

Consider the local volume problem (6.20) on an interval K with

$$K \ = \ [\mathsf{r}_1^K\ ,\ \mathsf{r}_2^K]\,, \qquad \partial K = \{\mathsf{r}_1^K\ ,\ \mathsf{r}_2^K\} \tag{6.43}$$

with outward pointing normal $\nu_{\partial K}$,

$$\nu_1^K \ := \ \nu_{\partial K}(\mathsf{r}_1^K) = -1 \quad , \quad \nu_2^K \ := \ \nu_{\partial K}(\mathsf{r}_2^K) = 1\,. \tag{6.44}$$

$\boxed{\textbf{Step 1}}$ For the local volume problem (6.20), we replace w_h and v_h by their approximation forms of (6.33), and the restriction (6.36) of λ to K. We rewrite the boundary term in (6.20a)

$$\begin{aligned} &-\ \tau^K \sum_{\mathsf{r}\in\partial K} (r^2\,\phi_k^K)|_{\mathsf{r}}\,\big(w_h\,\nu_{\partial_K} \ - \ \lambda\,\nu_{\partial_K}\big)|_{\mathsf{r}} \\ &\qquad = \ -\ \tau^K \sum_{\mathsf{r}\in\partial K} (r^2\,\phi_k^K)|_{\mathsf{r}}\,\big(w_h\,\nu_{\partial_K}\big)|_{\mathsf{r}} \ + \ \tau^K \sum_{\mathsf{r}\in\partial K} (r^2\,\phi_k^K)|_{\mathsf{r}}\,\big(\lambda\,\nu_{\partial_K}\big)|_{\mathsf{r}}\,. \end{aligned}$$

The first term on the right-hand side can be written as

$$\begin{aligned} -\ \tau^K &\sum_{\mathsf{r}\in\partial K} (r^2\,\phi_k^K)|_{\mathsf{r}}\,\big(w_h\,\nu_{\partial_K}\big)|_{\mathsf{r}} \\ &= \ -\tau^K\,(\mathsf{r}_2^K)^2\,\phi_k^K(\mathsf{r}_2^K)\,\nu_2^K \sum_{\ell=1}^{m_K} \mathsf{W}_\ell^K\,\phi_\ell^K(\mathsf{r}_2^K) \ - \ \tau^K\,(\mathsf{r}_1^K)^2\,\phi_k^K(\mathsf{r}_1^K)\,\nu_1^K \sum_{\ell=1}^{m_K} \mathsf{W}_\ell^K\,\phi_\ell^K(\mathsf{r}_1^K) \\ &= \ -\tau^K\,(\mathsf{r}_2^K)^2\,\delta_{k\,m_K} \sum_{\ell=1}^{m_K} \mathsf{W}_\ell^K\,\delta_{\ell\,m_K} \ + \ \tau^K\,(\mathsf{r}_1^K)^2\,\delta_{k\,1} \sum_{\ell=1}^{m_K} \mathsf{W}_\ell^K\,\delta_{l\,1} \\ &= \ -\tau^K\,(\mathsf{r}_2^K)^2\,\delta_{k\,m_K}\,\mathsf{W}_{m_K}^K \ + \ \tau^K\,(\mathsf{r}_1^K)^2\,\delta_{k1}\,\mathsf{W}_1^K\,. \end{aligned} \tag{6.45}$$

Here we have used the definition of the Lagrangian polynomial. Note that r_1^K is the start point of K, and in the index of the basis this corresponds to 1, while r_2^K is the end point and in the index of the basis this corresponds to m_K, thus

$$\phi_\ell^K(\mathsf{r}_1^K) \ = \ \delta_{\ell\,1}\,, \qquad \phi_\ell^K(\mathsf{r}_2^K) \ = \ \delta_{\ell\,m_K}\,. \tag{6.46}$$

Similarly, for the second term in the right-hand side, we use

$$\lambda|_{\mathsf{r}_1^K} \ = \ \lambda_1^K\,, \qquad \lambda|_{\mathsf{r}_2^K} \ = \ \lambda_2^K\,, \tag{6.47}$$

and obtain

$$\begin{aligned}\tau^K \sum_{\mathsf{r}\in\partial K} (r^2\,\phi_k^K)|_{\mathsf{r}}\,\big(\lambda\,\nu_{\partial_K}\big)|_{\mathsf{r}} = {} & \nu_2^K\,\tau^K\,(\mathsf{r}_2^K)^2\,\phi_k^K(\mathsf{r}_2^K)\,\lambda_2^K \;+\; \nu_1^K\,\tau^K\,(\mathsf{r}_1^K)^2\,\phi_k^K(\mathsf{r}_1^K)\,\lambda_1^K \\ = {} & \tau^K\,(\mathsf{r}_2^K)^2\,\delta_{km_K}\,\lambda_2^K \;-\; \tau^K\,(\mathsf{r}_1^K)^2\,\delta_{k1}\,\lambda_1^K\,.\end{aligned} \tag{6.48}$$

The boundary term in (6.20b) is

$$\sum_{\mathsf{r}\in\partial K}(r\,\phi\,\lambda\,\nu_{\partial K})|_{\mathsf{r}} \;=\delta_{k\,m_K}\;\nu_2^K\lambda_2^K\,\mathsf{r}_2^K \;+\; \delta_{k1}\;\nu_1^K\;\lambda_1^K\,\mathsf{r}_1^K \;=\; \delta_{km_K}\;\lambda_2^K\,\mathsf{r}_2^K \;-\; \delta_{k1}\;\lambda_1^K\,\mathsf{r}_1^K\,. \tag{6.49}$$

The discretized version of equation (6.20) in the basis $\{\phi_\ell^K\}$ using test functions $\{\phi_k^K\}$ is

$$\left\{\begin{aligned}
& -\sum_{\ell=1}^{m_K}\mathsf{V}_\ell^K\int_K\big(\phi_\ell^K \;+\; r\,(\phi_\ell^K)'\big)\,r\,\phi_k^K \;+\;\sum_{\ell=1}^{m_K}\mathsf{W}_\ell^K\int_K Q\,\phi_\ell^K\,\phi_k^K \\
&\qquad\qquad -\tau^K\,(\mathsf{r}_2^K)^2\;\delta_{k\,m_K}\;\mathsf{W}_{m_K}^K \;+\;\tau^K\,(\mathsf{r}_1^K)^2\;\delta_{k1}\;\mathsf{W}_1^K \\
&\qquad\qquad +\;\tau^K\,(\mathsf{r}_2^K)^2\;\delta_{k\,m_K}\;\lambda_2^K \;-\;\tau^K\,(\mathsf{r}_1^K)^2\;\delta_{k1}\;\lambda_1^K \;=\;\int_K r\,g\,\phi_k^K\,; && \text{(6.50a)}\\
& \sum_{\ell=1}^{m_K}\mathsf{W}_\ell^K\int_K\phi_\ell^K\,(\phi_k^K \;+\; r\,(\phi_k^K)') \;+\;\sum_{\ell=1}^{m_K}\mathsf{W}_\ell^K\int_K\phi_\ell^K\,\phi_k^K \\
&\qquad\qquad -\;\delta_{k\,m_K}\;\lambda_2^K\,\mathsf{r}_2^K \;+\;\delta_{k1}\;\lambda_1^K\,\mathsf{r}_1^K \;+\;\sum_{\ell=1}^{m_K}\mathsf{V}_\ell^K\int_K r\,\phi_\ell^K\,\phi_k^K \;=\;0 && \text{(6.50b)}
\end{aligned}\right.$$

with unknowns

$$\mathsf{W}^K \quad,\quad \mathsf{V}^K \quad,\quad \lambda_1^K \quad,\quad \lambda_2^K\,. \tag{6.51}$$

Recall that $\delta_{ij}=1$ for $i=j$ and 0 for $i\neq j$.

Step 2 We next write problem (6.50) in matrix form. Note that each row of the local matrix and right-hand side comes from testing with the test function ϕ_k^K for $k=1,\dots,m_K$. The column varies with the degree of freedom of the unknowns (6.51).

Definition of local matrices Define the following local matrices of size $m_K\times m_K$. The first equation in (6.50a) uses matrices

$$\mathbb{T}_{k\ell}^K \;:=\; \int_K\big(\phi_\ell^K \;+\; r\,(\phi_\ell^K)'\big)\,r\,\phi_k^K\,, \tag{6.52}$$

and

$$\mathbb{Q}_{k\ell}^K \;:=\; \int_K\phi_\ell^K\,Q\,\phi_k^K\,; \tag{6.53}$$

The second one (6.50b) uses

$$\mathbb{S}_{k\ell}^K \;:=\; \int_K\phi_\ell^K\,(2\,\phi_k^K \;+\; r\,(\phi_k^K)') \quad,\quad \mathbb{M}_{k\ell}^K \;:=\; \int_K r\,\phi_\ell^K\,\phi_k^K\,. \tag{6.54}$$

To capture the boundary terms, we define

$$\mathbb{R}^K \;:=\; -\,(\mathsf{r}_2^K)^2\,\mathbb{E}_{m_K m_K} \;+\; (\mathsf{r}_1^K)^2\,\mathbb{E}_{11}\,. \tag{6.55}$$

Here, we have used elementary matrices $\mathbb{E}_{ij}$ whose components are zero except at position (i,j) where they are equal to 1.

Matrix form of local volume problem The matrix form of problem (6.50) is

$$\mathbb{A}^K \begin{pmatrix} \mathsf{V}^K \\ \mathsf{W}^K \end{pmatrix} + \mathbb{C}^K \begin{pmatrix} \lambda_1^K \\ \lambda_2^K \end{pmatrix} = \begin{pmatrix} \mathsf{F}^K \\ \mathbf{0} \end{pmatrix} . \tag{6.56}$$

Here $\mathbf{0}$ is a column vector of size m_K. The unknowns are the local vectors of size m_K,

$$\mathsf{V}^K = \begin{pmatrix} \mathsf{V}_1^K \\ \vdots \\ \mathsf{V}_{m_K}^K \end{pmatrix} , \quad \mathsf{W}^K = \begin{pmatrix} \mathsf{W}_1^K \\ \vdots \\ \mathsf{V}_{m_K}^K \end{pmatrix} \quad \text{and} \quad \begin{pmatrix} \lambda_1^K \\ \lambda_2^K \end{pmatrix} . \tag{6.57}$$

The equation (6.50a) contributes the first block (of size $m_K \times m_K$), and (6.50b) to the second block. The matrix $\mathbb{A}^K$ is of size $(2m_K) \times (2m_K)$ and defined as

$$\mathbb{A}^K := \begin{pmatrix} -\mathbb{T}^K & \mathbb{Q}^K + \tau^K \mathbb{R}^K \\ \mathbb{M}^K & \mathbb{S}^K \end{pmatrix} . \tag{6.58}$$

The block $\mathbb{R}^K$ is contributed by (6.45). We define matrix $\mathbb{C}^K$ of size $(2m_K) \times 2$,

$$\mathbb{C}^K := \begin{pmatrix} -\,\tau^K\,(\mathsf{r}_1^K)^2\,\mathbf{e}_1 & \tau^K\,(\mathsf{r}_2^K)^2\,\mathbf{e}_{m_K} \\ \mathsf{r}_1^K\,\mathbf{e}_1 & -\mathsf{r}_2^K\,\mathbf{e}_{m_K} \end{pmatrix} , \tag{6.59}$$

where $\mathbf{e}_i$ is the column unit vector of size m_K whose components is zero except at position i. The upper block comes from the contribution of (6.48) and the second one from (6.49). The upper block of the local right-hand side is

$$\mathsf{F}^K = \begin{pmatrix} \mathsf{F}_1^K \\ \dots \\ \mathsf{F}_{m_K}^K \end{pmatrix} , \qquad \mathsf{F}_k^K := \int_K r\,g\,\phi_k^K . \tag{6.60}$$

6.4.3 Discretization of the local interface and boundary problem

$\boxed{\textbf{Step 1}}$ We first discretize the local interface problem contributed by each interval K_e. We simplify the notation by writing

$$\nu^{K_e}(\mathsf{r}^{(e,1)}) = \nu^{(e,1)} , \qquad \nu^{K_e}(\mathsf{r}^{(e,2)}) = \nu^{(e,2)} . \tag{6.61}$$

We use the basis functions to express $v_h^{K_e}$ and $w_h^{K_e}$,

$$v_h^{K_e} = \sum_{\ell}^{m_e} \mathsf{V}_\ell^e\,\phi_\ell^e \quad , \quad w_h^{K_e} = \sum_{\ell}^{m_e} \mathsf{W}_\ell^e\,\phi_\ell^e , \tag{6.62}$$

then

$$\begin{aligned} v_h^{K_e}(\mathsf{r}^{(e,1)}) &= \mathsf{V}_1^{K_e} ; \\ v_h^{K_{e-1}}(\mathsf{r}^{(e,1)}) &= v_h^{K_{e-1}}(\mathsf{r}^{(e-1,2)}) = \mathsf{V}_{m_e}^{e-1} ; \\ v_h^{K_{e+1}}(\mathsf{r}^{(e,2)}) &= v_h^{K_{e+1}}(\mathsf{r}^{(e+1,1)}) = \mathsf{V}_1^{e+1} ; \\ v_h^{K_e}(\mathsf{r}^{(e,2)}) &= \mathsf{V}_{m_e}^e , \end{aligned}$$

and similarly for $w_h^{K_e}$.

For an interior element Equation (6.28) leads to

$$\begin{cases} \Big(\mathsf{V}^{(e,1)} \;+\; \tau^{e}\,\mathsf{W}^{(e,1)} \;-\tau^{e}\,\lambda^{(e,1)}\Big)\,\nu^{(e,1)} \\ \qquad\qquad + \Big(\mathsf{V}^{(e-1,m_e)} \;+\; \tau^{e-1}\,\mathsf{W}^{(e-1,m_e)} \;-\tau^{e-1}\,\lambda^{(e-1,2)}\Big)\,\nu^{(e-1,2)} \;=\; 0\,; \\ \Big(\mathsf{V}^{(e+1,1)} \;+\; \tau^{e+1}\,\mathsf{W}_1^{e+1} \;-\tau^{e+1}\,\lambda^{(e+1,1)}\Big)\,\nu^{(e+1,1)} \\ \qquad\qquad + \big(\mathsf{V}^{(e,m_e)} \;+\; \tau^{e}\,\mathsf{W}^{(e,m_e)} \;-\tau^{e}\,\lambda^{(e,2)}\big)\,\nu^{(e,2)} \;=\; 0\,. \end{cases} \tag{6.63}$$

With $\mathbf{0}$ is a column vector of length 2, this is rewritten as

$$\mathbb{B}^{e}\begin{pmatrix}\mathsf{V}^{e}\\ \mathsf{W}^{e}\end{pmatrix} \;+\; \mathbb{L}^{e}\begin{pmatrix}\lambda^{(e,1)}\\ \lambda^{(e,2)}\end{pmatrix} \;+\; \mathsf{R}^{e} \;=\; \mathbf{0} \quad , \quad \text{for } e=2,\dots,N-1\,, \tag{6.64}$$

with the local matrices and remainder term defined as follows. The local matrices $\mathbb{B}^{e}$ is of size $2\times(2m_e)$ and is defined as

$$\mathbb{B}^{e} \;:=\; \begin{pmatrix}\nu^{(e,1)}\,\mathbb{e}_1 & \tau^{e}\,\nu^{(e,1)}\,\mathbb{e}_1\\ \nu^{(e,2)}\,\mathbb{e}_{m_e} & \tau^{e}\,\nu^{(e,2)}\,\mathbb{e}_{m_e}\end{pmatrix} \;=\; \begin{pmatrix}\nu^{(e,1)} & \nu^{(e,2)}\end{pmatrix}\begin{pmatrix}\mathbb{e}_1 & \tau^{e}\,\mathbb{e}_1\\ \mathbb{e}_{m_e} & \tau^{e}\,\mathbb{e}_{m_e}\end{pmatrix}\,. \tag{6.65}$$

Local matrix $\mathbb{L}^{e}$ of size 2×2 is defined as,

$$\mathbb{L}^{e} \;:=\; -\tau^{e}\begin{pmatrix}\nu^{(e,1)} & 0\\ 0 & \nu^{(e,2)}\end{pmatrix}\,. \tag{6.66}$$

The remainder term R^{e} is a column vector of length 2 and for $e=2,\dots,N-1$, is equal to

$$\begin{aligned}\mathsf{R}^{e} \;:=\; &\begin{pmatrix}\nu^{(e-1,2)}\,\mathbb{e}_{m_e} & \tau^{e-1}\,\nu^{(e-1,2)}\,\mathbb{e}_{m_e}\\ \mathbf{0}_{1\times m_e} & \mathbf{0}_{1\times m_e}\end{pmatrix}\begin{pmatrix}\mathsf{V}^{e-1}\\ \mathsf{W}^{e-1}\end{pmatrix} + \begin{pmatrix}0 & -\tau^{e-1}\nu^{(e-1,1)}\\ 0 & 0\end{pmatrix}\begin{pmatrix}\lambda^{(e-1,1)}\\ \lambda^{(e-1,2)}\end{pmatrix}\\ &+\begin{pmatrix}\mathbf{0}_{1\times m_e} & \mathbf{0}_{1\times m_e}\\ \nu^{(e+1,1)}\,\mathbb{e}_1 & \tau^{e+1}\,\nu^{(e+1,1)}\,\mathbb{e}_1\end{pmatrix}\begin{pmatrix}\mathsf{V}^{e+1}\\ \mathsf{W}^{e+1}\end{pmatrix} + \begin{pmatrix}0 & 0\\ -\tau^{e+1}\nu^{(e+1,1)} & 0\end{pmatrix}\begin{pmatrix}\lambda^{(e+1,1)}\\ \lambda^{(e+1,2)}\end{pmatrix}.\end{aligned} \tag{6.67}$$

Recall that $\mathbb{e}_i$ is an elementary row vector.

For left boundary interval On the first node K_1 where we impose (6.29), we have

$$\begin{cases} \Big(\mathsf{V}^{(e,1)} \;+\; \tau^{e}\,\mathsf{W}^{(e,1)} \;-\tau^{e}\,\lambda^{(e,1)}\Big)\,\nu^{(e,1)} \;=\; 0\,; \\ \Big(\mathsf{V}^{(e+1,1)} \;+\; \tau^{e+1}\,\mathsf{W}_1^{e+1} \;-\tau^{e+1}\,\lambda^{(e+1,1)}\Big)\,\nu^{(e+1,1)} \\ \qquad + \big(\mathsf{V}^{(e,m_e)} \;+\; \tau^{e}\,\mathsf{W}^{(e,m_e)} \;-\tau^{e}\,\lambda^{(e,2)}\big)\,\nu^{(e,2)} \;=\; 0\,. \end{cases} \tag{6.68}$$

The local problem is also of the form

$$\mathbb{B}^{1}\begin{pmatrix}\mathsf{V}^{1}\\ \mathsf{W}^{1}\end{pmatrix} \;+\; \mathbb{L}^{1}\begin{pmatrix}\lambda^{(1,1)}\\ \lambda^{(1,2)}\end{pmatrix} \;+\; \mathsf{R}^{1} \;=\; \mathbf{0}_{2\times 1}\,. \tag{6.69}$$

The matrices $\mathbb{B}^1$ and $\mathbb{L}^1$ are defined as in (6.65) and (6.66). Since there is no contribution from the left, and only from the right (from K_2)

$$\mathsf{R}^{1} \;:=\; \begin{pmatrix}\mathbf{0}_{1\times m_e} & \mathbf{0}_{1\times m_e}\\ \nu^{(2,1)}\,\mathbb{e}_1 & \tau^{2}\,\nu^{(2,1)}\,\mathbb{e}_1\end{pmatrix}\begin{pmatrix}\mathsf{V}^{2}\\ \mathsf{W}^{2}\end{pmatrix} + \begin{pmatrix}0 & 0\\ -\tau^{2}\nu^{(2,1)} & 0\end{pmatrix}\begin{pmatrix}\lambda^{(2,1)}\\ \lambda^{(2,2)}\end{pmatrix}. \tag{6.70}$$

For right boundary interval On the final element K_N, the system depends on the choice of boundary conditions, for instance, for the radiation boundary condition (6.30), we have

$$\begin{cases} \left(\mathsf{V}^{(N,1)} + \tau^N \mathsf{W}^{(N,1)} - \tau^N \lambda^{(N,1)}\right) \nu^{(N,1)} \\ \qquad\qquad + \left(\mathsf{V}^{(N-1,m_e)} + \tau^{N-1} \mathsf{W}^{(N-1,m_N)} - \tau^{N-1} \lambda^{(N-1,2)}\right) \nu^{(N-1,2)} = 0\,; \\ (\mathsf{V}^{(N,m_N)} + \tau^N \mathsf{W}^{(N,m_N)} - \tau^N \lambda^{(N,2)})\, \nu^{(N,2)} = \left(-\dfrac{1}{\mathsf{r}^{(N,2)}} + \mathsf{Z}\right) \lambda^{(N,2)} \nu^{(N,2)}\,. \end{cases} \tag{6.71}$$

Therefore, the local interface/boundary problem for K_N is of the form

$$\mathbb{B}^N \begin{pmatrix} \mathsf{V}^N \\ \mathsf{W}^N \end{pmatrix} + \mathbb{L}^N \begin{pmatrix} \lambda^{(N,1)} \\ \lambda^{(N,2)} \end{pmatrix} + \mathsf{R}^N = \mathbf{0}_{2\times 1}\,, \tag{6.72}$$

where $\mathbb{B}^N$ is defined as in (6.65). However $\mathbb{L}^N$ is different due to the boundary condition, such that

$$\mathbb{L}^N := \begin{pmatrix} -\tau^N \nu^{(N,1)} & 0 \\ 0 & \left(\dfrac{1}{\mathsf{r}^{(N,2)}} - \mathsf{Z} - \tau^N\right) \nu^{(N,2)} \end{pmatrix}, \qquad \text{radiation boundary condition}\,. \tag{6.73}$$

In addition, there is no contribution from the right, thus the remainder term takes the form,

$$\mathsf{R}^N := \begin{pmatrix} \nu^{(N-1,2)}\, \mathbb{e}_{m_N} & \tau^{N-1}\, \nu^{(N-1,2)}\, \mathbb{e}_{m_N} \\ \mathbf{0}_{1\times m_e} & \mathbf{0}_{1\times m_e} \end{pmatrix} \begin{pmatrix} \mathsf{V}^{N-1} \\ \mathsf{W}^{N-1} \end{pmatrix} + \begin{pmatrix} 0 & -\tau^{N-1}\nu^{(N-1,1)} \\ 0 & 0 \end{pmatrix} \begin{pmatrix} \lambda^{(N-1,1)} \\ \lambda^{(N-1,2)} \end{pmatrix}. \tag{6.74}$$

On the other hand, assuming a Dirichlet boundary condition on w, one has

$$\begin{cases} \left(\mathsf{V}^{(N,1)} + \tau^N \mathsf{W}^{(N,1)} - \tau^N \lambda^{(N,1)}\right) \nu^{(N,1)} \\ \qquad\qquad + \left(\mathsf{V}^{(N-1,m_e)} + \tau^{N-1} \mathsf{W}^{(N-1,m_N)} - \tau^{N-1} \lambda^{(N-1,2)}\right) \nu^{(N-1,2)} = 0\,; \\ \lambda^{(N,2)} = 0\,. \end{cases} \tag{6.75}$$

As a result of this, the local interface/boundary problem for K^N is of the same form of as in (6.72), however $\mathbb{B}^N$ and $\mathbb{L}^N$ are different and are given by,

$$\mathbb{B}^N := \begin{pmatrix} \nu^{(N,1)}\, \mathbb{e}_1 & \tau^N\, \nu^{(N,1)}\, \mathbb{e}_1 \\ \mathbf{0}_{1\times m_N} & \mathbf{0}_{1\times m_N} \end{pmatrix}; \qquad \mathbb{L}^N := \begin{pmatrix} -\tau^N \nu^{(N,1)} & 0 \\ 0 & 1 \end{pmatrix}. \tag{6.76}$$

$\boxed{\textbf{Step 2}}$ We put together the local interface and boundary problems into a global form by using the connectivity operator $\mathcal{A}$ of (6.41). Recall that we have derived the local interface problem contributed by each interval K_e,

$$\mathbb{B}^e \begin{pmatrix} \mathsf{V}^e \\ \mathsf{W}^e \end{pmatrix} + \mathbb{L}^e \begin{pmatrix} \lambda^{(e,1)} \\ \lambda^{(e,2)} \end{pmatrix} + \mathbb{R}^e = 0\,. \tag{6.77}$$

To derive the problem for $\boldsymbol{\lambda}$, we sum them up according to the correct contribution

$$\sum_{e=1}^{N} (\mathcal{A}^e)^t \left(\mathbb{B}^e \begin{pmatrix} \mathsf{V}^e \\ \mathsf{W}^e \end{pmatrix} + \mathbb{L}^e \begin{pmatrix} \lambda^{(e,1)} \\ \lambda^{(e,2)} \end{pmatrix} + \mathbb{R}^e \right) = 0\,. \tag{6.78}$$

This gives[5]

$$\sum_{e=1}^{N} (\mathcal{A}^e)^t \left(\mathbb{B}^e \begin{pmatrix} \mathsf{V}^e \\ \mathsf{W}^e \end{pmatrix} \;+\; \mathbb{L}^e \begin{pmatrix} \lambda^{(e,1)} \\ \lambda^{(e,2)} \end{pmatrix} \right) \;=\; 0\,. \tag{6.79}$$

6.5 Summary of discretized HDG formulation and algorithms

Here, we retain only the global index of the interval K_e, and write

$$\lambda_1^{K_e} \;=\; \lambda^{(e,1)}\,, \qquad \lambda_2^{K_e} \;=\; \lambda^{(e,2)}\,, \qquad \mathsf{V}^{K_e} = \mathsf{V}^e\,, \qquad \mathsf{W}^{K_e} = \mathsf{W}^e\,. \tag{6.80}$$

We have introduced the restriction to K_e of the vector $\boldsymbol{\lambda}$. We proceed similarly for the volume unknowns (discretizing w_h and v_h),

$$\mathbf{W}^e := \begin{pmatrix} \mathsf{V}^e \\ \mathsf{W}^e \end{pmatrix}\,, \qquad \boldsymbol{\lambda}^e = \begin{pmatrix} \lambda^{(e,1)} \\ \\ \lambda^{(e,2)} \end{pmatrix}\,. \tag{6.81}$$

6.5.1 Local volume problem

From (6.50), we have obtained the local volume problem on an interval K_e, for $e = 1, \ldots, N$,

$$\mathbb{A}^e\,\mathbf{W}^e \;+\; \mathbb{C}^K\,\boldsymbol{\lambda}^e \;=\; \begin{pmatrix} \mathsf{F}^e \\ 0 \end{pmatrix}\,.$$

with $\mathbb{A}^e$ defined by (6.58), $\mathbb{C}^e$ by (6.59) and F^e by (6.60). We can solve for W^e,

$$\mathbf{W}^e \;=\; -(\mathbb{A}^e)^{-1}\,\mathbb{C}^K\,\boldsymbol{\lambda}^e \;+\; (\mathbb{A}^e)^{-1}\begin{pmatrix} \mathsf{F}^e \\ 0 \end{pmatrix}\,. \tag{6.82}$$

6.5.2 Conservativity problem

From (6.79), we have obtained the conservativity condition and boundary conditions (at the left and right boundary),

$$\sum_{e=1}^{N} (\mathcal{A}^e)^t\,(\mathbb{B}^e\,\mathbf{W}^e \;+\; \mathbb{L}^e\boldsymbol{\lambda}^e) \;=\; \mathbf{0}_{N_{\text{dof}}\times 1}\,. \tag{6.83}$$

Use (6.82) to replace W^e in terms of $\boldsymbol{\lambda}^e$,

$$\sum_{e=1}^{N} (\mathcal{A}^e)^t \left(\mathbb{B}^e \Big(-(\mathbb{A}^e)^{-1}\mathbb{C}^K\boldsymbol{\lambda}^e \;+\; (\mathbb{A}^e)^{-1}\begin{pmatrix} \mathsf{F}^e \\ \mathbf{0}_{m_e\times 1} \end{pmatrix} \Big) \;+\; \mathbb{L}^e\boldsymbol{\lambda}^e \right) \;=\; \mathbf{0}_{N_{\text{dof}}\times 1}\,.$$

---

[5] When count in terms of K_e, each condition at the interior, i.e. for r_j with $j = 2, \ldots, N$, is already doubled up. Thus summing up gives

$$\sum_{e=1}^{N} (\mathcal{A}^e)^t \left(\mathbb{B}^e \begin{pmatrix} \mathsf{V}^e \\ \mathsf{W}^e \end{pmatrix} \;+\; \mathbb{L}^e \begin{pmatrix} \lambda^{(e,1)} \\ \lambda^{(e,2)} \end{pmatrix} \;+\; \mathbb{R}^e \right) = \sum_{e=1}^{N} (\mathcal{A}^e)^t \left(\tilde{\mathbb{B}}^e \;+\; \tilde{\mathbb{L}}^e \begin{pmatrix} \lambda^{(e,1)} \\ \lambda^{(e,2)} \end{pmatrix} \right)\,.$$

where, for an interior element,

$$e = 1\,, \quad \tilde{\mathbb{B}}^e = 2\mathbb{B}^e\,, \qquad \tilde{\mathbb{L}}^e = 2\mathbb{L}_e\,.$$

For the boundary elements K_1 and K_N, we have

$$\tilde{\mathbb{B}}^1 \;=\; \begin{pmatrix} \nu^{(e,1)}\,\mathbb{e}_1 & \tau^e\,\nu^{(e,1)}\,\mathbb{e}_1 \\ 2\nu^{(e,2)}\,\mathbb{e}_{m_e} & 2\tau^e\,\nu^{(e,2)}\,\mathbb{e}_{m_e} \end{pmatrix}\,, \qquad \tilde{\mathbb{L}}^1 \;:=\; -\tau^e \begin{pmatrix} \nu^{(e,1)} & 0 \\ 0 & 2\nu^{(e,2)} \end{pmatrix}\,,$$

and

$$\tilde{\mathbb{B}}^N \;=\; \begin{pmatrix} 2\nu^{(e,1)}\,\mathbb{e}_1 & 2\tau^e\,\nu^{(e,1)}\,\mathbb{e}_1 \\ \nu^{(e,2)}\,\mathbb{e}_{m_e} & \tau^e\,\nu^{(e,2)}\,\mathbb{e}_{m_e} \end{pmatrix}\,, \qquad \tilde{\mathbb{L}}^N \;:=\; -\tau^e \begin{pmatrix} 2\nu^{(e,1)} & 0 \\ 0 & \nu^{(e,2)} \end{pmatrix}\,.$$

We move all terms acting as a right-hand side to the right:

$$\sum_{e=1}^{N}(\mathcal{A}^e)^t \;\; \mathbb{K}^e \; \boldsymbol{\lambda}^e \;=\; \sum_{e=1}^{N}(\mathcal{A}^e)^t \;\mathsf{S}^e\,. \tag{6.84}$$

Here, we have defined the local matrix $\mathbb{K}^e$ of size 2×2,

$$\mathbb{K}^e \;:=\; -\mathbb{B}^e\,(\mathbb{A}^e)^{-1}\,\mathbb{C}^e \;+\; \mathbb{L}^e\,, \tag{6.85}$$

and the local source S^e,

$$\mathsf{S}^e \;:=\; -\mathbb{B}^e\,(\mathbb{A}^e)^{-1}\begin{pmatrix}\mathsf{F}^e \\ \mathbf{0}_{m_e\times 1}\end{pmatrix}. \tag{6.86}$$

Note that there is only the contribution of the volume source here.

6.5.3 Global problem

Replace $\boldsymbol{\lambda}^e = \mathcal{A}^e\boldsymbol{\lambda}$ in (6.84). The global unknown $\boldsymbol{\lambda}$ solves

$$\mathbb{K}\,\boldsymbol{\lambda} \;=\; \mathsf{S}\,, \tag{6.87}$$

where the global matrix $\mathbb{K}$ is of size $N_{\text{dof}} \times N_{\text{dof}}$, and the global right-hand side S of size N_{dof},

$$\mathbb{K} \;:=\; \sum_{e=1}^{N}(\mathcal{A}^e)^t\,\mathbb{K}^e\,\mathcal{A}^e\,, \qquad \mathsf{S} \;:=\; \sum_{e=1}^{N}(\mathcal{A}^e)^t\,\mathsf{S}^e\,. \tag{6.88}$$

We review in Algorithms 1 and 2 the overall procedure to solve the global and local problems respectively.

7 Validation of the HDG implementation

To validate our implementation, we compare with the analytical solutions that are obtained for different combinations of boundary conditions. We first consider the boundary value problems, and the delta-Dirac source is studied in Subsection 7.3, where we also compare between the Approaches 1 and 2. Here, the analytical solutions are given for the solution u while our computations are done with the unknowns $(w,\, v)$ of the first-order problem (6.6). We remind the relations between those unknowns already given in (6.2):

$$w \;:=\; r\,u\,, \qquad v \;:=\; r\,u'\,. \tag{7.1}$$

The correspondence between boundary conditions is given in Table 1.

To evaluate the accuracy, we compute the relative error in the same way as (5.21), and define

$$\mathcal{E}_w \;=\; \frac{\|w_{\text{ref}} \;-\; w_{\text{HDG}}\|_{L^2}}{\|w_{\text{ref}}\|_{L^2}}\,, \tag{7.2}$$

and similarly for v, where the indexes 'ref' and 'HDG' refers to the reference solution and the numerical one respectively.

7.1 Validation problems with zero sources

Analytical solutions can be derived in the case of homogeneous medium parameters (i.e., constant) and depend on the choice of boundary conditions, as was done in Subsection 5.3 to investigate the efficiency of the boundary conditions. For the validation of our HDG implementation, we will work with the `Pure atmo` operator, obtained from (4.28a) and (4.29) using the potential

$$\frac{Q_\ell^{\text{Atmo}}}{r^2} \;=\; -\mathsf{k}^2 \;+\; \frac{\alpha_\infty}{r} \;+\; \frac{\ell(\ell+1)}{r^2}\,. \tag{7.3}$$

```
for $e \leftarrow 1$ to $N$ do
    With interpolation degree $\mathsf{p}_e$, compute matrices of size $m_e = \mathsf{p}_e + 1$: $\mathbb{T}^e$ (6.52), $\mathbb{Q}^e$ (6.53), $\mathbb{S}^e$
     and $\mathbb{M}^e$ in (6.54) ;
    /* Construction of local matrix $\mathbb{K}^e$                                         */
    Compute matrices $\mathbb{A}^e$ defined by (6.58), $(\mathbb{A}^e)^{-1}$;
    Compute matrix $\mathbb{C}^e$ defined by (6.59) ;
    /* Computation of $\mathbb{B}^e$ and $\mathbb{L}^e$                                        */
    Compute matrix $\mathbb{B}^e$ for $e = 1, \dots, N-1$ defined by (6.65) ;
    Compute matrix $\mathbb{L}^e$ defined by (6.66) for $e = 1, \dots, N-1$ ;
    Compute $\mathbb{B}^N$ according to boundary condition ;
    Compute $\mathbb{L}^N$ according to boundary condition ;
    Compute matrix $\mathbb{K}^e = -\mathbb{B}^e\,(\mathbb{A}^e)^{-1}\,\mathbb{C}^e \;+\; \mathbb{L}^e$;
    /* Construction of global matrix $\mathbb{K}$ (6.88) using the definition of the
       connectivity matrix (6.40) and its transpose (6.41)                            */
    for $k \leftarrow 1$ to $2$ do
        for $\ell \leftarrow 1$ to $2$ do
            $i \;=\; 2(e-1) \;+\; k$ ;
            $j \;=\; 2(e-1) \;+\; \ell$ ;
            $\mathbb{K}_{ij} \;\leftarrow\; \mathbb{K}_{ij} \;+\; \mathbb{K}^e_{k\ell}$;
        end
    end
    /* Construction of lobal rhs $\mathsf{S}^e$ defined in (6.86)                              */
    Compute upper block $\mathsf{F}^e$ defined by (6.60);
    Compute $\mathsf{S}^e = \;-\mathbb{B}^e\,(\mathbb{A}^e)^{-1} \begin{pmatrix} \mathsf{F}^e \\ \mathbf{0}_{m_e \times 1} \end{pmatrix}$ ;
    /* Construction of global rhs $\mathsf{S}$ (6.88)                                         */
    for $k \leftarrow 1$ to $2$ do
        $i \;=\; 2(e-1) \;+\; k$ ;
        $\mathsf{S}_i \;\leftarrow\; \mathsf{S}_i \;+\; \mathsf{S}^e_k$ ;
    end
end
```

Algorithm 1: Construction of global coefficient matrix $\mathbb{K}$ of size $N_{\mathrm{dof}} \times N_{\mathrm{dof}}$ and global right-hand-side $\mathbb{K}$ of length N_{dof} for linear system (6.87). Recall that $N_{\mathrm{dof}} = N + 1$ where N is the number of intervals in the partitioning of $\Omega = [0, \mathsf{R}]$.

```
/* Resolution                                                                         */
Solve the linear system $\mathbb{K}\boldsymbol{\lambda} = \mathsf{S}$ constructed in Algorithm 1 ;
/* Post-processing                                                                    */
for $e \leftarrow 1$ to $N$ do
    /* Extract $\boldsymbol{\lambda}^e$ from $\boldsymbol{\lambda}$ using and the connectivity operator $\mathcal{A}$ (6.40)          */
    $i \;=\; 2(e-1) \;+\; 1$;
    $\lambda^e_1 \;=\; \boldsymbol{\lambda}_i$;
    $\lambda^e_2 \;=\; \boldsymbol{\lambda}_{i+1}$ ;
    /* Compute the unknowns $\mathsf{W}^e$ and $\mathsf{V}^e$ using (6.82)                             */
    Compute $\begin{pmatrix} \mathsf{V}^e \\ \mathsf{W}^e \end{pmatrix} = -(\mathbb{A}^e)^{-1} \left( \mathbb{C}^K \begin{pmatrix} \lambda^e_1 \\ \lambda^e_2 \end{pmatrix} + \begin{pmatrix} \mathsf{F}^e \\ 0 \end{pmatrix} \right)$ . ;
end
```

Algorithm 2: Resolution (6.87) and post-processing.

and investigate the three following problems, using Dirichlet, Neumann and the radiation boundary conditions.

We first recall how the Whittaker equation is retrieved in this case to provide the exact solutions for our validation tests. To be concise, we rewrite the prototype equation (4.28a) as,

$$\begin{aligned} & -(\,r^2\,u')' \;+\; Q_\ell\,u \;=\; g && \text{(7.4a)}\\ \Leftrightarrow\quad & -r^2\;u'' \;-2\,r\,u' \;+\; Q_\ell\,u \;=\; g && \text{(7.4b)}\\ \Leftrightarrow\quad & -u'' \;-\; \frac{2}{r}u' \;+\; \frac{Q_\ell}{r^2}u \;=\; \frac{g}{r^2}\,. && \text{(7.4c)} \end{aligned}$$

The unknown w defined by

$$u \;=\; \frac{w}{r} \tag{7.5}$$

solves

$$\left(-d_r^2 \;-\; \frac{Q_\ell}{r^2}\right) w \;=\; \frac{g}{r}\,. \tag{7.6}$$

For Q_ℓ of the form (5.9), ODE (7.6) takes the form,

$$\left(-d_r^2 \;-\; \mathsf{k}^2 \;+\; \frac{\alpha_\infty}{r} \;+\; \frac{\ell(\ell+1)}{r^2}\right) w \;=\; \frac{g}{r}\,. \tag{7.7}$$

For $g = 0$, then the generic solutions of the above equation are obtained from the Whittaker equation (2.31) via a change of variable, $z = 2e^{\mathrm{i}\frac{\pi}{2}\,\mathsf{k}\,r}$ cf. [3, Eqn. 2.3, 2.6], and are given as linear combinations of any two of the following three Whittaker functions (depending on the interval where the ODE (7.6) is considered),

$$w(r) \;=\; \mathrm{W}_{-\chi,\ell+1/2}(-2\,\mathrm{i}\,\mathsf{k}\,r) \quad,\quad w(r) \;=\; \mathrm{W}_{\chi,\ell+1/2}(2\,\mathrm{i}\,\mathsf{k}\,r) \quad,\quad w(r) \;=\; \mathrm{M}_{\chi,\ell+1/2}(2\,\mathrm{i}\,\mathsf{k}\,r)\,, \tag{7.8}$$

with

$$\chi \;=\; \frac{\mathrm{i}\alpha}{2\mathsf{k}} \;=\; \frac{\mathrm{i}\,\alpha\,\mathrm{c}_\infty^2}{2\,\sigma^2}\,. \tag{7.9}$$

The reference solution u is obtained by using relation (7.5). We refer to Subsection 2.5 for the definition of the above Whittaker functions.

7.1.1 First validation problem

The first validation problem consists in imposing Dirichlet boundary conditions on both sides with,

$$\text{Problem (7.13)}\quad \begin{cases} -\,(\,r^2\,u')' \;+\; Q_\ell^{\mathrm{Atmo}}\,u \;=\; 0\,, & r \in [r_{\min},\, r_{\max}]\,,\\ u(r_{\min}) = \tau_0\,, \qquad\qquad u(r_{\max}) = \tau_1\,. \end{cases} \tag{7.10}$$

The corresponding analytic solution for mode ℓ is given by

$$u_{\mathrm{ref}} \;=\; a_\ell\,\frac{\mathrm{W}_{-\chi,\ell+1/2}(-2\mathrm{i}\mathsf{k}\,r)}{r} \;+\; b_\ell\,\frac{\mathrm{W}_{\chi,\ell+1/2}(2\mathrm{i}\mathsf{k}r)}{r}\,, \tag{7.11}$$

where a_ℓ and b_ℓ solve the linear system (see Subsection 5.2)

$$\begin{pmatrix} \dfrac{\mathrm{W}_{-\chi,\ell+1/2}(-2\,\mathrm{i}\,\mathsf{k}\,r_{\min})}{r_{\min}} & \dfrac{\mathrm{W}_{\chi,\ell+1/2}(2\,\mathrm{i}\,\mathsf{k}\,r_{\min})}{r_{\min}}\\[2ex] \dfrac{\mathrm{W}_{-\chi,\ell+1/2}(-2\,\mathrm{i}\,\mathsf{k}\,r_{\max})}{r_{\max}} & \dfrac{\mathrm{W}_{\chi,\ell+1/2}(2\,\mathrm{i}\,\mathsf{k}\,r_{\max})}{r_{\max}} \end{pmatrix} \begin{pmatrix} a_\ell\\ b_\ell \end{pmatrix} \;=\; \begin{pmatrix} \tau_0\\ \tau_1 \end{pmatrix}\,. \tag{7.12}$$

Problem (7.13) is equivalent to first-order problem on $[r_{\min}, r_{\max}]$,

$$\begin{cases} -\,r(r\,v)' \;+\; Q_\ell^{\mathrm{Atmo}}\,w \;=\; r\,g\,,\\ r\,w' \;-\; w \;=\; r\,v\,,\\ w(r_{\min}) \;=\; r_{\min}\,\tau_0 \quad,\quad w(r_{\max}) \;=\; r_{\max}\,\tau_1 \end{cases} \tag{7.13}$$

whose exact solutions are obtained by using the identities (6.2),

$$w_{\text{ref}} \;=\; a_\ell\,\mathrm{W}_{-\chi,\ell+\frac{1}{2}}(-2\mathrm{i}\mathrm{k}\,r) \;+\; b_\ell\,\mathrm{W}_{\chi,\ell+\frac{1}{2}}(2\mathrm{i}\mathrm{k}r)\,; \tag{7.14a}$$

$$v_{\text{ref}} \;=\; -2\,\mathrm{i}\,\mathrm{k}\,a_\ell\,\mathrm{W}'_{-\chi,\ell+\frac{1}{2}}(-2\mathrm{i}\mathrm{k}\,r) \;+\; 2\,\mathrm{i}\,\mathrm{k}\,b_\ell\,\mathrm{W}'_{\chi,\ell+\frac{1}{2}}(2\mathrm{i}\mathrm{k}r) \;-\; \frac{w}{r}\,. \tag{7.14b}$$

We note that the w in the above first order system is also the same w given by relation (7.5). The boundary conditions are obtained via the correspondance in Table 1.

7.1.2 Second validation problem

The second validation problem is given by the boundary condition that treats the singularity at the origin and a Dirichlet condition on the right side, such that,

$$\text{Problem (7.17)}\quad \begin{cases} -\,(\,r^2\,u')' \;+\; Q_\ell^{\text{Atmo}}\,u \;=\; 0\,, & r \;\in\; [0,\,r_{\max}]\,,\\ \lim\limits_{r\to 0} r\,u = 0\,, \qquad\qquad u(r_{\max}) = \tau_1\,. \end{cases} \tag{7.15}$$

Here the exact solution is in terms of the regular Whittaker $\mathcal{M}$ function or of the Buchholtz function M,

$$u_{\text{ref}} \;=\; \tau_1\frac{\mathcal{M}_{\chi,\ell+1/2}(2\mathrm{i}\mathrm{k}r)}{\mathcal{M}_{\chi,\ell+1/2}(2\mathrm{i}\mathrm{k}r_{\max})}\,\frac{r_{\max}}{r} \;=\; \tau_1\frac{\mathrm{M}_{\chi,\ell+1/2}(2\mathrm{i}\mathrm{k}r)}{\mathrm{M}_{\chi,\ell+1/2}(2\mathrm{i}\mathrm{k}r_{\max})}\,\frac{r_{\max}}{r}\,. \tag{7.16}$$

Problem (7.17) is equivalent to the first-order problem on $[0, r_{\max}]$,

$$\boxed{\begin{cases} -\,r(r\,v)' \;+\; Q_\ell^{\text{Atmo}}\,w \;=\; r\,g\,,\\ r\,w' \;-\; w \;=\; r\,v\,,\\ v(0) \;=\; 0 \quad , \quad w(r_{\max}) \;=\; r_{\max}\,\tau_1\,. \end{cases}} \tag{7.17}$$

The exact solutions to (7.17) are

$$w_{\text{ref}} \;=\; \tau_1\,r_{\max}\,\frac{\mathcal{M}_{\chi,\ell+1/2}(2\mathrm{i}\mathrm{k}\,r)}{\mathcal{M}_{\chi,\ell+1/2}(2\mathrm{i}\mathrm{k}\,r_{\max})} \;=\; \tau_1\,r_{\max}\,\frac{\mathrm{M}_{\chi,\ell+1/2}(2\mathrm{i}\mathrm{k}\,r)}{\mathrm{M}_{\chi,\ell+1/2}(2\mathrm{i}\mathrm{k}\,r_{\max})}\,, \tag{7.18a}$$

$$v_{\text{ref}} \;=\; w' \;-\; \frac{w}{r} \tag{7.18b}$$

$$\;=\; \tau_1\,r_{\max}\,2\mathrm{i}\mathrm{k}\,\frac{\mathcal{M}'_{\chi,\ell+1/2}(2\mathrm{i}\mathrm{k}\,r)}{\mathcal{M}_{\chi,\ell+1/2}(2\mathrm{i}\mathrm{k}\,r_{\max})} \;-\; \frac{\tau_1\,r_{\max}}{r}\,\frac{\mathcal{M}_{\chi,\ell+1/2}(2\mathrm{i}\,\mathrm{k}\,r)}{\mathcal{M}_{\chi,\ell+1/2}(2\mathrm{i}\mathrm{k}\,r_{\max})} \tag{7.18c}$$

$$\;=\; \tau_1\,r_{\max}\,2\mathrm{i}\mathrm{k}\,\frac{\mathrm{M}'_{\chi,\ell+1/2}(2\mathrm{i}\mathrm{k}\,r)}{\mathrm{M}_{\chi,\ell+1/2}(2\mathrm{i}\mathrm{k}\,r_{\max})} \;-\; \frac{\tau_1\,r_{\max}}{r}\,\frac{\mathrm{M}_{\chi,\ell+1/2}(2\mathrm{i}\,\mathrm{k}\,r)}{\mathrm{M}_{\chi,\ell+1/2}(2\mathrm{i}\mathrm{k}\,r_{\max})}\,. \tag{7.18d}$$

7.1.3 Third validation problem

Eventually, with $\mathbf{Z}^\ell_{\text{DtN}}$ given in (5.2), we consider the case with the radiation boundary condition with,

$$\text{Problem (7.21)}\quad \begin{cases} \left(-\,\dfrac{d}{dr}\,r^2\,\dfrac{d}{dr} \;+\; Q_\ell^{\text{Atmo}}\right)u \;=\; 0\,, & r \;\in\; [r_{\min},\,r_{\max}]\,,\\ u(r = r_{\min}) = \tau_0\,, \qquad u'(r_{\max}) \;=\; (-1/r_{\max} + \mathbf{Z}^\ell_{\text{DtN}})u(r_{\max})\,. \end{cases} \tag{7.19}$$

The exact solution to (7.19) is given by

$$u_{\text{ref}} \;=\; \tau_0\frac{\mathrm{W}_{-\chi,\ell+1/2}(-2\mathrm{i}\mathrm{k}r)}{\mathrm{W}_{-\chi,\ell+1/2}(-2\mathrm{i}\mathrm{k}r_{\min})}\,\frac{r_{\min}}{r}\,. \tag{7.20}$$

Problem (7.19) is equivalent to the first-order problem (7.21),

$$\boxed{\begin{cases} -\,r(r\,v)' \,+\, Q_\ell^{\text{Atmo}}\, w \,=\, r\,g\,, \\ r\,w' \,-\, w \,=\, r\,v\,, \\ v(r_{\min}) \,=\, r_{\min}\,\tau_0 \quad , \quad v(r_{\max}) \,=\, (-1/r_{\max} + \mathbf{Z}^{\ell}_{\text{DtN}})w(r_{\max}) \end{cases}} \tag{7.21}$$

with analytic solutions,

$$w_{\text{ref}} \;=\; \tau_0\, r_{\min} \frac{\mathrm{W}_{-\chi,\ell+1/2}(-2\mathrm{i}\mathsf{k}\, r)}{\mathrm{W}_{-\chi,\ell+1/2}(-2\mathrm{i}\mathsf{k}\, r_{\min})}\,; \tag{7.22a}$$

$$v_{\text{ref}} \;=\; w' \,-\, \frac{w}{r} \tag{7.22b}$$

$$\;=\; -\tau\, r_{\min} 2\mathrm{i}\mathsf{k}\, \frac{\mathrm{W}'_{-\chi,\ell+1/2}(-2\mathrm{i}\mathsf{k}\, r)}{\mathrm{W}_{-\chi,\ell+1/2}(-2\mathrm{i}\mathsf{k}\, r_{\min})} \;-\; \frac{\tau\, r_{\min}}{r}\, \frac{\mathrm{W}_{-\chi,\ell+1/2}(-2\mathrm{i}\,\mathsf{k}\, r)}{\mathrm{W}_{-\chi,\ell+1/2}(-2\mathrm{i}\mathsf{k}\, r_{\min})}\,. \tag{7.22c}$$

7.2 Numerical validation

We probe our numerical implementation with the three problems introduced above. We select the following constant parameters:

$$\mathfrak{c} = c/R_\odot = 10^{-4}\,\text{s}^{-1}\,, \qquad \alpha = 60\,, \tag{7.23}$$

and investigate the case with attenuation and without ($\gamma = 0$).

Validation problem of type Dirichlet-Dirichlet For Problem (7.13), we consider the interval [0.5, 1], and picture the comparison between the analytic solution and the approximation using the HDG method in Figure 5. In Figure 6, we plot a restriction of the interval for better visualization, and compare the results for different modes. Then, in Figures 7 and 8, we illustrate the case with attenuation, using $\gamma = 10^{-4}$. Visually, we cannot observe any difference between the analytical and computational solutions. To further validate the implementation, we picture the relative error (7.2) for different order of polynomials in Figure 9.

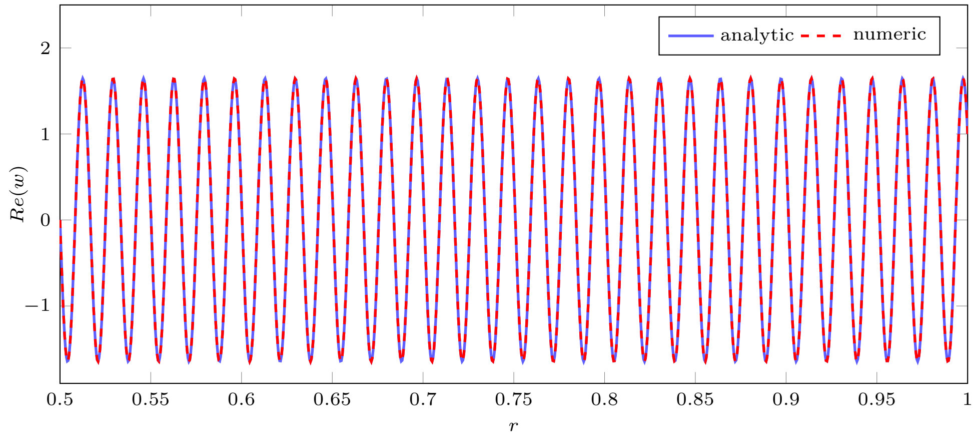

Figure 5: Real parts of the analytic and numerical solution for Problem (7.13) with Dirichlet boundary conditions $\tau_0 = 0$ and $\tau_1 = 1$, for a computational interval $[0.5, 1]$ at frequency 6 mHz for mode $\ell = 0$ without attenuation ($\gamma = 0$). The numerical solution uses polynomials of order 4 and discretization step 10^{-3} (i.e., 501 elements).

We observe the convergence of the method with a relative error that reaches 10^{-6} for sufficiently high order of approximation. The pattern of the convergence is different between w and v such that the convergence of v is faster than in w, but both eventually reach the same precision. Here, we do not observe a difference between the mode 0 and 100 in terms of accuracy.

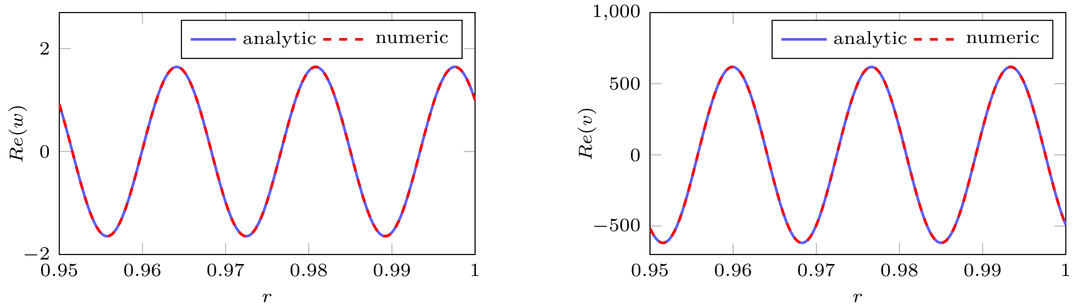

(a) mode $\ell = 0$.

(b) mode $\ell = 0$.

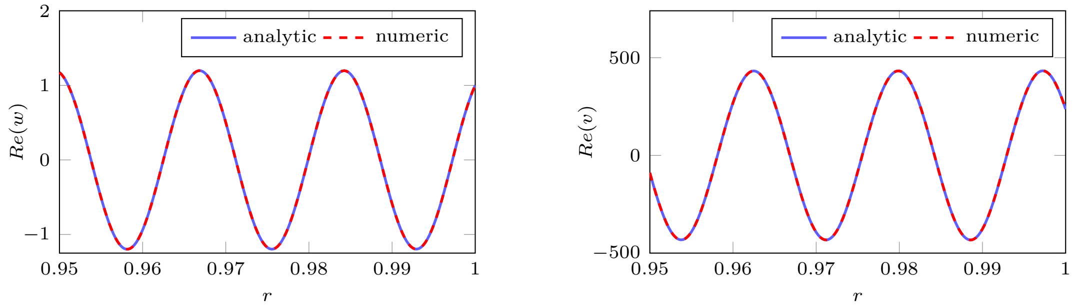

(c) mode $\ell = 100$.

(d) mode $\ell = 100$.

Figure 6: Real parts of the analytic and numerical solution for Problem (7.13) with Dirichlet boundary conditions $\tau_0 = 0$ and $\tau_1 = 1$ at frequency 6 mHz without attenuation ($\gamma = 0$). The original computational interval is $[0.5, 1]$. The numerical solutions use polynomials of order 4 and discretization step 10^{-3} (i.e., 501 elements).

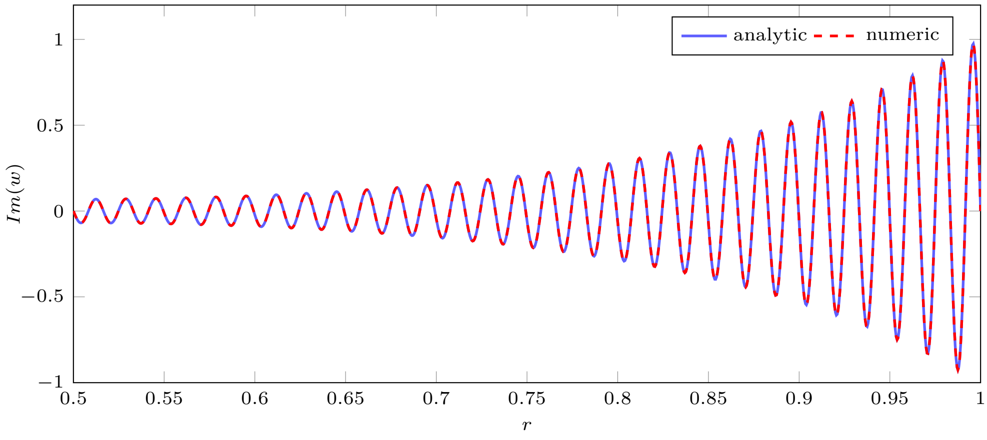

Figure 7: Imaginary parts of the analytic and numerical solution for Problem (7.13) with Dirichlet boundary conditions $\tau_0 = 0$ and $\tau_1 = 1$, for a computational interval [0.5, 1] at frequency 6 mHz for mode $\ell = 0$ with attenuation $\gamma = 10^{-4}$. The numerical solution uses polynomials of order 4 and discretization step 10^{-3} (i.e., 501 elements).

Validation problem of type Neumann-Dirichlet For Problem (7.17), we consider the interval [0, 1] and show the solutions in Figure 10, where we focus on the interval near the origin. The evolution of the relative error with the order of the polynomials is shown in Figure 11.

This test-case allows us to validate the boundary condition at the origin, and we observe similar

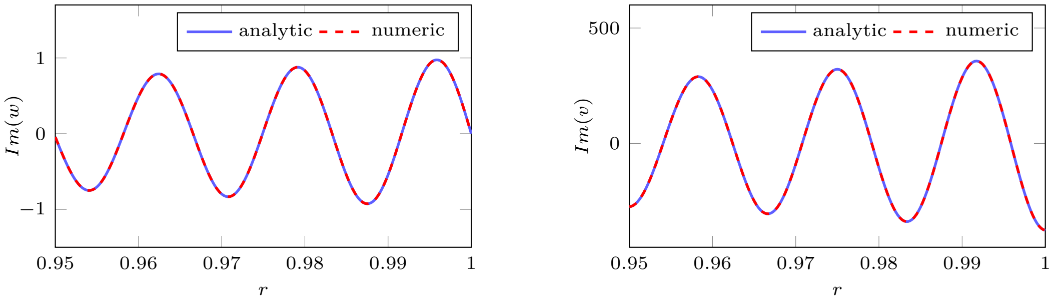

(a) mode $\ell = 0$. (b) mode $\ell = 0$.

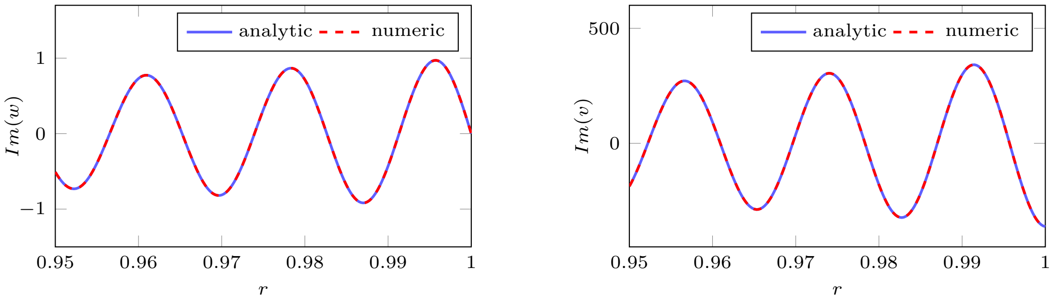

(c) mode $\ell = 100$. (d) mode $\ell = 100$.

Figure 8: Imaginary parts of the analytic and numerical solution for Problem (7.13) with Dirichlet boundary conditions $\tau_0 = 0$ and $\tau_1 = 1$ at frequency 6 mHz with attenuation $\gamma = 100$ µHz. The original computational interval is [0.5, 1]. The numerical solutions use polynomials of order 4 and discretization step 10^{-3} (i.e., 501 elements). The analytic solution w is given by (7.14a).

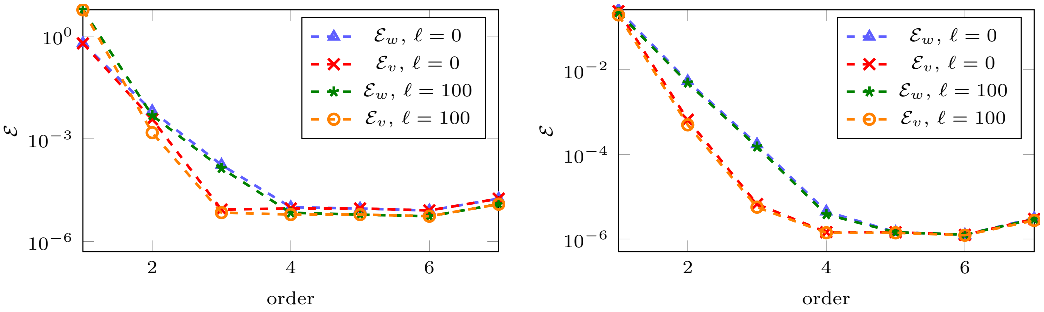

(a) Without attenuation, $\gamma = 0$. (b) With attenuation $\gamma = 10^{-4}$.

Figure 9: Evolution of the relative error (7.2) for Problem (7.13) with Dirichlet boundary conditions $\tau_0 = 0$ and $\tau_1 = 1$ at frequency 6 mHz for a computational interval [0.5, 1]. The numerical solutions use a discretization step 10^{-3} (i.e., 501 elements) and we vary the polynomial order.

accuracy as in the previous case only with Dirichlet boundary conditions, where the relative error given by (7.2) reaches about 10^{-6}.

Validation problem of type Dirichlet - DtN Finally, we validate the HDG implementation in the case of a radiation boundary condition with Problem (7.21). We consider the interval [0.5, 1] and the DtoN condition given (5.2). The analytical and numerical solutions are represented in Figure 12, where we restrict the interval near the radiation boundary. In Figure 13, we provide the evolution of the relative

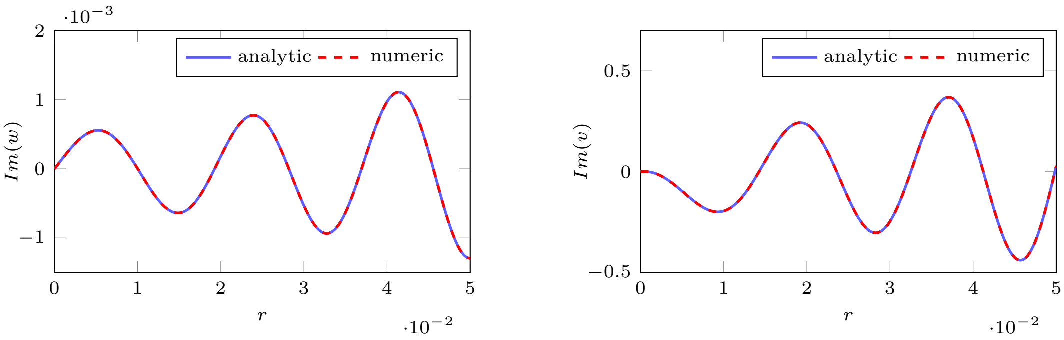

(a) mode $\ell = 0$.

(b) mode $\ell = 0$.

Figure 10: Imaginary parts of the analytic and numerical solution for Problem (7.17) with Dirichlet boundary condition $\tau_1 = 1$ at frequency 6 mHz with attenuation $\gamma = 10^{-4}$. The original computational interval is $[0,\, 1]$. The numerical solutions use polynomials of order 4 and discretization step 10^{-3} (i.e., 1001 elements). The analytic solution w is given by (7.18b).

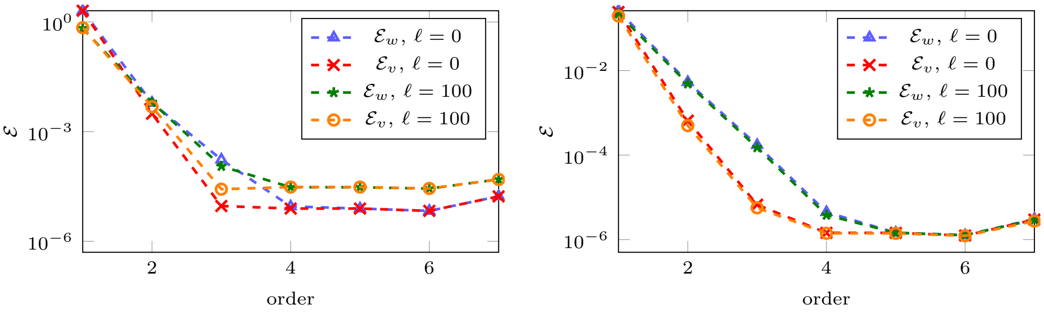

(a) Without attenuation, $\gamma = 0$.

(b) With attenuation $\gamma = 100$ µHz.

Figure 11: Evolution of the relative error (7.2) for Problem (7.17) with Dirichlet boundary condition $\tau_1 = 1$ at frequency 6 mHz for a computational interval $[0,\, 1]$. The numerical solutions use a discretization step 10^{-3} (i.e., 1001 elements) and we vary the polynomial order.

error with the order of the polynomial approximation.

From these three test-cases, we have been able to validate our numerical implementation using the HDG method. The accuracy for Dirichlet, Neumann and radiation boundary conditions is assessed, and we obtain similar accuracy in all cases, with a relative error that reaches 10^{-6}. Both the two variables of the first-order HDG problem have been validated (w and v).

7.3 Validation of point-source problem

We now consider the more interesting configuration of having a delta-Dirac right-hand side at position s, with the radiation boundary condition on the right end and the Neumann-like condition in zero, which amounts to solving the problem,

$$\text{Problem (7.25)} \quad \begin{cases} -\,(r^2\,u')' \;+\; Q_\ell^{\text{Atmo}}\,u \;=\; r\,\delta(r-s)\,, & r \;\in\; [0,\, r_{\max}]\,, \\ \lim\limits_{r\to 0} r\,u = 0\,, \qquad d_r u(r_{\max}) \;=\; (-1/r_{\max} + \mathsf{Z})u(r_{\max})\,. \end{cases} \tag{7.24}$$

As discussed in Subsection 6.1, the above problem is equivalent to

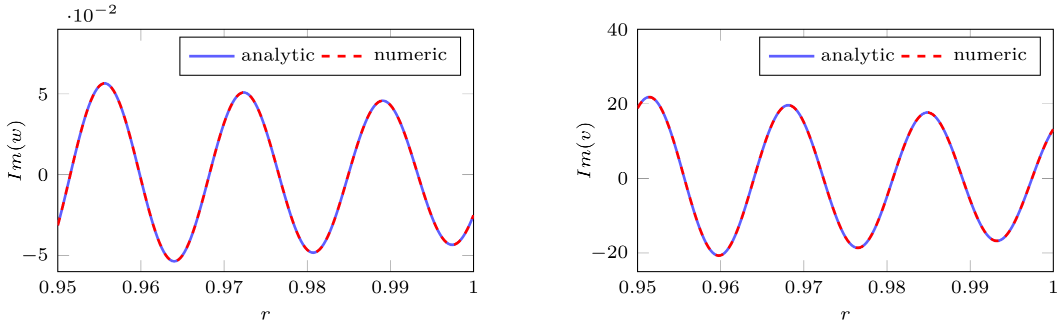

(a) mode $\ell = 0$.   (b) mode $\ell = 0$.

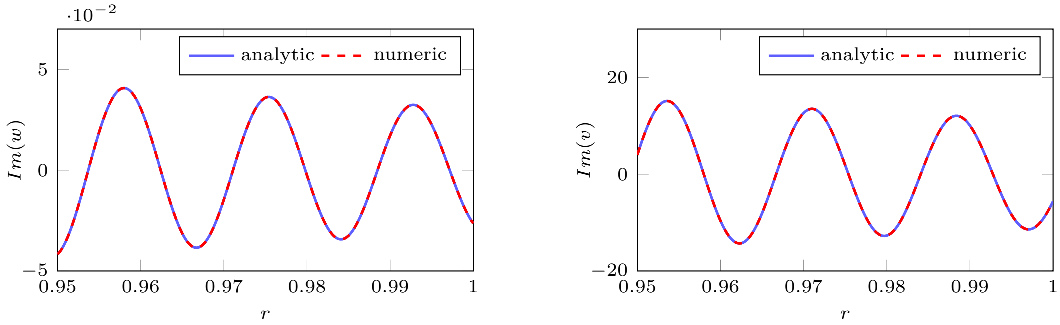

(c) mode $\ell = 100$.   (d) mode $\ell = 100$.

Figure 12: Imaginary parts of the analytic and numerical solution for Problem (7.21) with Dirichlet boundary condition $\tau_0 = 1$ at frequency 6 mHz with attenuation $\gamma = 10^{-4}$. The original computational interval is [0.5, 1]. The numerical solutions use polynomials of order 4 and discretization step 10^{-3} (i.e., 1001 elements). Exact solution w is given by (7.22a).

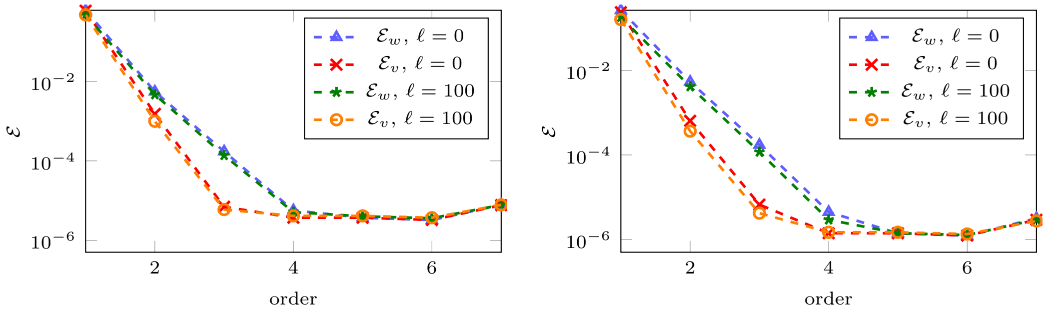

(a) Without attenuation, $\gamma = 0$.   (b) With attenuation $\gamma = 100$ µHz.

Figure 13: Evolution of the relative error (7.2) for Problem (7.21) with Dirichlet boundary condition $\tau_0 = 1$ at frequency 6 mHz for a computational interval [0.5, 1]. The numerical solutions use a discretization step 10^{-3} (i.e., 1001 elements) and we vary the polynomial order.

$$\begin{cases} -\,r(r\,v)' \,+\, Q_\ell^{\text{Atmo}}\,w \;=\; r^2\,\delta(r-s)\,, \\ r\,w' \,-\, w \;=\; r\,v\,, \\ \lim\limits_{r\to 0}\, v \;=\; 0\,, \qquad\qquad v(r_{\max}) \;=\; \Big(-\dfrac{1}{r_{\max}} + \mathsf{Z}\Big)\, w(r_{\max})\,. \end{cases} \tag{7.25}$$

In Subsection 4.2, we have given two ways to compute the solution with either

1. using a direct discretization: this is the Approach 1 of Subsection 4.2.1,
2. assembling the solutions of two boundary value problems, as explained in Proposition 1: this is our Approach 2 (Subsection 4.2.2).

We next give the explicit form for the exact solution w to (7.25).

7.3.1 Analytic solution

The exact solution w to (7.25) is also the solution to

$$\left(-d_r^2 \,-\, \mathsf{k}^2 \,+\, \frac{\alpha_\infty}{r} \,+\, \frac{\ell(\ell+1)}{r^2}\right) w \,=\, \delta(r-s)\,. \tag{7.26}$$

It is thus given by

$$w_{\mathrm{ref}}(r,s) \;=\; \frac{-\mathrm{H}(s-r)\,\psi(r)\,\tilde{\psi}(s) \;-\; \mathrm{H}(r-s)\,\tilde{\psi}(r)\;\psi(s)}{\mathcal{W}\{\psi(s)\,,\,\tilde{\psi}(s)\}}\,, \tag{7.27}$$

where H is the Heavyside function and ψ and $\tilde{\psi}$ are given by

$$\psi = \mathcal{M}_{\chi,\ell+1/2}(2\mathrm{i}\mathsf{k}r) \quad \text{or} \quad \mathrm{M}_{\chi,\ell+1/2}(2\mathrm{i}\mathsf{k}r)\,, \tag{7.28a}$$

$$\tilde{\psi} = \mathrm{W}_{-\chi,\ell+1/2}(-2\mathrm{i}\mathsf{k}r) + a\mathrm{W}_{\chi,\ell+1/2}(2\mathrm{i}\mathsf{k}r)\,. \tag{7.28b}$$

The constant a is determined by the boundary condition at $r = r_{\max}$,

$$\begin{aligned} &2\mathrm{i}\mathsf{k}\big(-\mathrm{W}'_{-\chi,\ell+1/2}(-2\mathrm{i}\mathsf{k}r_{\max}) + a\mathrm{W}'_{\chi,\ell+1/2}(2\mathrm{i}\mathsf{k}r_{\max})\big) \\ &\qquad = (\mathbf{Z}_\bullet)\big(\mathrm{W}_{-\chi,\ell+1/2}(-2\mathrm{i}\mathsf{k}r_{\max}) + a\mathrm{W}_{\chi,\ell+1/2}(2\mathrm{i}\mathsf{k}r_{\max})\big) \end{aligned} \tag{7.29}$$

such that

$$a = \frac{2\mathrm{i}\mathsf{k}\mathrm{W}'_{-\chi,\ell+1/2}(-2\mathrm{i}\mathsf{k}r_{\max}) + (\mathbf{Z}_\bullet)\mathrm{W}_{-\chi,\ell+1/2}(-2\mathrm{i}\mathsf{k}r_{\max})}{2\mathrm{i}\mathsf{k}\mathrm{W}'_{\chi,\ell+1/2}(2\mathrm{i}\mathsf{k}r_{\max}) - (\mathbf{Z}_\bullet)\mathrm{W}_{\chi,\ell+1/2}(2\mathrm{i}\mathsf{k}r_{\max})}\,. \tag{7.30}$$

We note that when $Z = \mathbf{Z}^{\ell}_{\mathrm{DtN}}$ then $a = 0$. We also note that ψ and $\tilde{\psi}$ can be chosen as *constant multiples* of the solutions of the boundary value problems given in (7.17) and (7.21) respectively.

Computation of the Wronskian Here we will give explicit expression for the Wronskian of ψ and $\tilde{\psi}$ given in (7.28).

1. If in (7.28a) we work with $\psi = \mathcal{M}_{\chi,\ell+1/2}(2\mathrm{i}\mathsf{k}r)$, we have that

$$\mathcal{W} = \begin{vmatrix} \mathcal{M}_{\chi,\ell+1/2}(2\mathrm{i}\mathsf{k}r) & \mathrm{W}_{-\chi,\ell+1/2}(-2\mathrm{i}\mathsf{k}r) + a\mathrm{W}_{\chi,\ell+1/2}(2\mathrm{i}\mathsf{k}r) \\ 2\mathrm{i}\mathsf{k}\mathcal{M}'_{\chi,\ell+1/2}(2\mathrm{i}\mathsf{k}r) & 2\mathrm{i}\mathsf{k}(-\mathrm{W}'_{-\chi,\ell+1/2}(-2\mathrm{i}\mathsf{k}r) + a\mathrm{W}'_{\chi,\ell+1/2}(2\mathrm{i}\mathsf{k}r)) \end{vmatrix} \;=\; 2\mathrm{i}\mathsf{k}\,(C_1 + a\,C_2)\,, \tag{7.31}$$

with

$$\begin{aligned} C_1 &= \begin{vmatrix} \mathcal{M}_{\chi,\ell+1/2}(2\mathrm{i}\mathsf{k}r) & \mathrm{W}_{-\chi,\ell+1/2}(-2\mathrm{i}\mathsf{k}r) \\ \mathcal{M}'_{\chi,\ell+1/2}(2\mathrm{i}\mathsf{k}r) & -\mathrm{W}'_{-\chi,\ell+1/2}(-2\mathrm{i}\mathsf{k}r) \end{vmatrix} = \frac{1}{\Gamma(2\ell+2)} \begin{vmatrix} \mathrm{M}_{\chi,\ell+1/2}(2\mathrm{i}\mathsf{k}r) & \mathrm{W}_{-\chi,\ell+1/2}(-2\mathrm{i}\mathsf{k}r) \\ \mathrm{M}'_{\chi,\ell+1/2}(2\mathrm{i}\mathsf{k}r) & -\mathrm{W}'_{-\chi,\ell+1/2}(-2\mathrm{i}\mathsf{k}r) \end{vmatrix} \\ &= \frac{1}{\Gamma(1+\ell+\chi)}(-1)^{\ell+1}\,, \end{aligned} \tag{7.32}$$

and

$$\begin{aligned} C_2 &= \begin{vmatrix} \mathcal{M}_{\chi,\ell+1/2}(2\mathrm{i}\mathsf{k}r) & \mathrm{W}_{\chi,\ell+1/2}(2\mathrm{i}\mathsf{k}r) \\ \mathcal{M}'_{\chi,\ell+1/2}(2\mathrm{i}\mathsf{k}r) & \mathrm{W}'_{\chi,\ell+1/2}(2\mathrm{i}\mathsf{k}r) \end{vmatrix} = \frac{1}{\Gamma(2\ell+2)} \begin{vmatrix} \mathrm{M}_{\chi,\ell+1/2}(2\mathrm{i}\mathsf{k}r) & \mathrm{W}_{\chi,\ell+1/2}(2\mathrm{i}\mathsf{k}r) \\ \mathrm{M}'_{\chi,\ell+1/2}(2\mathrm{i}\mathsf{k}r) & \mathrm{W}'_{\chi,\ell+1/2}(2\mathrm{i}\mathsf{k}r) \end{vmatrix} \\ &= -\frac{1}{\Gamma(\ell+1-\chi)}\,. \end{aligned} \tag{7.33}$$

2. If in (7.28a) we work with $\psi = \mathrm{M}_{\chi,\ell+1/2}(2\mathrm{i}\mathsf{k}r)$, then

$$\mathcal{W}(s) \,=\, 2\mathrm{i}\,\mathsf{k}\,(\tilde{C}_1 \,+\, a\,\tilde{C}_2)\,, \tag{7.34}$$

with

$$\tilde{C}_1 \;=\; \frac{\Gamma(2\ell+2)}{\Gamma(1+\ell+\chi)}(-1)^{\ell+1} \quad , \quad \tilde{C}_2 \;=\; -\frac{\Gamma(2+2\ell)}{\Gamma(\ell+1-\chi)}\,. \tag{7.35}$$

For the above result, we have used [28, 13.14.27] which gives

$$\begin{vmatrix} \mathrm{M}_{\chi,\ell+1/2}(2\mathrm{i}\mathsf{k}r) & \mathrm{W}_{-\chi,\ell+1/2}(-2\mathrm{i}\mathsf{k}r) \\ \mathrm{M}'_{\chi,\ell+1/2}(2\mathrm{i}\mathsf{k}r) & -\mathrm{W}'_{-\chi,\ell+1/2}(-2\mathrm{i}\mathsf{k}r) \end{vmatrix} = \frac{\Gamma(2\ell+2)}{\Gamma(1+\ell+\chi)}e^{(\ell+1)\pi\mathrm{i}} = \frac{\Gamma(2\ell+2)}{\Gamma(1+\ell+\chi)}(-1)^{\ell+1}\,,$$

and [28, 13.14.26],

$$\begin{vmatrix} \mathrm{M}_{\chi,\ell+1/2}(2\mathrm{i}\mathsf{k}r) & \mathrm{W}_{\chi,\ell+1/2}(2\mathrm{i}\mathsf{k}r) \\ \mathrm{M}'_{\chi,\ell+1/2}(2\mathrm{i}\mathsf{k}r) & \mathrm{W}'_{\chi,\ell+1/2}(2\mathrm{i}\mathsf{k}r) \end{vmatrix} = -\frac{\Gamma(2+2\ell)}{\Gamma(\ell+1-\chi)}\,.$$

Exact solution with $\mathbf{Z}^{\ell}_{\mathbf{DtN}}$ As mentioned earlier $a = 0$, the analytical solution (7.27) has the simplified form,

$$w_{\mathrm{ref}}(r,s) \;=\; -\mathrm{H}(s-r)\frac{\mathrm{M}_{\chi,\,\ell+1/2}(2\mathrm{i}\mathsf{k}r)\,\mathrm{W}_{-\chi,\,\ell+1/2}(-2\mathrm{i}\mathsf{k}s)}{2\,\mathrm{i}\,\mathsf{k}\,\frac{\Gamma(2\ell+2)}{\Gamma(1+\ell+\chi)}(-1)^{\ell+1}} \;-\; \mathrm{H}(r-s)\frac{\mathrm{W}_{-\chi,\,\ell+1/2}(-2\mathrm{i}\mathsf{k}r)\,\mathrm{M}_{\chi,\,\ell+1/2}(2\mathrm{i}\mathsf{k}s)}{2\,\mathrm{i}\,\mathsf{k}\,\frac{\Gamma(2\ell+2)}{\Gamma(1+\ell+\chi)}(-1)^{\ell+1}}. \tag{7.36}$$

If the regular solution ψ (7.28a) is obtained with $\mathcal{M}$, we have an equivalent expression for the exact solution,

$$w_{\mathrm{ref}}(r,s) \;=\; -\mathrm{H}(s-r)\frac{\mathcal{M}_{\chi,\,\ell+1/2}(2\mathrm{i}\mathsf{k}r)\,\mathrm{W}_{-\chi,\,\ell+1/2}(-2\mathrm{i}\mathsf{k}s)}{2\,\mathrm{i}\,\mathsf{k}\,\frac{1}{\Gamma(1+\ell+\chi)}(-1)^{\ell+1}} \;-\; \mathrm{H}(r-s)\frac{\mathrm{W}_{-\chi,\,\ell+1/2}(-2\mathrm{i}\mathsf{k}r)\,\mathcal{M}_{\chi,\,\ell+1/2}(2\mathrm{i}\mathsf{k}s)}{2\,\mathrm{i}\,\mathsf{k}\,\frac{1}{\Gamma(1+\ell+\chi)}(-1)^{\ell+1}}\,. \tag{7.37}$$

This simplifies to

$$\begin{aligned} w(r,s) \;=\; \frac{(-1)^{\ell+2}\Gamma(1+\ell+\chi)}{2\mathrm{i}\mathsf{k}}\Big(&\mathrm{H}(s-r)\,\mathcal{M}_{\chi,\,\ell+1/2}(2\mathrm{i}\mathsf{k}r)\,\mathrm{W}_{-\chi,\,\ell+1/2}(-2\mathrm{i}\mathsf{k}s) \\ &+\mathrm{H}(r-s)\,\mathrm{W}_{-\chi,\,\ell+1/2}(-2\mathrm{i}\mathsf{k}r)\mathcal{M}_{\chi,\,\ell+1/2}(2\mathrm{i}\mathsf{k}s)\Big)\,. \end{aligned} \tag{7.38}$$

The specific calculation is written in Subsection 7.3.1.

Remark 5 (Relation to the Helmholtz equation)**.** *When $\alpha = 0$, the first equation of (7.25) reduces to*

$$\left(-\frac{d^2}{dr^2} \,+\, \mathsf{k}^2 \,+\, \frac{\ell(\ell+1)}{r^2}\right) w_\ell(r,s) \;=\; \delta(r-s)\,. \tag{7.39}$$

With zero right-hand-side, the equation

$$\left(-\frac{d^2}{dr^2} \,+\, \mathsf{k}^2 \,+\, \frac{\ell(\ell+1)}{r^2}\right) \mathrm{G} \;=\; 0\,, \tag{7.40}$$

can be rewritten as the spherical Bessel equation

$$\Big(-\frac{d^2}{dz^2} \;-\; \frac{2}{z}\frac{d}{dz} \;-\; 1 \;+\; \frac{\ell(\ell+1)}{z^2}\Big)\mathsf{g} = 0\,. \tag{7.41}$$

By putting back the term r, i.e., for $\mathsf{g}(z) = \frac{\tilde{\mathsf{g}}(z)}{z}$, then $\tilde{\mathsf{g}}(z)$ solves

$$\Big(-\frac{d^2}{dz^2} \;-\; 1 \;+\; \frac{\ell(\ell+1)}{z^2}\Big)\tilde{\mathsf{g}} = 0 \tag{7.42}$$

We now carry out the change of variable $z = \mathsf{k}r$*, thus* $\tilde{\mathrm{g}}(\mathsf{k}r) = \mathrm{G}(r)$ *with* $\mathrm{G}(r)$ *solving (7.39).*

In short, for the solution $\psi(r)$ *on* $[0,b]$ *and outgoing solution* $\tilde{\psi}(r)$ *on* $[a, r_{\max}]$ *to (7.40), we choose*

$$\psi(r) \;=\; r\,\mathrm{j}_\ell(\mathsf{k}\,r)\,, \qquad \tilde{\psi}(r) \;=\; r\,\mathrm{h}^{(1)}_\ell(\mathsf{k}\,r)\,. \tag{7.43}$$

Note that $\mathrm{h}^{(1)}_\ell = \mathrm{j}_\ell + \mathrm{i}\mathrm{y}_\ell$*, using [28, 10.50.1], their Wronskian is given by*

$$\mathrm{W}\{\mathrm{j}_\ell(t)\,,\,\mathrm{h}^{(1)}_\ell(t)\} \;=\; \mathrm{i}\,\mathrm{W}\{\mathrm{j}_\ell(t)\,,\,\mathrm{y}_\ell(t)\} \;=\; \frac{\mathrm{i}}{t^2}\,, \tag{7.44}$$

and

$$\begin{aligned} W\{\psi(r),\tilde{\psi}(r)\} &= \begin{vmatrix} r\mathrm{j}_\ell(\mathsf{k}r) & r\mathrm{h}^{(1)}_\ell(\mathsf{k}r) \\ \mathrm{j}_\ell(\mathsf{k}r) + r\mathsf{k}\mathrm{j}'_\ell(\mathsf{k}r) & \mathrm{h}^{(1)}_\ell(\mathsf{k}r) + \mathsf{k}\,r\,\mathsf{k}\mathrm{h}^{(1)\prime}_\ell(\mathsf{k}r) \end{vmatrix} \\ &= \mathsf{k}r^2 \begin{vmatrix} \mathrm{j}_\ell(\mathsf{k}r) & \mathrm{h}^{(1)}_\ell(\mathsf{k}r) \\ \mathrm{j}'_\ell(\mathsf{k}r) & \mathrm{h}^{(1)\prime}_\ell(\mathsf{k}r) \end{vmatrix} = \mathsf{k}r^2 \frac{\mathrm{i}}{(\mathsf{k}r)^2} = \frac{\mathrm{i}}{\mathsf{k}}\,. \end{aligned} \tag{7.45}$$

Using formula (4.37), the Green function to (7.39) when $\alpha = 0$ *is then*

$$\begin{aligned} w_\ell(r,s) \;&=\; \mathrm{i}\mathsf{k}\,\Big(\mathrm{H}(s-r)\,r\,\mathrm{j}_\ell(\mathsf{k}r)\,s\,\mathrm{h}^{(1)}_\ell(\mathsf{k}s) \;+\; \mathrm{H}(r-s)\,r\,\mathrm{h}^{(1)}_\ell(\mathsf{k}r)\,s\,\mathrm{j}_\ell(\mathsf{k}s)\Big) \\ &=\; \mathrm{i}\mathsf{k}\,r\,s\,\Big(\mathrm{H}(s-r)\,\mathrm{j}_\ell(\mathsf{k}r)\,\mathrm{h}^{(1)}_\ell(\mathsf{k}s) \;+\; \mathrm{H}(r-s)\,\mathrm{h}^{(1)}_\ell(\mathsf{k}r)\,\mathrm{j}_\ell(\mathsf{k}s)\Big)\,. \end{aligned} \tag{7.46}$$

In addition, when $\ell = 0$*,*

$$\mathrm{j}_0 \;=\; \frac{\sin z}{z} \quad , \quad \mathrm{h}^{(1)}_0 = \frac{e^{\mathrm{i}z}}{\mathrm{i}z}\,, \tag{7.47}$$

such that

$$\tilde{\psi}(r) \;=\; r\,\frac{\sin(\mathsf{k}\,r)}{\mathsf{k}r} = \frac{\sin(\mathsf{k}\,r)}{\mathsf{k}}\,, \qquad \psi(r) \;=\; r\,\frac{e^{\mathrm{i}\mathsf{k}r}}{\mathrm{i}\mathsf{k}r} = \frac{e^{\mathrm{i}\mathsf{k}r}}{\mathrm{i}\mathsf{k}}\,, \tag{7.48}$$

and

$$\begin{aligned} w_0(r,s) \;&= \mathrm{i}\mathsf{k}\,r\,s\,\left(\mathrm{H}(s-r)\,\frac{\sin(\mathsf{k}\,r)}{\mathsf{k}\,r}\,\frac{e^{\mathrm{i}\mathsf{k}s}}{\mathrm{i}\,\mathsf{k}\,s} \;+\; \mathrm{H}(r-s)\,\frac{e^{\mathrm{i}\mathsf{k}r}}{\mathrm{i}\,\mathsf{k}\,r}\,\frac{\sin(\mathsf{k}\,s)}{\mathsf{k}\,s}\right) \\ &= \frac{1}{\mathsf{k}}\,\left(\mathrm{H}(s-r)\,\sin(\mathsf{k}\,r)\,e^{\mathrm{i}\mathsf{k}s} \;+\; \mathrm{H}(r-s)\,e^{\mathrm{i}\mathsf{k}r}\,\sin(\mathsf{k}\,s)\right)\,. \end{aligned} \tag{7.49}$$

△

7.3.2 Numerical experiments

We validate our HDG implementation by comparing the numerical solution with the analytical one. The constant parameters are selected to take the value in the solar atmosphere, extracted from the `Atmo` model, which are scaled such that we take

$$\mathfrak{c} = 6.86 \times 10^9/R_\odot = 9.87 \times 10^{-6}\,\mathrm{s}^{-1}\,; \qquad \alpha = 6663.62\,. \tag{7.50}$$

The (scaled) radius varies from 0 to 1.05 and we consider a fixed source in $s = 1$. We investigate different frequencies (6 and 10 mHz), and modes ($\ell = 0$ and $\ell = 100$), as well as the case with or without attenuation, respectively with $\gamma = 0$ and $\gamma = 0.1$. The comparisons between the two approaches and the analytical solution are pictured Figures 14 and 15 where, for the sake of clarity (because of the fast oscillations), we zoom on an interval around the source location. In the case of Approach 2, we take the parameters

$$a \;=\; 10^{-25}\,, \qquad\qquad b \;=\; r_{\max} \;=\; 1.05 \tag{7.51}$$

which give the interval of computation for ψ and $\tilde{\psi}$, see (4.33) and (4.35).

We observe that the two approaches capture well the analytical solution, and we cannot distinguish the difference between them. However, in the Approach 1, which discretizes the delta-Dirac source function on the right-hand side, the singularity remains at the source position, leading to drastic inaccuracy at

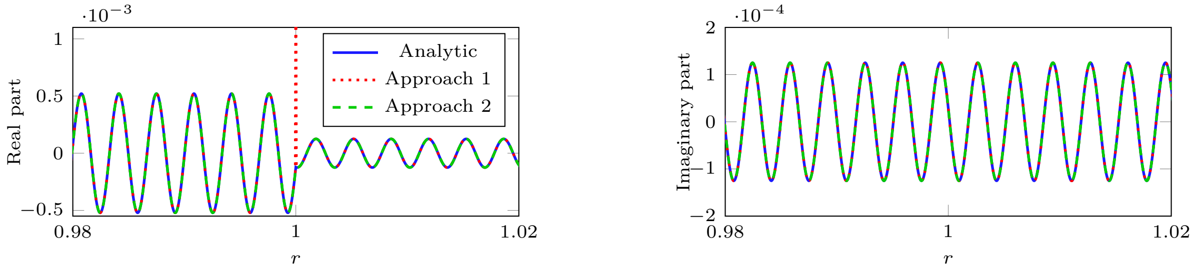

(a) Real part at 6 mHz for $\ell = 0$, $\gamma = 0$.

(b) Imaginary part at 6 mHz for $\ell = 0$, $\gamma = 0$.

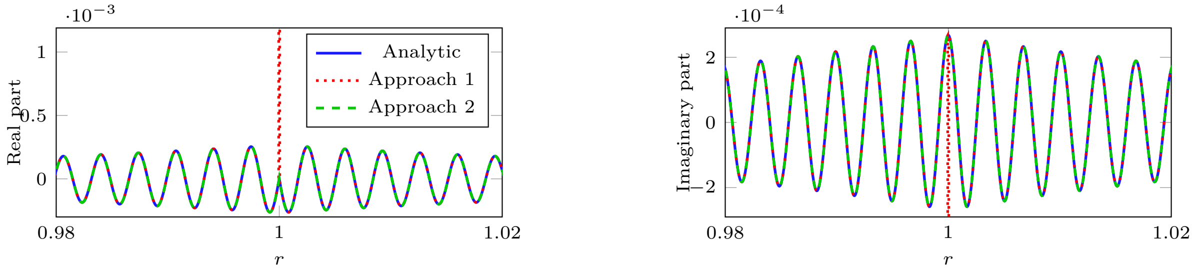

(c) Real part at 6 mHz for $\ell = 0$, $\gamma = 10^{-4}$.

(d) Imaginary part at 6 mHz for $\ell = 0$, $2\pi\gamma = 0.1$mHz.

Figure 14: Comparisons of the solutions at 6 mHz for mode $\ell = 0$ without attenuation ($\gamma = 0$, on top) and with attenuation ($2\pi\gamma = 0.1$mHz, at the bottom) for a source located in $s = 1$.

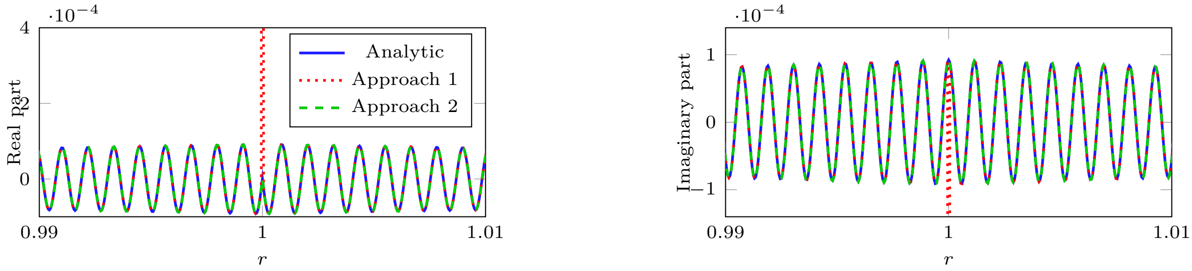

(a) Real part at 10 mHz for $\ell = 0$, $2\pi\gamma = 0.1$mHz.

(b) Imaginary part at 10 mHz for $\ell = 0$, $2\pi\gamma = 0.1$mHz.

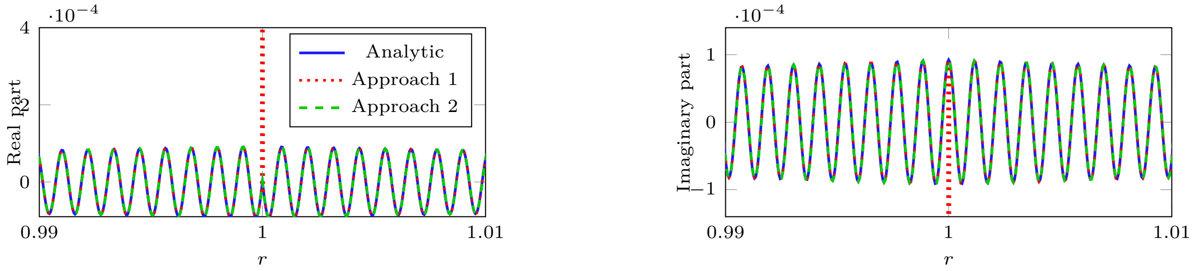

(c) Real part at 10 mHz for $\ell = 100$, $2\pi\gamma = 0.1$mHz.

(d) Imaginary part at 10 mHz for $\ell = 100$, $2\pi\gamma = 0.1$mHz.

Figure 15: Comparisons of the solutions at 10 mHz for mode $\ell = 0$ and $\ell = 100$ with attenuation $2\pi\gamma = 0.1$mHz, for a source located in $s = 1$.

this location. While the singularity is only contained in the real part without attenuation ($\gamma = 0$), when incorporating the attenuation, the singularity (leading to an inaccurate solution) also appears in the imaginary part. This observation highlights a major difficulty of the naive discretization approach: the discretization of the source needs to be carefully addressed. This is even more important as, in helioseismology, one is mostly interested by the value of the solution at the source location (namely, $G_\ell(1,1)$). In order to overcome the issue, one needs to refine around the source position, as advocated in [8, 14, 3]. This can however be cumbersome when several sources must be taken into account, such that the mesh for the numerical resolution must be updated for every source to take into account the refinement, or that one uses the same mesh but which would be over-refined everywhere. On the other hand, Approach 2 provides the accurate solution at the source position, without any need for specific discretization.

In Table 2, we give the relative errors between the approaches, computed on the whole interval (from 0 to $r_{\max}$), using (7.2). For the Approach 1, the relative error excludes the source position, which shows the singularity of the delta-Dirac source. It confirms the accuracy of the numerical solutions, with a relative error that is always less than 0.1%. We also observe that the Approach 2 gives slightly better results.

Table 2: Relative error (7.2) between the analytical solution and the computations using Approach 1 or 2. For Approach 1, due to the singularity of the delta-Dirac function, the solution at the source position is not taken into account in the relative errors. The error is multiplied by 100 to give the result in percent.

3 mHz		**Approach 1**	**Approach 2**
	$\ell = 0 \quad, \gamma = 0$	$2.4 \times 10^{-2}\%$	$6.9 \times 10^{-3}\%$
	$\ell = 100, \gamma = 0$	$1.8 \times 10^{-2}\%$	$6.6 \times 10^{-3}\%$
	$\ell = 0 \quad, \gamma = 10^{-4}$	$1.8 \times 10^{-4}\%$	$5.5 \times 10^{-5}\%$
	$\ell = 100, \gamma = 10^{-4}$	$1.8 \times 10^{-4}\%$	$5.5 \times 10^{-5}\%$

10 mHz		**Approach 1**	**Approach 2**
	$\ell = 0 \quad, \gamma = 0$	$2.1 \times 10^{-2}\%$	$9.9 \times 10^{-3}\%$
	$\ell = 100, \gamma = 0$	$2.2 \times 10^{-2}\%$	$9.4 \times 10^{-3}\%$
	$\ell = 0 \quad, \gamma = 10^{-4}$	$6.3 \times 10^{-3}\%$	$8.3 \times 10^{-3}\%$
	$\ell = 100, \gamma = 10^{-4}$	$6.3 \times 10^{-3}\%$	$8.3 \times 10^{-3}\%$

8 Observables in local helioseismology

In helioseismology, the data are time series representing the surface oscillations $\Phi(\hat{\boldsymbol{r}}_1, t_j)$ at spatial points $\hat{\boldsymbol{r}}_1$ on the CCD (charge-coupled device) camera and at times t_j. The data can come from satellites such as MDI (Michelson doppler imager) on board of the SOHO (solar and heliospheric observatory) satellite (from 1996 to 2010) [31] or the HMI (helioseismic and magnetic imager) on board of the SDO (solar dynamics observatory) satellite since 2010 [32] but also from ground-based telescopes such as the GONG (global oscillation network group) network (since 1996) [18].

The temporal resolution h_t is of one minute for MDI and GONG, and of 45 s for HMI. This resolution determines the Nyquist frequency – the highest frequency that can be observed – $\omega_{\max}/(2\pi) = 1/(2h_t)$ ($\sim$ 11.1 mHz for HMI and 8.33 mHz for MDI and GONG). The spatial resolution is linked to the number of pixels of the instrument which is of 4000 by 4000 for HMI (4k×4k) 1000 by 1000 for MDI (1k×1k). GONG had initially a 256 × 256 camera which was replaced by a 1k × 1k camera in 2001. One pixel is around 0.03 heliographic degrees for HMI and 0.12 heliographic degrees for MDI and the actual data from GONG (which has a spatial step of 1.45 Mm at the disk center).

In this section, we define some classic quantities used in local helioseismology such as the cross-covariance function, the power spectrum and the wave travel times. These quantities will be used in Section 9 to compare the different boundary conditions and to show the importance of the knowledge of the full Green kernel.

8.1 Classical helioseismic quantities

8.1.1 Observables

In order to analyse the data, a relationship between the observed wavefield Φ and the modeled wave displacement $\boldsymbol{\xi}$ is necessary. It can be written formally as

$$\Phi(\hat{\boldsymbol{r}}_1, t_j) = \mathcal{O}_{\hat{\boldsymbol{r}}_1}\Big(\boldsymbol{\xi}(\boldsymbol{r}, t_j)\Big), \tag{8.1}$$

where $\hat{\boldsymbol{r}}_1$ is a point on the camera, t_j is the time and $\mathcal{O}$ is an operator that depends on the point $\hat{\boldsymbol{r}}_1$ and on the wave displacement at any location $\boldsymbol{r}$ in the solar interior. The data are then generally Fourier transform to the frequency domain

$$\Phi(\hat{\boldsymbol{r}}_1, \omega_k) = \frac{h_t}{2\pi} \sum_{j=-N_t/2}^{N_t/2-1} \Phi(\hat{\boldsymbol{r}}_1, t_j) e^{i\omega_k t_j}, \tag{8.2}$$

where T is the observation time, $N_t = T/dt$ the number of data samples during the time T, and $t_j = jdt$ is the discrete time variable. The inverse Fourier transform is defined as

$$\Phi(\hat{\boldsymbol{r}}_1, t_j) = h_\omega \sum_{k=-N_t/2}^{N_t/2-1} \Phi(\hat{\boldsymbol{r}}_1, \omega_k) e^{-i\omega_k t_j}, \tag{8.3}$$

where $h_\omega = 2\pi/T$ is the frequency spacing, and $\omega_k = kh_\omega$. We suppose that the observable operator $\mathcal{O}$ does not depend on time and we can thus write equivalently (8.1) in the frequency domain

$$\Phi(\hat{\boldsymbol{r}}_1, \omega_k) = \mathcal{O}_{\hat{\boldsymbol{r}}_1}\Big(\boldsymbol{\xi}(\boldsymbol{r}, \omega_k)\Big). \tag{8.4}$$

Remark 6. *An example of such operator often used to interpret Dopplergrams [7] [6] is an approximation of the line-of-sight velocity such that*

$$\mathcal{O}_{\hat{\boldsymbol{r}}_1}\Big(\boldsymbol{\xi}(\boldsymbol{r}, \omega_k)\Big) = -\mathrm{i}\omega_\mathrm{k} \hat{\mathbf{l}}(\hat{\boldsymbol{r}}_1) \cdot \boldsymbol{\xi}(\boldsymbol{r}_1, \omega_\mathrm{k}), \tag{8.5}$$

where $\hat{\mathbf{l}}(\hat{\boldsymbol{r}}_1)$ is the line-of-sight unit vector corresponding to the observation point $\hat{\boldsymbol{r}}_1$ and $\boldsymbol{r}_1 = (1, \hat{\boldsymbol{r}}_1)$ is the 3D point at the solar surface. It requires the knowledge of the 3D displacement and cannot be obtained directly in the framework of this report.

8.1.2 Filtering

To analyze the data, the observable is generally decomposed into spherical harmonics such that

$$\Phi(\hat{\boldsymbol{r}}_1, \omega_k) = \sum_{l=0}^{L_{\max}} \sum_{m=-l}^{l} \Phi_l^m(\omega_k) \mathrm{Y}_l^m(\theta_1, \phi_1), \tag{8.6}$$

where

$$\Phi_l^m(\omega_k) = \int_0^{2\pi} \int_0^{\pi} \Phi(\theta, \phi, \omega_k) \overline{\mathrm{Y}_l^m(\theta, \phi)} \sin\theta d\theta d\phi. \tag{8.7}$$

Of course, θ and ϕ are only available on a discrete grid and the integral needs to be replaced by a sum at available locations. Similarly to the Nyquist frequency for ω, the largest available harmonic degree $L_{\max}$ is $\pi/h_\theta = N_\theta$ where $h_\theta = \pi/N_\theta$ is the number of available pixels. Thus, due to the number of pixels on the camera, $L_{\max} = 1000$ for MDI and 4000 for HMI.

Depending on the considered problem the data are then filtered in order to be more sensitive to the desired quantity. The filtered observable $\tilde{\Phi}_l^m(\omega_k)$ is obtained by multiplying by a filter F

$$\tilde{\Phi}_\ell^m(\omega_k) = \Phi_\ell^m(\omega_k) \mathsf{F}_\ell^m(\omega_k), \tag{8.8}$$

where $\mathsf{F}_l^m(\omega_k)$ is the spherical harmonic coefficient of the filter $\mathsf{F}(\omega_k)$. In this report, we use a phase-speed filter

$$\mathsf{F}_\ell^m(\omega_k) = \exp\left(-\frac{(|\omega_k|R_\odot/\ell - v_i)^2}{2\delta v_i^2}\right), \tag{8.9}$$

where v_i is the mean velocity and δv_i the standard deviation. Other classical filters can be used for example to select a range of harmonic degrees between L_0 and L_1

$$\mathsf{F}_\ell^m(\omega_k) = \delta_{[L_0,L_1]}, \tag{8.10}$$

or similarly a range of frequencies $[\omega_0, \omega_1]$. The δ can be replaced by a smoother filter (Gaussian, smooth rectangle) in order to avoid edge effects (aliasing).

The filtered data can then be transformed back to spatial variables

$$\tilde{\Phi}(\hat{\boldsymbol{r}}_1, \omega_k) = \sum_{\ell=0}^{L_{\max}} \sum_{m=-\ell}^{\ell} \tilde{\Phi}_\ell^m(\omega_k) Y_\ell^m(\theta_1, \phi_1). \tag{8.11}$$

Assumption 4. *We suppose that the filter does not depend on longitude (and thus not on the azimuthal order m) and is the same at all spatial locations on the camera (for all points $\hat{\boldsymbol{r}}$ on the solar surface).*

8.1.3 Cross-covariance and power spectrum

As the sources due to convection have zero mean, the expectation value of the observable $\mathbb{E}[\Phi(\hat{\boldsymbol{r}}_1, \omega_k)]$ is equal to zero and thus the data cannot be analyzed directly on the observed signal. Thus, one generally considers the cross-covariance between any two points at the solar surface. In the frequency domain it just corresponds to a multiplication and

$$C(\hat{\boldsymbol{r}}_1, \hat{\boldsymbol{r}}_2, \omega_k) = \overline{\tilde{\Phi}(\hat{\boldsymbol{r}}_1, \omega_k)} \tilde{\Phi}(\hat{\boldsymbol{r}}_2, \omega_k). \tag{8.12}$$

The expectation value of the cross-covariance is denoted by

$$\mathcal{C}(\hat{\boldsymbol{r}}_1, \hat{\boldsymbol{r}}_2, \omega_k) = \mathbb{E}[\overline{\tilde{\Phi}(\hat{\boldsymbol{r}}_1, \omega_k)} \tilde{\Phi}(\hat{\boldsymbol{r}}_2, \omega_k)]. \tag{8.13}$$

To facilitate the derivation of $\mathcal{C}$ in Subsection 8.2.3, we also define the expectation value of the cross-covariance for unfiltered data

$$\mathcal{C}^{\mathrm{u}}(\hat{\boldsymbol{r}}_1, \hat{\boldsymbol{r}}_2, \omega_k) = \mathbb{E}[\overline{\Phi(\hat{\boldsymbol{r}}_1, \omega_k)} \Phi(\hat{\boldsymbol{r}}_2, \omega_k)]. \tag{8.14}$$

The power spectrum is

$$\begin{aligned} \mathcal{P}^{\ell,m}(\omega_k) &= \mathbb{E}[|\tilde{\Phi}_l^m(\omega_k)|^2] \\ &= \int_0^{2\pi}\int_0^{\pi}\int_0^{2\pi}\int_0^{\pi} \mathcal{C}(\hat{\boldsymbol{r}}_1, \hat{\boldsymbol{r}}_2, \omega_k) \mathrm{Y}_l^m(\theta_1, \phi_1) \overline{\mathrm{Y}_l^m(\theta_2, \phi_2)} \sin\theta_1 d\theta_1 d\phi_1 \sin\theta_2 d\theta_2 d\phi_2. \end{aligned} \tag{8.15}$$

It corresponds to the spherical harmonic transform (in $\hat{\boldsymbol{r}}_1$ and $\hat{\boldsymbol{r}}_2$ of the expectation value of the cross-covariance.

8.1.4 Travel-time and amplitude measurements

In time-distance helioseismology, the travel-time (τ) and amplitude ($\mathfrak{a}$) between the observed and a reference cross-covariance are often used. They are defined as the solution of the minimization problem ,

$$\int_{-\infty}^{\infty} w(t) \left[\mathcal{C}(\hat{\boldsymbol{r}}_1, \hat{\boldsymbol{r}}_2, t) - \mathfrak{a}\mathcal{C}^{\mathrm{ref}}(\hat{\boldsymbol{r}}_1, \hat{\boldsymbol{r}}_2, t-\tau)\right]^2 dt, \tag{8.16}$$

where w is a window function chosen in order to select a given wave packet (for example the first arrival wave packet, see e.g. Fig. 1 in [26] for a sketch). The reference cross-covariance $\mathcal{C}^{\mathrm{ref}}$ can be obtained

	Ass. Source	Surface	Integrated	Depth
Observable		$\Phi_{\mathrm{surf}}(\hat{\boldsymbol{r}}_1, \omega_k) =$ $\psi(R_\odot, \hat{\boldsymbol{r}}_1, \omega_k)$	$\Phi_{\mathrm{int}}(\hat{\boldsymbol{r}}_1, \omega_k) =$ $\int K(r, \hat{\boldsymbol{r}}_1)\psi(r, \hat{\boldsymbol{r}}_1, \omega_k)dr$	$\Phi_{\mathrm{depth}}(\hat{\boldsymbol{r}}_1, \omega_k) =$ $\psi(r_{\mathrm{fh}}(\hat{\boldsymbol{r}}_1), \hat{\boldsymbol{r}}_1, \omega_k)$
Cross-covariance	(8.36)	(8.39)$^{(*)}$	(8.41)$^{(*)}$	(8.42)$^{(*)}$
	(8.37)	(8.46)	(8.47)	(8.48)
	(8.38)	(8.51)	(8.52)	(8.53)
Power spectrum	(8.37)	(8.56)	(8.61)	(8.64)
	(8.38)	(8.65)	(8.66)	(8.68)

Table 3: Summary of the three defined observables and the corresponding equations to compute the expectation value of the cross-covariance and the power spectrum depending on the hypothesis on the source covariance matrix. The unknown ψ is solution the wave equation given by (8.21).
$^{(*)}$ These expressions are for the unfiltered data.

by averaging the observations or computed from a reference solar model. Linearizing around reference values such that $\tau = \tau_0 + \delta\tau$ and $\mathfrak{a} = 1 + \delta\mathfrak{a}$, the solution of the minimization problem at first order is, cf. [26, Equation 6 and 7]

$$\delta\tau(\hat{\boldsymbol{r}}_1, \hat{\boldsymbol{r}}_2) = \int_{-\infty}^{\infty} W_\tau(\hat{\boldsymbol{r}}_1, \hat{\boldsymbol{r}}_2, t) \left(\mathcal{C}(\hat{\boldsymbol{r}}_1, \hat{\boldsymbol{r}}_2, t) - \mathcal{C}^{\mathrm{ref}}(\hat{\boldsymbol{r}}_1, \hat{\boldsymbol{r}}_2, t)\right) dt, \tag{8.17}$$

$$\delta\mathfrak{a}(\hat{\boldsymbol{r}}_1, \hat{\boldsymbol{r}}_2) = \int_{-\infty}^{\infty} W_{\mathfrak{a}}(\hat{\boldsymbol{r}}_1, \hat{\boldsymbol{r}}_2, t) \left(\mathcal{C}(\hat{\boldsymbol{r}}_1, \hat{\boldsymbol{r}}_2, t) - \mathcal{C}^{\mathrm{ref}}(\hat{\boldsymbol{r}}_1, \hat{\boldsymbol{r}}_2, t)\right) dt \tag{8.18}$$

where the weighting functions W_τ and $W_{\mathfrak{a}}$ are given by, cf. [26, Equation 8 and 9],

$$W_\tau(\hat{\boldsymbol{r}}_1, \hat{\boldsymbol{r}}_2, t) = -\frac{w(t)\partial_t \mathcal{C}^{\mathrm{ref}}(\hat{\boldsymbol{r}}_1, \hat{\boldsymbol{r}}_2, t)}{\int_{-\infty}^{\infty} w(t')\partial_t \mathcal{C}^{\mathrm{ref}}(\hat{\boldsymbol{r}}_1, \hat{\boldsymbol{r}}_2, t')^2 dt'}, \tag{8.19}$$

$$W_{\mathfrak{a}}(\hat{\boldsymbol{r}}_1, \hat{\boldsymbol{r}}_2, t) = \frac{w(t)\mathcal{C}^{\mathrm{ref}}(\hat{\boldsymbol{r}}_1, \hat{\boldsymbol{r}}_2, t)}{\int_{-\infty}^{\infty} w(t')\mathcal{C}^{\mathrm{ref}}(\hat{\boldsymbol{r}}_1, \hat{\boldsymbol{r}}_2, t')^2 dt'}. \tag{8.20}$$

8.2 From the scalar wave solution to simulated observables

In order to consider a scalar problem instead of solving for the full 3D wave displacement $\boldsymbol{\xi}$, we follow the approach of [15] and solve an equation for the quantity $\psi = \rho c^2 \nabla \cdot \boldsymbol{\xi}$ which is (up to the minus sign) the Lagrangian perturbation of the pressure. It satisfies

$$\mathcal{L}\psi := -\nabla \cdot \left(\frac{1}{\rho}\nabla\psi\right) - \frac{\sigma^2}{\rho c^2}\psi = \mathfrak{s}, \tag{8.21}$$

where $\mathfrak{s}(\boldsymbol{r}, \omega_k)$ is a stochastic source that represents the excitation of waves due to convection. It is a random process with zero mean and covariance matrix $M(\boldsymbol{r}, \boldsymbol{r}', \omega_k)$.

We consider three different possible observables $\Phi(\hat{\boldsymbol{r}}_1, \omega_k)$ (and their associated filtered version $\tilde{\Phi}(\hat{\boldsymbol{r}}_1, \omega_k)$) for this scalar problem:

- the observable at the surface which is classically used for helioseismic studies. In this case, the operator $\mathcal{O}$ is given by

  $$\mathcal{O}_{\hat{\boldsymbol{r}}_1}\left(\boldsymbol{\xi}(\boldsymbol{r}, \omega_k)\right) = \rho(\boldsymbol{r}_1)c^2(\boldsymbol{r}_1)\nabla \cdot \boldsymbol{\xi}(\boldsymbol{r}_1, \omega_k), \tag{8.22}$$

  where $\boldsymbol{r}_1 = (1, \hat{\boldsymbol{r}}_1)$, and the observable $\Phi_{\mathrm{surf}}(\hat{\boldsymbol{r}}_1, \omega_k)$ is directly the solution of (8.21) at the solar surface

  $$\Phi_{\mathrm{surf}}(\hat{\boldsymbol{r}}_1, \omega_k) = \psi(\boldsymbol{r}_1, \omega_k). \tag{8.23}$$

  It supposes that the Sun is a solid body with a clearly defined surface at height 1 corresponding to the solar radius in unscaled quantities.

- the observable integrated over depth. As the Sun is a plasma, the observables cannot be considered to come only from the solar surface but correspond to a weighted average

  $$\Phi_{\text{int}}(\hat{\boldsymbol{r}}_1, \omega_k) = \int K(r, \hat{\boldsymbol{r}}_1)\psi(r, \hat{\boldsymbol{r}}_1, \omega_k)dr, \tag{8.24}$$

  where K is called the contribution function[6]. In our numerical experiments, we use an approximation and consider that K is roughly a Gaussian that peaks at a given depth $r_{\text{fh}}(\hat{\boldsymbol{r}}_1)$

  $$K(r, \hat{\boldsymbol{r}}_1) = \frac{1}{\sqrt{2\pi}\,\sigma} \exp\left(-\frac{(r - r_{\text{fh}}(\hat{\boldsymbol{r}}_1))^2}{2\sigma^2}\right), \tag{8.25}$$

  where $\sigma\ R_\odot = 50$ km and

  $$r_{\text{fh}}(\hat{\boldsymbol{r}}_1) = r_{\text{eq}} + (r_{\text{pole}} - r_{\text{eq}}) \cos^2(\theta_1) \cos^2(\phi_1), \tag{8.26}$$

  with $r_{\text{eq}}\ R_\odot = 0$ km, and $r_{\text{pole}}\ R_\odot = 300$ km. With this simplified formula the observed height at the equator is r_{eq} while it is r_{pole} at the pole. The integral must theoretically be done over the full depth range but it can in practice be done only from a few hundred kilometers below the surface as deeper layers inside the Sun are optically thick.

- the observable at a given height. To avoid the integration from (8.24), it is possible simplify the previous approach and to define a formation height[7]

  $$r_{\text{fh}}(\hat{\boldsymbol{r}}_1) = \text{argmax}_r\ K(r, \hat{\boldsymbol{r}}_1). \tag{8.27}$$

  We then define a third possible observable which corresponds to the solution of the wave equation at the formation height $r_{\text{fh}}(\hat{\boldsymbol{r}}_1)$

  $$\Phi_{\text{depth}}(\hat{\boldsymbol{r}}_1, \omega_k) = \psi(r_{\text{fh}}(\hat{\boldsymbol{r}}_1), \hat{\boldsymbol{r}}_1, \omega_k). \tag{8.28}$$

In the next subsections, we derive the expressions to compute these observables as well as the expectation value of the cross-covariance and the power spectrum as a function of the Green's function Legendre coefficients. A summary of the results is given in Table 3.

Remark 7. *Integrating the observable over height (and thus the full Green kernel) is also required if we define our observable as a perturbation to the emergent intensity due to acoustic oscillations. In this case, the background emergent intensity is defined in an equilibrium state (perfect sphere of radius $R_\odot$ with background sound speed c_0 and density ρ_0). The oscillations perturb the solar surface and the thermodynamical quantities and thus the observed intensity. For adiabatic oscillations, the Lagrangian perturbations of density, pressure and temperature are linked to the divergence of the displacement and thus to the unknown of our scalar equation ψ. We could then define the function $\tilde{K}$ such that, at first order,*

$$\delta I(\hat{\boldsymbol{r}}_1, \omega_k) = \int \tilde{K}(r, \hat{\boldsymbol{r}}_1)\psi(r, \hat{\boldsymbol{r}}_1, \omega_k)dr. \tag{8.29}$$

Example of intensity perturbations computed with such an approach can be found in [36].

---

[6] The contribution function expresses how much of the observable is coming from the depth r at the position $\hat{\boldsymbol{r}}_1$. It depends on the opacity which is a function of pressure, temperature and chemical composition of the Sun. An example of contribution function can be seen in [22, e.g. Fig. 1] and the expression of the contribution function corresponds to the term inside the integral in [22, Eq. 3].

[7] The formation height is the height from which most of the photons are emitted and which thus contributes the most to the observable. It is increasing towards the limb which implies that the observable is coming from a height with lower density and temperature at the limb compare to the disk center. The emitted intensity is thus decreasing with latitude which makes the limb appears darker than the center of the Sun, an optical phenomenon called limb darkening.

8.2.1 Connection to the Green kernel

The solution of (8.21) can be obtained from the Green's function of the linear operator $\mathcal{L}$

$$\psi(\boldsymbol{r}_1, \omega_k) = \int \mathcal{G}(\boldsymbol{r}_1, \boldsymbol{r}, \omega_k)\mathfrak{s}(\boldsymbol{r}, \omega_k) d\boldsymbol{r}. \tag{8.30}$$

For a radially symmetric background, the Green's function can be written as a function of the Legendre coefficients $\mathcal{G}_\ell$ solutions of (1.5) (see Proposition 1)

$$\mathcal{G}(\boldsymbol{r}_1, \boldsymbol{r}, \omega_k) = \frac{1}{4\pi r_1 r} \sum_\ell (2\ell+1) \mathcal{G}_\ell(r_1, r, \omega_k) \mathrm{P}_\ell(\cos\theta_{\hat{\boldsymbol{r}}_1 \cdot \hat{\boldsymbol{r}}}). \tag{8.31}$$

Thus, the three possible observables can be obtained from the solution of the modal ODE as

$$\Phi_{\mathrm{surf}}(\hat{\boldsymbol{r}}_1, \omega_k) = \frac{1}{4\pi} \sum_\ell (2\ell+1) \int \frac{\mathcal{G}_\ell(1, r, \omega_k)}{r} \mathrm{P}_\ell(\cos\theta_{\hat{\boldsymbol{r}}_1 \cdot \hat{\boldsymbol{r}}})\, \mathfrak{s}(\boldsymbol{r}, \omega_k) d\boldsymbol{r}, \tag{8.32}$$

$$\Phi_{\mathrm{int}}(\hat{\boldsymbol{r}}_1, \omega_k) = \frac{1}{4\pi} \sum_\ell (2\ell+1) \int K(r', \hat{\boldsymbol{r}}_1) \int \frac{\mathcal{G}_\ell(r', r, \omega_k)}{r r'} \mathrm{P}_\ell(\cos\theta_{\hat{\boldsymbol{r}}_1 \cdot \hat{\boldsymbol{r}}})\, \mathfrak{s}(\boldsymbol{r}, \omega_k) d\boldsymbol{r} dr', \tag{8.33}$$

$$\Phi_{\mathrm{depth}}(\hat{\boldsymbol{r}}_1, \omega_k) = \frac{1}{4\pi r_{\mathrm{fh}}(\hat{\boldsymbol{r}}_1)} \sum_\ell (2\ell+1) \int \frac{\mathcal{G}_\ell(r_{\mathrm{fh}}(\hat{\boldsymbol{r}}_1), r, \omega_k)}{r} \mathrm{P}_\ell(\cos\theta_{\hat{\boldsymbol{r}}_1 \cdot \hat{\boldsymbol{r}}})\, \mathfrak{s}(\boldsymbol{r}, \omega_k) d\boldsymbol{r}. \tag{8.34}$$

Note that due to seismic reciprocity we have $\mathcal{G}(\boldsymbol{r}_1, \boldsymbol{r}, \omega_k) = \mathcal{G}(\boldsymbol{r}, \boldsymbol{r}_1, \omega_k)$ and $\mathcal{G}_l(r_1, r, \omega_k) = \mathcal{G}_l(r, r_1, \omega_k)$. Thus the Green's function and consequently the observable Φ_{surf} can be obtained from the computation of a single Green's function (at all harmonic degrees l) with a source located at the solar surface, while Φ_{int} requires the full Green's function for all sources and receivers (in the support of K) and Φ_{depth} needs the Green's function at all heights r_1 corresponding to the observation points $\hat{\boldsymbol{r}}_1$.

8.2.2 Assumptions on the sources of excitation

To obtain the $\Phi(\hat{\boldsymbol{r}}_1, \omega_k)$ one needs to generate a realization of the random process $\mathfrak{s}$. This source term corresponds to the stochastic excitation of the wave by convection.

Assumption 5. *The source term is a Gaussian process with zero-mean and source covariance matrix M*

$$\mathbb{E}[\overline{s(\boldsymbol{r}, \omega_k)} s(\boldsymbol{r}', \omega_k)] := M(\boldsymbol{r}, \boldsymbol{r}', \omega_k). \tag{8.35}$$

Assumption 6. *The sources satisfy Assumption 5 and are spatially uncorrelated*

$$\mathbb{E}[\overline{s(\boldsymbol{r}, \omega_k)} s(\boldsymbol{r}', \omega_k)] = M(\boldsymbol{r}, \boldsymbol{r}, \omega_k)\delta(\boldsymbol{r} - \boldsymbol{r}'). \tag{8.36}$$

While Assumption 5 can be justified by the law of larger number, Assumption 6 should be taken with care as the sources have a horizontal correlation length depending on the scales we are interested in (e.g $\sim 1-2$ Mm for granulation, ~ 30 Mm for supergranulation, see e.g. [17]) and an unknown vertical correlation length. An example of source covariance matrix with a correlation length in time and space is given in [16], although they considered uncorrelated sources for their numerical examples as it greatly simplifies the computations.

As little is known about the source covariance matrix M, simple forms are often assumed in order to reduce the computational cost.

Assumption 7. *The sources satisfy Assumption 6 with a covariance matrix M that depends only on depth*

$$M(\boldsymbol{r}, \boldsymbol{r}, \omega_k) = \mathfrak{M}(r, \omega_k). \tag{8.37}$$

This is the most commonly used simplification and includes for example the choice from [6, 24] where $M(\boldsymbol{r}, \boldsymbol{r}, \omega_k) = \delta(r - r_s)$, where r_s is the height where the sources are generated.

A more physical assumption coming from the geophysics litterature [33, 12] is that the energy is equipartitioned. It was introduced in helioseismology in [15].

Assumption 8. *The sources satisfy Assumption 6 with a covariance matrix M and the energy is equipartitioned which implies for our problem that [15]*

$$M(\boldsymbol{r},\boldsymbol{r},\omega_k) = \Pi(\omega_k)\left(\frac{\gamma(r)}{\rho(r)} + \frac{c(r)}{2\rho(r)}\delta(r-1)\right), \tag{8.38}$$

where Π is a function that describes the time correlations of the sources.

8.2.3 Expectation value of the cross-covariance as a function of the Green function

In this subsection, we give the expressions of the expectation value of the cross-covariance as a function of the Green kernel under the different assumptions on the source covariance matrix. We suppose that at least Assumption 6 (spatially uncorrelated sources) is satisfied.

Unfiltered data Using the definition of the observables Φ_{surf}, Φ_{int} and Φ_{depth} given by (8.23), (8.24) and (8.28), the expectation value of the cross-covariance for unfiltered data is given by

$$\mathcal{C}^{\mathrm{u}}_{\mathrm{surf}}(\hat{\boldsymbol{r}}_1,\hat{\boldsymbol{r}}_2,\omega_k) := \mathbb{E}[\overline{\Phi_{\mathrm{surf}}(\hat{\boldsymbol{r}}_1,\omega_k)}\Phi_{\mathrm{surf}}(\hat{\boldsymbol{r}}_2,\omega_k)] = \int \overline{\mathcal{G}(1,\hat{\boldsymbol{r}}_1,\boldsymbol{r},\omega_k)}\mathcal{G}(1,\hat{\boldsymbol{r}}_2,\boldsymbol{r},\omega_k)\mathfrak{M}(\boldsymbol{r})d\boldsymbol{r}, \tag{8.39}$$

$$\mathcal{C}^{\mathrm{u}}_{\mathrm{int}}(\hat{\boldsymbol{r}}_1,\hat{\boldsymbol{r}}_2,\omega_k) := \mathbb{E}[\overline{\Phi_{\mathrm{int}}(\hat{\boldsymbol{r}}_1,\omega_k)}\Phi_{\mathrm{int}}(\hat{\boldsymbol{r}}_2,\omega_k)] \tag{8.40}$$

$$= \int\int\int K(r',\hat{\boldsymbol{r}}_1)K(r'',\hat{\boldsymbol{r}}_2)\overline{\mathcal{G}(r',\hat{\boldsymbol{r}}_1,\boldsymbol{r},\omega_k)}\mathcal{G}(r'',\hat{\boldsymbol{r}}_2,\boldsymbol{r},\omega_k)\mathfrak{M}(\boldsymbol{r})d\boldsymbol{r}dr'dr'', \tag{8.41}$$

$$\mathcal{C}^{\mathrm{u}}_{\mathrm{depth}}(\hat{\boldsymbol{r}}_1,\hat{\boldsymbol{r}}_2,\omega_k) := \mathbb{E}[\overline{\Phi_{\mathrm{depth}}(\hat{\boldsymbol{r}}_1,\omega_k)}\Phi_{\mathrm{depth}}(\hat{\boldsymbol{r}}_2,\omega_k)] = \int \overline{\mathcal{G}(r_{\mathrm{fh}}(\hat{\boldsymbol{r}}_1),\hat{\boldsymbol{r}}_1,\boldsymbol{r},\omega_k)}\mathcal{G}(r_{\mathrm{fh}}(\hat{\boldsymbol{r}}_2),\hat{\boldsymbol{r}}_2,\boldsymbol{r},\omega_k)\mathfrak{M}(\boldsymbol{r})d\boldsymbol{r}. \tag{8.42}$$

Without any additional on the source covariance, the expressions for the expectation value of the filtered cross-covariance are lengthy and not instructive. We will thus derive these expressions only in the case of Assumptions 7 and 8.

Under Assumption 7, using the representation of the 3D Green function from Proposition 1 and the result (2.13), one obtains

$$\mathcal{C}^{\mathrm{u}}_{\mathrm{surf}}(\hat{\boldsymbol{r}}_1,\hat{\boldsymbol{r}}_2,\omega_k) = \sum_{\ell}\frac{2\ell+1}{4\pi}\mathrm{P}_\ell(\cos\theta_{\hat{\boldsymbol{r}}_1\cdot\hat{\boldsymbol{r}}_2})\int|\mathcal{G}_\ell(1,r,\omega_k)|^2\mathfrak{M}(r,\omega_k)dr, \tag{8.43}$$

$$\mathcal{C}^{\mathrm{u}}_{\mathrm{int}}(\hat{\boldsymbol{r}}_1,\hat{\boldsymbol{r}}_2,\omega_k) = \sum_{\ell}\frac{2\ell+1}{4\pi}\mathrm{P}_\ell(\cos\theta_{\hat{\boldsymbol{r}}_1\cdot\hat{\boldsymbol{r}}_2})\int\int\int K(r',\hat{\boldsymbol{r}}_1)K(r'',\hat{\boldsymbol{r}}_2)\frac{\overline{\mathcal{G}_\ell(r',r,\omega_k)}\mathcal{G}_\ell(r'',r,\omega_k)}{r'r''}\mathfrak{M}(r,\omega_k)drdr'dr'', \tag{8.44}$$

$$\mathcal{C}^{\mathrm{u}}_{\mathrm{depth}}(\hat{\boldsymbol{r}}_1,\hat{\boldsymbol{r}}_2,\omega_k) = \frac{1}{r_{\mathrm{fh}}(\hat{\boldsymbol{r}}_1)r_{\mathrm{fh}}(\hat{\boldsymbol{r}}_2)}\sum_{\ell}\frac{2\ell+1}{4\pi}\mathrm{P}_\ell(\cos\theta_{\hat{\boldsymbol{r}}_1\cdot\hat{\boldsymbol{r}}_2})\int\overline{\mathcal{G}_\ell(r_{\mathrm{fh}}(\hat{\boldsymbol{r}}_1),r,\omega_k)}\mathcal{G}_\ell(r_{\mathrm{fh}}(\hat{\boldsymbol{r}}_2),r,\omega_k)\mathfrak{M}(r,\omega_k)dr. \tag{8.45}$$

Filtered data Under Assumption 7, it is now also possible to write the expression of the expectation value of the cross-covariance for filtered data. Projecting $\tilde{\Phi}$ into spherical harmonics and using the definition of the filtered data (8.8), we obtain similar expressions than above but now with the filter

$$\mathcal{C}_{\mathrm{surf}}(\hat{\boldsymbol{r}}_1,\hat{\boldsymbol{r}}_2,\omega_k)=\sum_\ell \frac{2\ell+1}{4\pi}\mathsf{F}_\ell^2\mathrm{P}_\ell(\cos\theta_{\hat{\boldsymbol{r}}_1\cdot\hat{\boldsymbol{r}}_2})\int|\mathcal{G}_\ell(1,r,\omega_k)|^2\mathfrak{M}(r,\omega_k)dr, \tag{8.46}$$

$$\mathcal{C}_{\mathrm{int}}(\hat{\boldsymbol{r}}_1,\hat{\boldsymbol{r}}_2,\omega_k)=$$
$$\sum_\ell \frac{2\ell+1}{4\pi}\mathsf{F}_\ell^2\mathrm{P}_\ell(\cos\theta_{\hat{\boldsymbol{r}}_1\cdot\hat{\boldsymbol{r}}_2})\int\int\int K(r',\hat{\boldsymbol{r}}_1)K(r'',\hat{\boldsymbol{r}}_2)\frac{\overline{\mathcal{G}_\ell(r',r,\omega_k)}\mathcal{G}_\ell(r'',r,\omega_k)}{r'r''}\mathfrak{M}(r,\omega_k)drdr'dr'', \tag{8.47}$$

$$\mathcal{C}_{\mathrm{depth}}(\hat{\boldsymbol{r}}_1,\hat{\boldsymbol{r}}_2,\omega_k)=$$
$$\frac{1}{r_{\mathrm{fh}}(\hat{\boldsymbol{r}}_1)r_{\mathrm{fh}}(\hat{\boldsymbol{r}}_2)}\sum_\ell \frac{2\ell+1}{4\pi}\mathsf{F}_\ell^2\mathrm{P}_\ell(\cos\theta_{\hat{\boldsymbol{r}}_1\cdot\hat{\boldsymbol{r}}_2})\int\overline{\mathcal{G}_\ell(r_{\mathrm{fh}}(\hat{\boldsymbol{r}}_1),r,\omega_k)}\mathcal{G}_\ell(r_{\mathrm{fh}}(\hat{\boldsymbol{r}}_2),r,\omega_k)\mathfrak{M}(r,\omega_k)dr. \tag{8.48}$$

Here, we used again the addition theorem and the orthonormality of spherical harmonics.

If moreover we have Assumption 8, then it was shown in [15] that

$$\int\overline{\mathcal{G}(\boldsymbol{r}_1,\boldsymbol{r},\omega_k)}\mathcal{G}(\boldsymbol{r}_2,\boldsymbol{r},\omega_k)\mathfrak{M}(\boldsymbol{r},\omega_k)d\boldsymbol{r}=\frac{\Pi(\omega_k)}{2\omega_k}\mathrm{Im}[\mathcal{G}(\boldsymbol{r}_1,\boldsymbol{r}_2,\omega_\mathrm{k})], \tag{8.49}$$

$$=\frac{1}{4\pi r_1r_2}\frac{\Pi(\omega_k)}{2\omega_k}\sum_\ell(2\ell+1)\mathrm{Im}[\mathcal{G}_\mathrm{l}(\mathrm{r}_1,\mathrm{r}_2,\omega_\mathrm{k})]\mathrm{P}_\ell(\cos\theta_{\hat{\boldsymbol{r}}_1\cdot\hat{\boldsymbol{r}}_2}). \tag{8.50}$$

For the last equality, we use Proposition 1. In this case, the expressions for the expectation value of the cross-covariance become

$$\mathcal{C}_{\mathrm{surf}}(\hat{\boldsymbol{r}}_1,\hat{\boldsymbol{r}}_2,\omega_k)=\frac{\Pi(\omega_k)}{8\pi\omega_k}\sum_\ell(2\ell+1)\mathsf{F}_\ell^2\mathrm{Im}[\mathcal{G}_\mathrm{l}(1,1,\omega_\mathrm{k})]\mathrm{P}_\ell(\cos\theta_{\hat{\boldsymbol{r}}_1\cdot\hat{\boldsymbol{r}}_2}), \tag{8.51}$$

$$\mathcal{C}_{\mathrm{int}}(\hat{\boldsymbol{r}}_1,\hat{\boldsymbol{r}}_2,\omega_k)=\frac{\Pi(\omega_k)}{8\pi\omega_k}\sum_\ell(2\ell+1)\mathsf{F}_\ell^2\int\int K(r,\hat{\boldsymbol{r}}_1)K(r',\hat{\boldsymbol{r}}_2)\frac{\mathrm{Im}[\mathcal{G}_\mathrm{l}(\mathrm{r},\mathrm{r}',\omega_\mathrm{k})]}{rr'}drdr'P_\ell(\cos\theta_{\hat{\boldsymbol{r}}_1\cdot\hat{\boldsymbol{r}}_2}), \tag{8.52}$$

$$\mathcal{C}_{\mathrm{depth}}(\hat{\boldsymbol{r}}_1,\hat{\boldsymbol{r}}_2,\omega_k)=\frac{\Pi(\omega_k)}{8\pi\omega_k}\frac{1}{r_{\mathrm{fh}}(\hat{\boldsymbol{r}}_1)r_{\mathrm{fh}}(\hat{\boldsymbol{r}}_2)}\sum_\ell(2\ell+1)\mathsf{F}_\ell^2\mathrm{Im}[\mathcal{G}_\mathrm{l}(\mathrm{r}_{\mathrm{fh}}(\hat{\boldsymbol{r}}_2),\mathrm{r}_{\mathrm{fh}}(\hat{\boldsymbol{r}}_1),\omega_\mathrm{k})]\mathrm{P}_\ell(\cos\theta_{\hat{\boldsymbol{r}}_1\cdot\hat{\boldsymbol{r}}_2}). \tag{8.53}$$

Remark 8. *For a radially symmetric medium, under the hypotheses (8.37) or (8.38), the expectation value of the cross-covariance for surface observations depends only on the angle between the observation points $\hat{\boldsymbol{r}}_1$ and $\hat{\boldsymbol{r}}_2$ (see (8.46) and (8.51)). In this case, we simply write $\mathcal{C}_{\mathrm{surf}}(\theta,\omega)$.* △

To evaluate $\mathcal{C}_{\mathrm{surf}}$, one only needs to evaluate the Green's function for a source at the surface while a source at a given height (that differs depending on co-latitude and longitude) is required for $\mathcal{C}_{\mathrm{depth}}$ and the full Green function for $\mathcal{C}_{\mathrm{int}}$. Thanks to the approach 2 to compute the Green function proposed in this report, the computation time required to compute $\mathcal{C}_{\mathrm{int}}$ or $\mathcal{C}_{\mathrm{depth}}$ is only twice as much as the one to compute $\mathcal{C}_{\mathrm{surf}}$ using the approach 1 (as two simulations are required for the approach 2 but the full Green function is obtained while approach 1 requires one simulation but gives only the Green function for one source location).

Note that the number of Green functions to be computed is independent of the hypothesis on the source covariance matrix. However the computational cost to evaluate the expectation of the cross-covariance is larger if one only supposes that the sources are uncorrelated as an extra integral over depth must be performed (see e.g (8.39) compared to (8.46) and (8.51)).

Time-distance diagram The inverse Fourier transform in time of the expectation value of the cross-covariance $\mathcal{C}(\hat{\boldsymbol{r}}_1,\hat{\boldsymbol{r}}_2,t)$ is called the time-distance diagram and allows for a visual representation of how waves propagating through the solar interior are observed at the surface as a function of time and distance (see e.g. Fig. 12 in [15]). In order to compute the time-distance diagram, the Green function must be computed for all harmonic degrees ℓ and frequencies ω_k in order to be able to perform the Legendre and inverse Fourier transform. It is thus important to have an efficient method to compute the full Green function as this routine should be called many times. It is however embarrassingly parallel as the frequencies and harmonic degrees are independent.

8.2.4 Power spectrum as a function of the modal Green function

If the only assumption is that the sources are spatially uncorrelated, then the expressions of the power spectrum are obtained by plugging (8.39), (8.42), and (8.41) into the definition of the power spectrum (8.15) and cannot be further simplified.

If we assume also (8.37) then the horizontal integrals can be done analytically using the orthonormality of spherical harmonics (2.26) and we obtain for the case of surface data

$$\begin{aligned}
\mathcal{P}^{\ell,m}_{\text{surf}}(\omega_k) &= \int_0^{2\pi}\int_0^{\pi}\int_0^{2\pi}\int_0^{\pi} \mathcal{C}_{\text{surf}}(\hat{\boldsymbol{r}}_1,\hat{\boldsymbol{r}}_2,\omega_k)\mathrm{Y}_l^m(\theta_1,\phi_1)\overline{\mathrm{Y}_l^m(\theta_2,\phi_2)}\sin\theta_1 d\theta_1 d\phi_1 \sin\theta_2 d\theta_2 d\phi_2, && (8.54)\\
&= \sum_{\ell'} \frac{2\ell'+1}{4\pi}\mathsf{F}^2_{\ell'}\int |\overline{\mathcal{G}_{\ell'}(1,r,\omega_k)}|^2 \mathfrak{M}(r,\omega_k)dr \\
&\quad \int_0^{2\pi}\int_0^{\pi}\int_0^{2\pi}\int_0^{\pi} \mathrm{P}_{\ell'}(\cos\theta_{\hat{\boldsymbol{r}}_1\cdot\hat{\boldsymbol{r}}_2})\mathrm{Y}_\ell^m(\theta_1,\phi_1)\overline{\mathrm{Y}_\ell^m(\theta_2,\phi_2)}\sin\theta_1 d\theta_1 d\phi_1 \sin\theta_2 d\theta_2 d\phi_2, && (8.55)\\
&= \mathsf{F}^2_\ell \int |\mathcal{G}_\ell(1,r,\omega_k)|^2\mathfrak{M}(r,\omega_k)dr, && (8.56)
\end{aligned}$$

where we used the addition theorem (2.27).

In the case of integrated data, the power spectrum is given by

$$\begin{aligned}
\mathcal{P}^{\ell,m}_{\text{int}}(\omega_k) &= \int_0^{2\pi}\int_0^{\pi}\int_0^{2\pi}\int_0^{\pi} \mathcal{C}_{\text{int}}(\hat{\boldsymbol{r}}_1,\hat{\boldsymbol{r}}_2,\omega_k)\mathrm{Y}_l^m(\theta_1,\phi_1)\overline{\mathrm{Y}_l^m(\theta_2,\phi_2)}\sin\theta_1 d\theta_1 d\phi_1 \sin\theta_2 d\theta_2 d\phi_2, && (8.57)\\
&= \sum_{\ell'} \frac{2\ell'+1}{4\pi}\mathsf{F}^2_{\ell'} \int_0^{2\pi}\int_0^{\pi}\int_0^{2\pi}\int_0^{\pi} \mathrm{P}_{\ell'}(\cos\theta_{\hat{\boldsymbol{r}}_1\cdot\hat{\boldsymbol{r}}_2})\mathrm{Y}_l^m(\theta_1,\phi_1)\overline{\mathrm{Y}_l^m(\theta_2,\phi_2)} && (8.58)\\
&\quad \int\int\int K(r',\hat{\boldsymbol{r}}_1)K(r'',\hat{\boldsymbol{r}}_2)\sin\theta_1 d\theta_1 d\phi_1 \sin\theta_2 d\theta_2 d\phi_2 \frac{\overline{\mathcal{G}_{\ell'}(r',r,\omega_k)}\mathcal{G}_{\ell'}(r'',r,\omega_k)}{r'r''}\mathfrak{M}(r,\omega_k)dr dr' dr''. && (8.59)
\end{aligned}$$

The main difference with $\mathcal{P}_{\text{surf}}$ is that the functions K depend on $\hat{\boldsymbol{r}}_1$ and $\hat{\boldsymbol{r}}_2$ and the horizontal integrals cannot be evaluated as easily as before. One solution is to evaluate these integrals numerically, however it can become cumbersome for high harmonic degrees. It is also possible to decompose K into spherical harmonics

$$K(r',\hat{\boldsymbol{r}}_1) = \sum_{\ell_1}\sum_{m_1=-\ell_1}^{\ell_1} K^{\ell_1,m_1}(r')\mathrm{Y}_{\ell_1}^{m_1}, \tag{8.60}$$

and to use the Gaunt formula (2.30) in order to compute analytically the integral of the product of three spherical harmonics, to obtain,

$$\begin{aligned}
\mathcal{P}^{\ell,m}_{\text{int}}(\omega_k) = \sum_{\ell'} F^2_{\ell'} \sum_{\ell_1=|\ell-\ell'|}^{\ell+\ell'}\sum_{\ell_2=|\ell-\ell'|}^{\ell+\ell'}\sum_{m'=-L}^{L} &\operatorname{Gaunt}(\ell,\ell',\ell_1,m,-m',-m+m') \\
\operatorname{Gaunt}(\ell,\ell',\ell_2,m,m',-m-m') &\int \frac{K^{\ell_1,-m+m'}(r')}{r'}\int\frac{K^{\ell_2,-m-m'}(r'')}{r''} \\
&\int \overline{\mathcal{G}_{\ell'}(r',r,\omega_k)}\mathcal{G}_{\ell'}(r'',r,\omega_k)\mathfrak{M}(r,\omega_k)dr dr' dr''. \qquad (8.61)
\end{aligned}$$

Here $L = \min(\ell',\ell_1,\ell_2)$ and we have use the fact that the Gaunt integrals are non-zeros only if the sum of the three m is equal to 0.

For data whose formation height is varying, the power spectrum is given by

$$\mathcal{P}^{\ell,m}_{\text{depth}}(\omega_k) = \int_0^{2\pi}\int_0^{\pi}\int_0^{2\pi}\int_0^{\pi} \mathcal{C}_{\text{depth}}(\hat{\boldsymbol{r}}_1,\hat{\boldsymbol{r}}_2,\omega_k)\mathrm{Y}_l^m(\theta_1,\phi_1)\overline{\mathrm{Y}_l^m(\theta_2,\phi_2)}\sin\theta_1 d\theta_1 d\phi_1 \sin\theta_2 d\theta_2 d\phi_2, \quad (8.62)$$

$$= \sum_{\ell'} \frac{2\ell'+1}{4\pi}\mathsf{F}^2_{\ell'} \int_0^{2\pi}\int_0^{\pi}\int_0^{2\pi}\int_0^{\pi} \mathrm{P}_{\ell'}(\cos\theta_{\hat{\boldsymbol{r}}_1\cdot\hat{\boldsymbol{r}}_2})\mathrm{Y}_l^m(\theta_1,\phi_1)\overline{\mathrm{Y}_l^m(\theta_2,\phi_2)} \quad (8.63)$$

$$\int \frac{\overline{\mathcal{G}_{\ell'}(r_{\text{fh}}(\hat{\boldsymbol{r}}_1),r,\omega_k)}\mathcal{G}_{\ell'}(r_{\text{fh}}(\hat{\boldsymbol{r}}_2),r,\omega_k)}{r_{\text{fh}}(\hat{\boldsymbol{r}}_1)r_{\text{fh}}(\hat{\boldsymbol{r}}_2)}\mathfrak{M}(r,\omega_k)dr \;\; \sin\theta_1 d\theta_1 d\phi_1 \sin\theta_2 d\theta_2 d\phi_2. \quad (8.64)$$

It is possible to write that $r_{\text{fh}}(\hat{\boldsymbol{r}}_1) = \int \delta(r' - r_{\text{fh}}(\hat{\boldsymbol{r}}_1))dr'$ and to project the Dirac delta function into spherical harmonics in order to evaluate analytically the horizontal integrals as previously. However, the convergence of the Dirac delta function into spherical harmonics is very slow and many coefficients would need to be kept. It is thus more efficient to evaluate numerically these integrals.

With energy equipartition (8.38), the expressions of the power spectrum further simplify

$$\mathcal{P}^{\ell,m}_{\text{surf}}(\omega_k) = \frac{\Pi(\omega_k)}{2\omega_k}\mathsf{F}^2_\ell \mathrm{Im}[\mathcal{G}_\ell(1,1,\omega_\mathrm{k})], \quad (8.65)$$

$$\mathcal{P}^{\ell,m}_{\text{int}}(\omega_k) = \frac{\Pi(\omega_k)}{2\omega_k}\sum_{\ell'} F^2_{\ell'} \sum_{\ell_1=|\ell-\ell'|}^{\ell+\ell'} \sum_{\ell_2=|\ell-\ell'|}^{\ell+\ell'} \sum_{m'=-L}^{L} \mathrm{Gaunt}(\ell,\ell',\ell_1,m,-m',-m+m')$$

$$\mathrm{Gaunt}(\ell,\ell',\ell_2,m,m',-m-m') \int \frac{K^{\ell_1,-m+m'}(r')}{r'} \int \frac{K^{\ell_2,-m-m'}(r'')}{r''} \mathrm{Im}\left[\mathcal{G}_{\ell'}(\mathrm{r}',\mathrm{r}'',\omega_\mathrm{k})\right]\mathrm{dr}'\mathrm{dr}'', \quad (8.66)$$

$$\mathcal{P}^{\ell,m}_{\text{depth}}(\omega_k) = \frac{\Pi(\omega_k)}{2\omega_k}\sum_{\ell'} \frac{2\ell'+1}{4\pi}\mathsf{F}^2_{\ell'} \int_0^{2\pi}\int_0^{\pi}\int_0^{2\pi}\int_0^{\pi} \mathrm{P}_{\ell'}(\cos\theta_{\hat{\boldsymbol{r}}_1\cdot\hat{\boldsymbol{r}}_2})\mathrm{Y}_l^m(\theta_1,\phi_1)\overline{\mathrm{Y}_l^m(\theta_2,\phi_2)} \quad (8.67)$$

$$\frac{\mathrm{Im}\left[\mathcal{G}_{\ell'}(\mathrm{r}_{\text{fh}}(\hat{\boldsymbol{r}}_1),\mathrm{r}_{\text{fh}}(\hat{\boldsymbol{r}}_2,\omega_\mathrm{k})\right]}{r_{\text{fh}}(\hat{\boldsymbol{r}}_1)r_{\text{fh}}(\hat{\boldsymbol{r}}_2)} \;\sin\theta_1 d\theta_1 d\phi_1 \sin\theta_2 d\theta_2 d\phi_2. \quad (8.68)$$

With observations at the surface, the power spectrum (at a given ℓ and ω_k) is proportional to the imaginary part of the Green function Legendre coefficient $\mathcal{G}_\ell$ with a source and receiver at the surface. With integrated data, the knowledge of the full Green function for all sources and receivers is still required.

Remark 9. *For surface data, under hypothesis (8.37) and (8.38), the expectation value of the cross-covariance depends only on the angle between* $\hat{\boldsymbol{r}}_1$ *and* $\hat{\boldsymbol{r}}_2$ *and the expression of the power spectrum simplifies to*

$$\mathcal{P}^{\ell,m}_{\text{surf}}(\omega_k) = \frac{2\ell+1}{2}\int_0^{\pi} \mathcal{C}_{\text{surf}}(\theta,\omega_k)\mathrm{P}_\ell(\cos\theta)\sin\theta d\theta. \quad (8.69)$$

In this case, the power spectrum is then independent of m *and corresponds to the Legendre transform of the expectation value of the cross-covariance* $\mathcal{C}$.

9 Numerical experiments with solar models

Now that our HDG implementation has been validated from the analytical solution, we perform numerical experiments using inhomogeneous medium parameters that follow the solar profiles. Our code is written in `Fortran90`, and combine `mpi` and `OpenMp` parallelism[8]. Furthermore, our code is linked with the library `Arb`, [19] for the efficient computation of the special functions.

9.1 Model parameters from `S+Atmo` and `S+Val-C`

The propagation of the scalar waves is governed by the medium wave speed c and the inverse density scale height α, together with its derivative α'. In the interior of the Sun, these are extracted from the model

---

[8] The code used, `Haven` will soon be made available online and will be open-source.

`S` of [9]. In the atmosphere, we consider two models: `Atmo`, where the velocity is smoothly extended to a constant and the density follows an exponential decay ([14, 15]); and the model `Val-C`, [34]. Consequently, we designed the two solar profiles, `S+Atmo` and `S+Val-C`, which we picture in Figure 16. In particular, we see that the atmospheric profile given by the model `Val-C` contains a drastic increase of both parameters c and α, while the profile of the `Atmo` models is smooth.

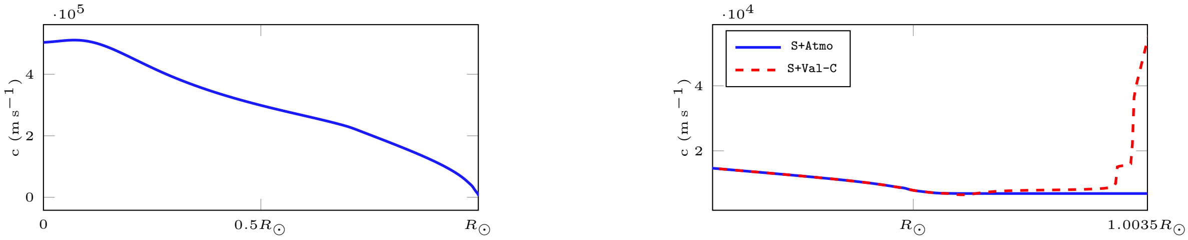

(a) Wave speed profile from model `S`.

(b) Atmospheric wave speed profiles.

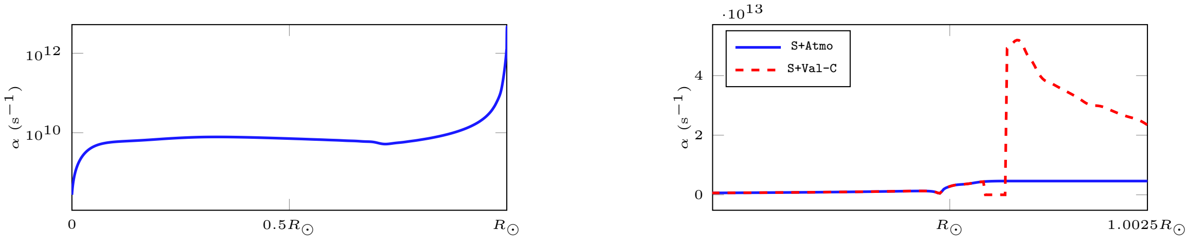

(c) α profile from model `S`.

(d) Atmospheric profiles of α.

Figure 16: Profiles of the solar parameters, the model `S` is used for the interior and is combined with the atmospheric models `Atmo` or `Val-C`.

For the computation using model `S+Atmo`, as the models are artificially smoothed, the interval of computation is ended as soon as the wave speed is constant and the density exponentially decaying (which means that α is constant). This amounts to

$$r \in [0,\, 1.0008]\,, \qquad \text{scaled computational interval for model } \texttt{S+Atmo}. \tag{9.1}$$

On the other hand, the profile `S+Val-C` is given for

$$r \in [0,\, 1.00365]\,, \qquad \text{scaled computational interval for model } \texttt{S+Val-C}. \tag{9.2}$$

9.2 Power spectrum and numerical efficiency of the radiation conditions

One of the main quantity in numerical helioseismology is the *power spectrum* $\mathcal{P}$. Under the hypothesis of energy equipartition (8.38) and supposing that the data are observed at the surface of the Sun, it is directly proportional to the imaginary part of the Green's function as given by (8.65):

$$\mathcal{P}^{\ell,m}_{\text{surf}}(\omega) \;=\; \frac{\Pi(\omega)}{2\omega}\text{Im}[\mathcal{G}_\ell(1,1,\omega)]. \tag{9.3}$$

The scaling function Π depends only on the frequency and can be given, for example, by [15, Eq. (85)],

$$\Pi(\omega) \;=\; \left(1 \,+\, \left(\frac{|\omega| - \omega_0}{\omega_1}\right)^2\right)^{-1} \qquad \text{with } \frac{\omega_0}{2\pi} = 3.3 \text{ mHz and } \frac{\omega_1}{2\pi} = 0.6 \text{ mHz}. \tag{9.4}$$

We picture the power spectrum for the model `S+Atmo` in Figure 17, for frequencies from 1 mHz to 12 mHz and modes from 1 to 1000. For the computations, we use a constant attenuation $\gamma/(2\pi) = 20$ µHz.

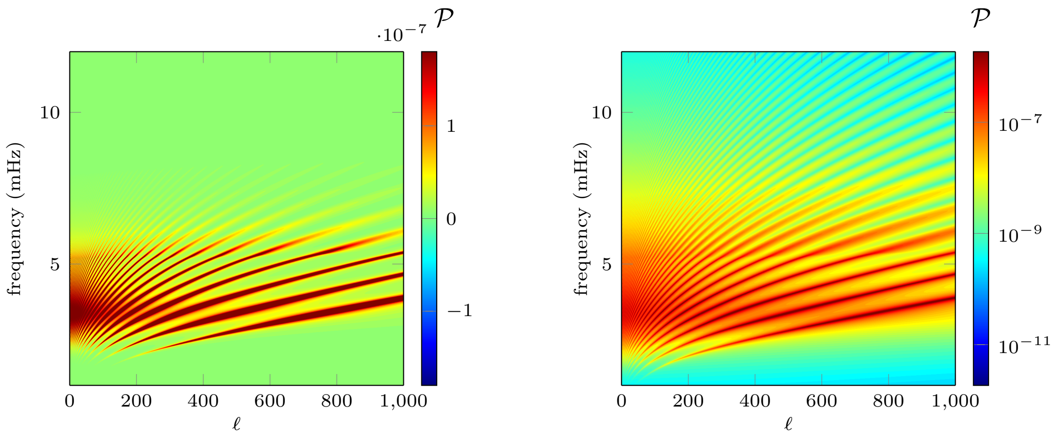

(a) Power spectrum.

(b) Power spectrum on a logarithmic scale.

Figure 17: Power spectrum (9.3) associated with the model `S+Atmo` using radiation boundary condition $\mathbf{Z}^{\ell}_{\mathrm{DtN}}$. It uses a constant attenuation $\gamma/(2\pi) = 20$ µHz.

Note that, contrary to the existing literature, our computation uses the exact Dirichlet-to-Neumann map condition $\mathbf{Z}^{\ell}_{\mathrm{DtN}}$ given in (5.2).

The high-frequency waves have less energy than the ones below the acoustic cut-off as high-frequency waves are propagating in the atmosphere and are only partly reflected back to the interior of the Sun (see Subsection 9.3). To clearly see the structure of the power spectrum at high frequencies, we also represent the spectrum on a logarithmic scale.

In order to compare the models `S+Atmo` and `S+Val-C`, we plot some slices of the power spectrum at fixed harmonic degree $\ell = 200$ in Figure 18. These simulated data are compared with a slice of the power spectrum from HMI (observed) data. The HMI power spectrum have been computed from one month of data in December 2010. In order to reduce the noise, we compute the power spectrum daily and average over the 31 realizations, see e.g., Section 2 of [21] for details. At low-frequency, Figure 18(a), the computations using the two models are very similar, and we have a good correspondence with the peak locations of the observed HMI data. The shift in the peak location is known as the "surface effect" in helioseismology as in due to the imperfect modeling of the surface by the background model `S` [30]. The widths of the peaks can be adjusted by tuning the attenuation term γ in (1.1). The attenuation should be a function of frequency and harmonic degree which was not done for this study (see e.g. Fig. 8 in [15].

On the other hand, for frequencies above the acoustic cut-off, Figure 18(b), the models `S+Atmo` and `S+Val-C` give different solutions, while none of them agree with the HMI data. Contrary to waves below the cut-off which are trapped inside the Sun, high-frequency waves are traveling into the atmosphere and are partly reflected back inside the Sun. They are thus carrying information not only about the interior but also about the structure of the atmosphere. The use of high-frequency waves to learn about the atmosphere is an interesting inverse problem but it probably requires a more sophisticated wave equation as magnetic phenomena are very important in this area.

After this comparison between models and data, we investigate the efficiency of the radiation boundary conditions for the computation of the power spectrum. In Subsection 5.3, we have evaluated their performances analytically, using the reference solutions with homogeneous background parameters. Here, we compare the efficiency for computations using the solar model `S+Atmo`, where the reference solution is given by the solution of (7.25) using the exact Dirichlet-to-Neumann map condition $\mathbf{Z}^{\ell}_{\mathrm{DtN}}$, see Figure 17. Our computational interval uses a scaled radius from 0 to 1.0008, that is, the boundary condition is set as soon as the velocity is constant and the density exponentially decaying. It is the smallest possible interval, and it allows us to clearly identify the performance in the choice of conditions. Therefore, we

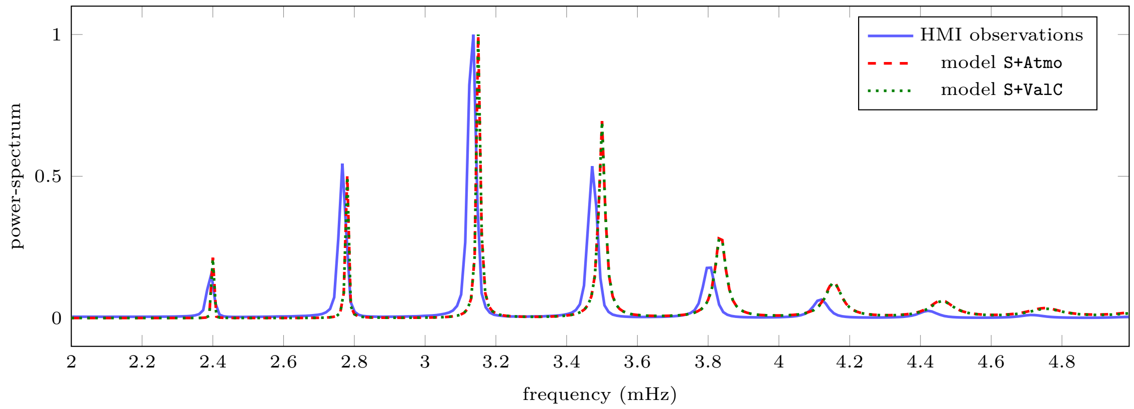

(a) Comparison at frequencies below the cut-off.

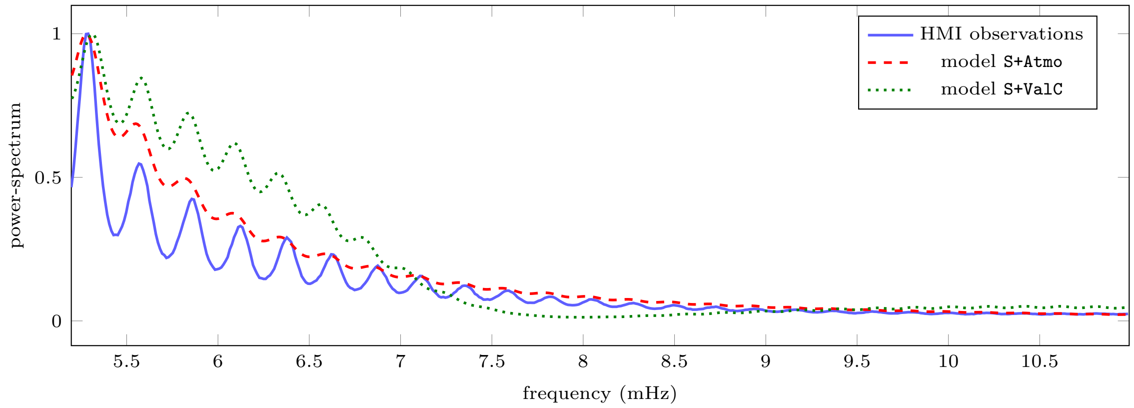

(b) Comparison at frequencies above the cut-off.

Figure 18: Comparison of the computed power spectra (9.3) using solar models `S+Atmo` and `S+Val-C` with the HMI observed data at harmonic degree $\ell = 200$. In each of the plots, the three functions are normalized to have their maximum at 1.

evaluate the performance with the relative error

$$\mathfrak{e}^{\mathcal{P}}_{\mathbf{Z}_\bullet}(\omega,\,\ell) \;=\; \frac{\|\,\mathcal{P}^{\ell}_{\mathrm{surf},\mathbf{Z}_\bullet}(\omega) \;-\; \mathcal{P}^{\ell}_{\mathrm{surf},\mathbf{Z}^{\ell}_{\mathrm{DtN}}}(\omega)\,\|}{\|\,\mathcal{P}^{\ell}_{\mathrm{surf},\mathbf{Z}^{\ell}_{\mathrm{DtN}}}(\omega)\,\|}\,, \tag{9.5}$$

where the index $\mathbf{Z}_\bullet$ indicates the choice of condition and $\mathcal{P}^{\ell}_{\mathrm{surf},\mathbf{Z}^{\ell}_{\mathrm{DtN}}}$ is the reference power spectrum computed with $\mathbf{Z}^{\ell}_{\mathrm{DtN}}$, pictured in Figure 17. The relative errors for a choice of six conditions are shown in Figure 19, in particular, we focus on the conditions that do not depend on ℓ.

We see that the nonlocal boundary condition provides the more accurate results, and that the maximum error is on a line that corresponds to the cut-off frequency, in particular for high-degree modes. On the other hand, $\mathbf{Z}^{\ell}_{\texttt{A-HF-1}}$ gives the worst results, while all other conditions give very similar errors, with a slight advantage towards $\mathbf{Z}_{\texttt{SAI-0}}$ and $\mathbf{Z}_{\texttt{S-HF-1a}}$. To confirm the observations, we provide the means of the relative errors:

$$\begin{aligned}
&\mathrm{mean}\big(\mathfrak{e}^{\mathcal{P}}_{\mathbf{Z}^{\ell}_{\mathrm{nonlocal}}}\big) &&= 1\times 10^{-5}\,, \qquad &&\mathrm{mean}\big(\mathfrak{e}^{\mathcal{P}}_{\mathbf{Z}^{\ell}_{\texttt{A-HF-1}}}\big) &&= 4.53\times 10^{-1}\,,\\
&\mathrm{mean}\big(\mathfrak{e}^{\mathcal{P}}_{\mathbf{Z}_{\texttt{S-HF-0}}}\big) &&= 9.26\times 10^{-3}\,, \qquad &&\mathrm{mean}\big(\mathfrak{e}^{\mathcal{P}}_{\mathbf{Z}_{\texttt{A-RBC-1}}}\big) &&= 9.28\times 10^{-3}\,,\\
&\mathrm{mean}\big(\mathfrak{e}^{\mathcal{P}}_{\mathbf{Z}_{\texttt{S-HF-1a}}}\big) &&= 9.10\times 10^{-3}\,, \qquad &&\mathrm{mean}\big(\mathfrak{e}^{\mathcal{P}}_{\mathbf{Z}_{\texttt{SAI-0}}}\big) &&= 9.10\times 10^{-3}\,.
\end{aligned}$$

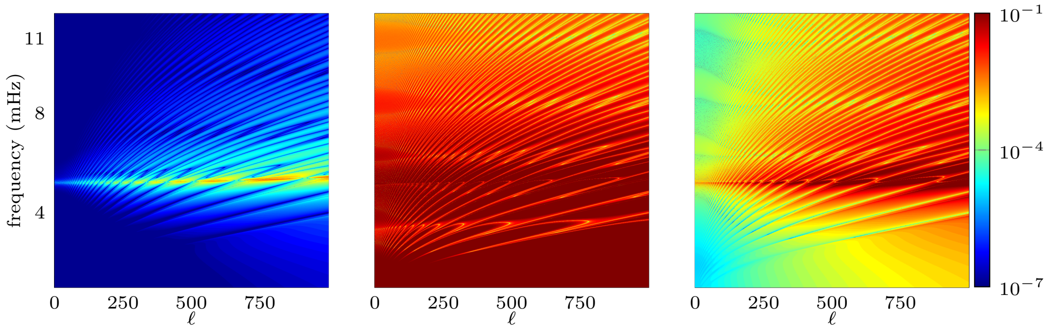

(a) $\mathfrak{e}^{\mathcal{P}}_{\mathbf{Z}^{\ell}_{\text{nonlocal}}}$ (b) $\mathfrak{e}^{\mathcal{P}}_{\mathbf{Z}^{\ell}_{\texttt{A-HF-1}}}$ (c) $\mathfrak{e}^{\mathcal{P}}_{\mathbf{Z}_{\texttt{A-RBC-1}}}$

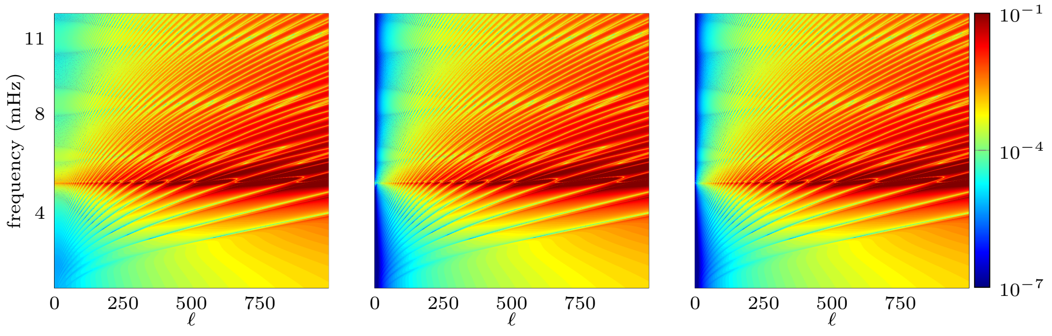

(e) $\mathfrak{e}^{\mathcal{P}}_{\mathbf{Z}_{\texttt{S-HF-0}}}$ (f) $\mathfrak{e}^{\mathcal{P}}_{\mathbf{Z}_{\texttt{S-HF-1a}}}$ (g) $\mathfrak{e}^{\mathcal{P}}_{\mathbf{Z}_{\texttt{SAI-0}}}$

Figure 19: Relative error (9.5) for the power spectrum associated with the model `S+Atmo` depending on the choice of radiation boundary condition, placed in $r_{\max} = 1.0008$. The computations use a constant attenuation $\gamma/(2\pi) = 20$ µHz.

9.3 Influence of the radiation conditions on the time-distance diagram

In this subsection, we use the set-up from [14] in order to see the difference between $\mathbf{Z}_{\texttt{S-HF-1a}}$ and $\mathbf{Z}^{\ell}_{\texttt{A-HF-1}}$ in terms of time-distance diagram. They are both high-frequencies approximations of the nonlocal RBC coefficient, however the first one is obtain in expansion with respect to k^{-1} while the latter in terms of σ^{-1}. Also $\mathbf{Z}^{\ell}_{\texttt{A-HF-1}}$ depends on ℓ but not $\mathbf{Z}_{\texttt{S-HF-1a}}$, meaning that $\mathbf{Z}_{\texttt{S-HF-1a}}$ it is much more convenient to be implemented in 3D. In order to study the behaviour of waves below and above the acoustic cut-off, we select frequencies around $\omega_{\mathrm{L}}/(2\pi) = 3$ mHz and $\omega_{\mathrm{H}}/(2\pi) = 6.5$ mHz respectively by using a Gaussian filter,

$$\tilde{\mathsf{F}}_{\bullet}(\omega_k) = \exp\left(-\frac{(|\omega_k| - \omega_{\bullet})^2}{2\sigma_{\mathrm{F}}^2}\right), \quad \text{for} \quad \bullet = \mathrm{L}, \mathrm{H}, \tag{9.6}$$

and $\sigma_{\mathrm{F}}/(2\pi) = 0.3$ mHz. We then filter around a given velocity by applying a phase-speed filter as defined in (8.9)

$$\hat{\mathsf{F}}_{\bullet}(\omega_k)_{\ell} = \exp\left(-\frac{(|\omega_k| R_{\odot}/\ell - v_{\bullet})^2}{2\delta v^2}\right), \tag{9.7}$$

with parameters $v_{\mathrm{L}} = 125.2\ \mathrm{km\,s^{-1}}$, $v_{\mathrm{H}} = 250.4\ \mathrm{km\,s^{-1}}$ and $\delta v = 12.3\ \mathrm{km\,s^{-1}}$. The final filter $\mathsf{F}_{\bullet}(\omega_k)_{\ell}$ is given by

$$\mathsf{F}_{\bullet}(\omega_k)_{\ell} \;=\; \tilde{\mathsf{F}}_{\bullet}(\omega_k)\ \hat{\mathsf{F}}_{\bullet}(\omega_k)_{\ell}\,. \tag{9.8}$$

To compute the time-distance diagram, we first compute the expectation value of the cross-covariance for surface data $\mathcal{C}_{\mathrm{surf}}$ using (8.51) (under the energy equipartition hypothesis (8.38)). In this case, the cross-covariance depends only on the angle θ between the two observation points,

$$\mathcal{C}_{\text{surf}}(\theta,\omega_k) = \frac{\Pi(\omega_k)}{8\pi\omega_k} \sum_{\ell} (2\ell+1)\ \mathsf{F}_\ell(\omega_k)^2\ \operatorname{Im}[\mathcal{G}_l(1,1,\omega_\mathrm{k})]\ \mathrm{P}_\ell(\cos\theta)\,, \tag{9.9}$$

with Π defined in (9.4) and F_ℓ in (9.8). The time-distance diagram is next obtained from the inverse Fourier transform of $\mathcal{C}_{\text{surf}}(\theta,\omega_k)$, i.e.

$$\mathcal{C}_{\text{surf}}(\theta,t_j) = h_\omega \sum_{k=-N_t/2}^{N_t/2-1} \mathcal{C}_{\text{surf}}(\theta,\omega_k)\ e^{-\mathrm{i}\,\omega_k\,t_j}\ . \tag{9.10}$$

In the above expression, the frequency resolution in frequency domain $h_\omega = 5$ µHz, and $N_t = 2^{15}$.

We represent $\mathcal{C}_{\text{surf}}(\theta,t)$ associated with filters F_L and F_H in Figure 20 and Figure 21 respectively. In Figures 20(b) and 21(b), we show cuts through the first and second skips for the boundary conditions $\mathbf{Z}_{\texttt{S-HF-1a}}$ and $\mathbf{Z}^\ell_{\texttt{A-HF-1}}$. We have the following observations:

- In Figures 20(a) and 21(a), the time-distance diagram shows clearly different skips (three in Figure 20(a) and two in Figure 21(a)) corresponding to waves going directly from $\hat{\boldsymbol{r}}_1$ to $\hat{\boldsymbol{r}}_2$, or being reflected at the surface once or several times.

- For waves below the acoustic cut-off (Figure 20), both boundary conditions looks similar because waves are reflected before the boundary due to the stratification. Nonetheless, we still observe a difference between the approximations of the RBCs, of about 3 to 4 order of magnitudes, with a clear advantage towards $\mathbf{Z}_{\texttt{S-HF-1a}}$ in Figure 20(c).

- Above the cut-off, Figure 21, we can visually observe the difference in the solutions for the two boundary conditions. The condition $\mathbf{Z}_{\texttt{S-HF-1a}}$ gives the appropriate result (that is, the closest to the $\mathbf{Z}^\ell_{\mathrm{DtN}}$) and we still have between 2 to 3 orders of magnitude difference in the accuracy, see Figure 21(c).

Thus, making the expansion of the boundary condition with respect to the wavenumber that depends on the stratification leads to an improved performance, even with a condition that is independent of the harmonic degree ℓ.

9.4 Comparisons of the Green's kernel

While the analysis of data (cross-covariance or power spectrum) supposing that the Sun has a real surface uses only the Green's function at the surface, the full Green kernel is required when the solar surface is considered as optically thin. We illustrate here the computational Approach 2, which gives access to the Green's kernel $G_\ell(r,s,\omega)$, for all r and s. For each frequency and each mode, we only need two simulations to assemble the function, which we compare for two solar models, `S+Atmo` and `S+Val-C+Atmo`. For boundary conditions, we use $\mathbf{Z}^\ell_{\mathrm{DtN}}$ for the model `S+Atmo` and $\mathbf{Z}^\ell_{\mathrm{nonlocal}}$ for the model `S+Val-C+Atmo`, the kernels are pictured in Figures 22 and 23, for different frequency and modes, using for attenuation the power law given by (2.4) and (2.5).

We see that the wavelength reduces when the waves reach the atmosphere, for the two choices of models. Between the models `S+Atmo` and `S+Val-C`, there is a difference in amplitude in the solutions, see Figure 23, that must come from the increase of the model parameters in Figure 16. Nonetheless, the patterns for the two models are quite similar. At a fixed frequency (i.e., 7 mHz in Figure 23), we observe that increasing the mode results in that the waves are concentrated near the position $(r = 1, s = 1)$, while at lower modes, the whole map has similar magnitude. In this case of (relative to the frequency) high modes, this area near the surface overpowers any other interval of the Green's function.

In the following section, we specifically make use of the Green's functions for the quantities of interest of helioseismology. We remind that the computation of $\mathcal{G}$ from G simply needs a multiplication by the density profile as given in (4.4).

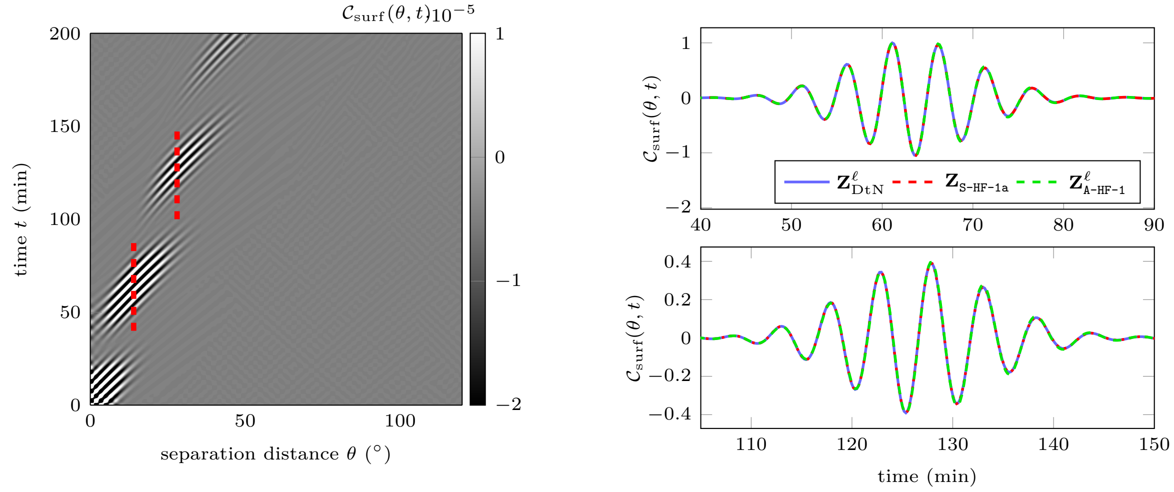

(a) Time-distance diagram with the DtN boundary condition.

(b) Skips at $\theta = 14°$ (top) and $\theta = 28°$ (bottom).

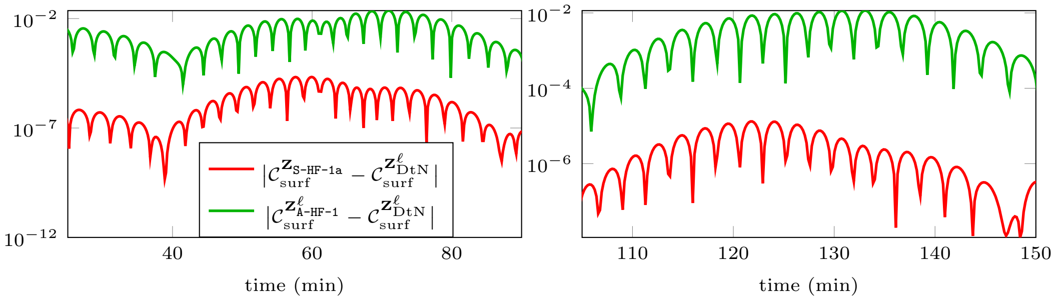

(c) Difference depending on the choice of boundary conditions for the two skips.

Figure 20: Time-distance diagram representing the expectation value of the filtered cross-covariance given in (9.10) with a phase-speed filter centered at 3 mHz (i.e. with $\mathsf{F}_{\rm L}(\omega)_\ell$ in (9.8)) as a function of separation distance and time: two-dimensional diagram and sections for $\theta = 14°$ and $\theta = 28°$, indicated by the red dashed lines on the left panel.

9.5 On the importance of the approach 2 for time-distance helioseismology

From the full Green's function $\mathcal{G}_\ell(r,s)$ computed for all sources s and receivers r using Approach 2, we can compute efficiently the cross-covariance by taking into account the contributions from different depths using (8.52)

$$\mathcal{C}_{\rm int}(\hat{\boldsymbol r}_1,\hat{\boldsymbol r}_2,\omega_k) = \frac{\Pi(\omega_k)}{8\pi\omega_k}\sum_{\ell=0}^{L_{\max}}(2\ell+1)\ \mathrm{P}_\ell(\cos\theta)\int\!\!\int K(r,\hat{\boldsymbol r}_1)K(r',\hat{\boldsymbol r}_2)\frac{\mathrm{Im}[\mathcal{G}_{\rm l}(\mathrm{r},\mathrm{r}',\omega_{\rm k})]}{rr'}drdr', \tag{9.11}$$

or (8.53)

$$\mathcal{C}_{\rm depth}(\hat{\boldsymbol r}_1,\hat{\boldsymbol r}_2,\omega_k) = \frac{\Pi(\omega_k)}{8\pi\omega_k}\frac{1}{\mathrm{r}_{\rm fh}(\hat{\boldsymbol r}_1)\ \mathrm{r}_{\rm fh}(\hat{\boldsymbol r}_2)}\sum_{\ell=0}^{L_{\max}}(2\ell+1)\ \mathrm{Im}[\mathcal{G}_{\rm l}(\mathrm{r}_{\rm fh}(\hat{\boldsymbol r}_2),\mathrm{r}_{\rm fh}(\hat{\boldsymbol r}_1),\omega_{\rm k})]\mathrm{P}_\ell(\cos\theta_{\hat{\boldsymbol r}_1\cdot\hat{\boldsymbol r}_2}), \tag{9.12}$$

and compare it with the classic approach (8.51)

$$\mathcal{C}_{\rm surf}(\hat{\boldsymbol r}_1,\hat{\boldsymbol r}_2,\omega_k) = \frac{\Pi(\omega_k)}{8\pi\omega_k}\sum_{\ell=0}^{L_{\max}}(2\ell+1)\ \mathrm{Im}[\mathcal{G}_{\rm l}(1,1,\omega_{\rm k})]\ \ \mathrm{P}_\ell(\cos\theta_{\hat{\boldsymbol r}_1\cdot\hat{\boldsymbol r}_2}). \tag{9.13}$$

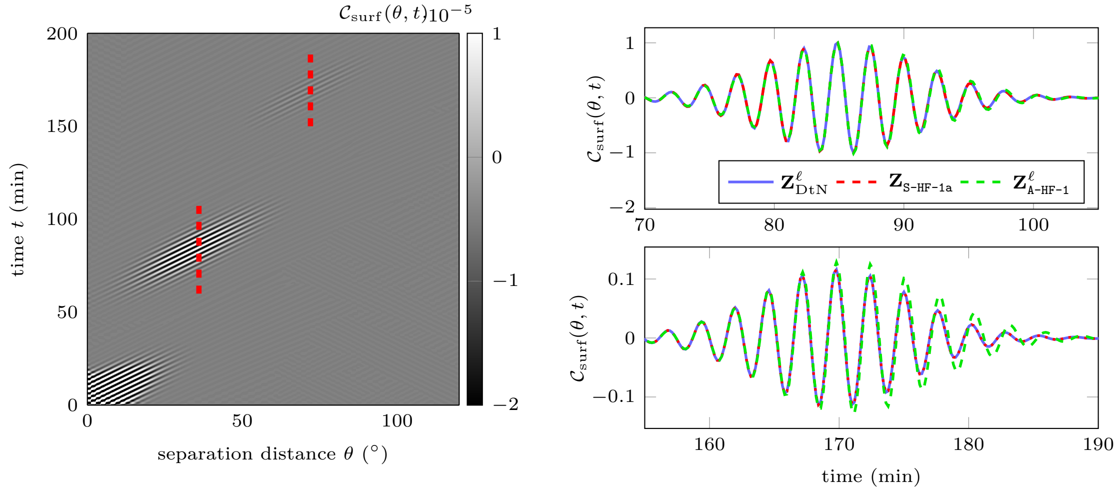

(a) Time-distance diagram with the DtN boundary condition.

(b) Skips at $\theta = 36°$ (top) and $\theta = 72°$ (bottom).

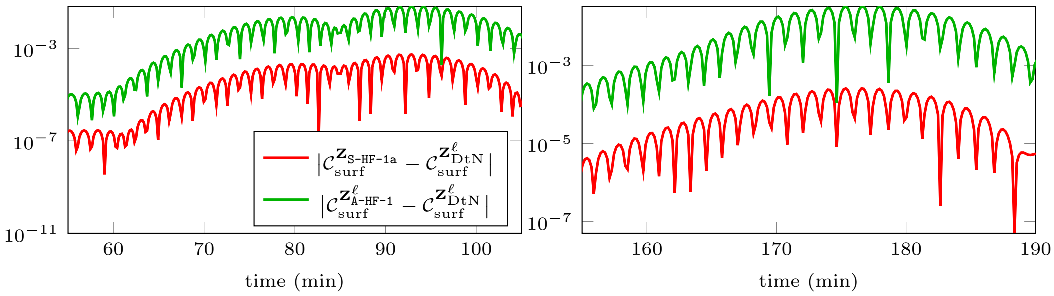

(c) Difference depending on the choice of boundary conditions for the two skips.

Figure 21: Time-distance diagram representing the expectation value of the filtered cross-covariance given in (9.10) with a phase-speed filter centered at 6.5 mHz (i.e. with $\mathsf{F}_{\mathrm{H}}(\omega)_\ell$ in (9.8)) as a function of separation distance and time: two-dimensional diagram and sections for $\theta = 36°$ and $\theta = 72°$, indicated by the red dashed lines on the left panel.

Contrary to Subsection 9.3, we do not use a specific filter to select particular waves but just keep the harmonic degrees up to $L_{\max} = 300$. The function Π is the same than before and is given by (9.4). For our numerical experiments, we work with a simplified contribution function K given in (8.25)

$$K(r, \hat{\boldsymbol{r}}_1) \;=\; \frac{1}{\sqrt{2\pi}\;\sigma} \exp\left(-\frac{(r - r_{\mathrm{fh}}(\hat{\boldsymbol{r}}_1))^2}{2\sigma^2}\right) \tag{9.14}$$

and formation height in (8.26)

$$r_{\mathrm{fh}}(\hat{\boldsymbol{r}}_1) = r_{\mathrm{eq}} + (r_{\mathrm{pole}} - r_{\mathrm{eq}}) \cos^2(\theta_1) \cos^2(\phi_1), \tag{9.15}$$

with

$$\sigma\, R_\odot = 50 \text{ km} \quad ; \quad \mathrm{r_{eq}}\, \mathrm{R}_\odot = 0 \text{ km} \quad , \quad \text{and } \mathrm{r_{pole}}\, \mathrm{R}_\odot = 300 \text{ km}\,. \tag{9.16}$$

In our numerical experiments, we compute the cross-covariance using $L_{\max} = 300$ in (9.11)–(9.13). We then take the inverse Fourier transform and represent the cross-covariance as a function of time for points

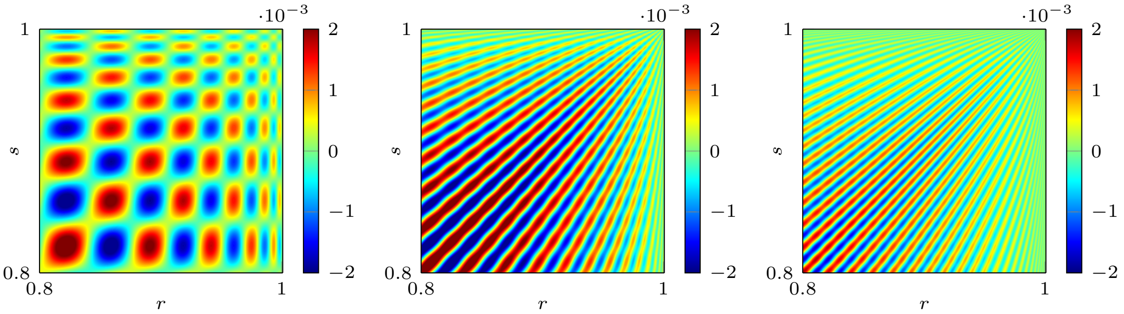

(a) Imaginary part at 3 mHz. (b) Imaginary part at 7 mHz. (c) Imaginary part at 12 mHz.

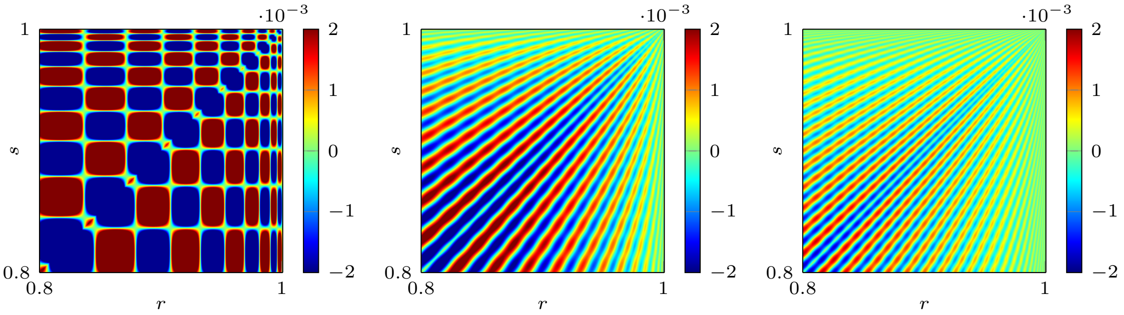

(d) Real part at 3 mHz. (e) Real part at 7 mHz. (f) Real part at 12 mHz.

Figure 22: Solar Green's functions $G_\ell(r,s,\omega)$ for the model `S+Atmo`, for mode $\ell = 0$.

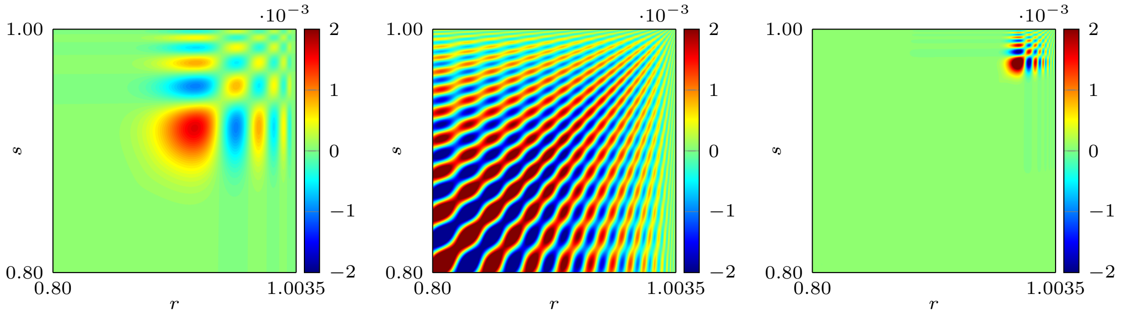

(a) 3 mHz, $\ell = 100$, model `S+Atmo`. (b) 7 mHz, $\ell = 100$, model `S+Atmo`. (c) 7 mHz, $\ell = 500$, model `S+Atmo`.

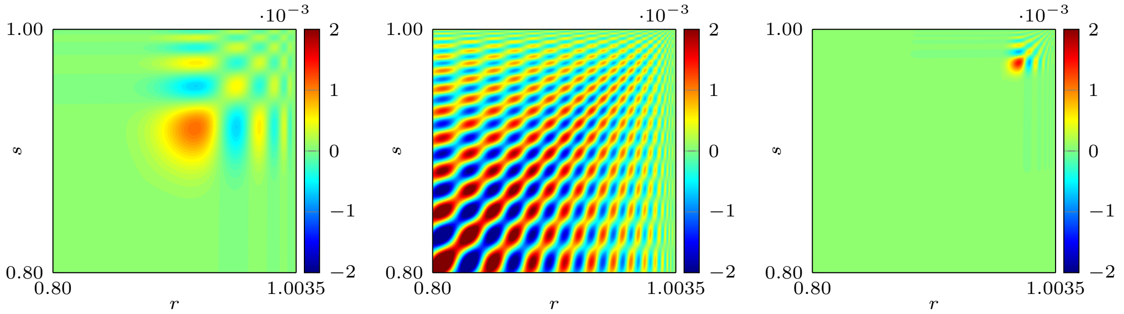

(d) 3 mHz, $\ell = 100$, model `S+Val-C`. (e) 7 mHz, $\ell = 100$, model `S+Val-C`. (f) 7 mHz, $\ell = 500$, model `S+Val-C`.

Figure 23: Imaginary parts of the solar Green's functions $G_\ell(r,s,\omega)$ for the models `S+Atmo` and `S+Val-C`.

$\hat{\boldsymbol{r}}_1 = (\pi/2, 0)$ at the equator and $\hat{\boldsymbol{r}}_2 = (2\pi/3, 0)$ corresponding to a latitude of 30° in Figure 25,

$$\mathcal{C}_\bullet(\hat{\boldsymbol{r}}_1, \hat{\boldsymbol{r}}_2, t_j) = h_\omega \sum_{k=-N_t/2}^{N_t/2-1} \mathcal{C}_\bullet(\hat{\boldsymbol{r}}_1, \hat{\boldsymbol{r}}_2, \omega_k)\, e^{-\mathrm{i}\,\omega_k\, t_j}\,; \quad \text{with} \quad \bullet \;=\; \text{surf}, \text{int}, \text{depth} \tag{9.17}$$

We use the same frequency space h_ω and N_t as in (9.10). The integration in (9.12) is theoretically going form 0 to infinity. However, due to the shape of the function K (and more generally to the opacity of the Sun), we integrate from -300 km to $+500$ km which corresponds to a distance of at least 4σ to the center of the Gaussian. The integration is done using the trapezoidal rule.

In order to have a better idea of the differences between the three definitions of the cross-covariances, $\mathcal{C}^{\text{surf}}$, $\mathcal{C}^{\text{int}}$ and $\mathcal{C}^{\text{depth}}$ (given in (9.17)), we compute the travel-time perturbation $\delta\tau$ using (8.17),

$$\begin{aligned} \delta\tau(\hat{\boldsymbol{r}}_1, \hat{\boldsymbol{r}}_2) &= \int_{-\infty}^{\infty} W_\tau(\hat{\boldsymbol{r}}_1, \hat{\boldsymbol{r}}_2, t)\,\big(\mathcal{C}(\hat{\boldsymbol{r}}_1, \hat{\boldsymbol{r}}_2, t) - \mathcal{C}^{\text{ref}}(\hat{\boldsymbol{r}}_1, \hat{\boldsymbol{r}}_2, t)\big)\, dt, \\ \text{with} \quad W_\tau(\hat{\boldsymbol{r}}_1, \hat{\boldsymbol{r}}_2, t) &= -\frac{w(t)\partial_t \mathcal{C}^{\text{ref}}(\hat{\boldsymbol{r}}_1, \hat{\boldsymbol{r}}_2, t)}{\int_{-\infty}^{\infty} w(t')\partial_t \mathcal{C}^{\text{ref}}(\hat{\boldsymbol{r}}_1, \hat{\boldsymbol{r}}_2, t')^2 dt'}\,, \end{aligned} \tag{9.18}$$

and the amplitude differences $\delta\mathfrak{a}$ using (8.18),

$$\begin{aligned} \delta\mathfrak{a}(\hat{\boldsymbol{r}}_1, \hat{\boldsymbol{r}}_2) &= \int_{-\infty}^{\infty} W_{\mathfrak{a}}(\hat{\boldsymbol{r}}_1, \hat{\boldsymbol{r}}_2, t)\,\big(\mathcal{C}(\hat{\boldsymbol{r}}_1, \hat{\boldsymbol{r}}_2, t) - \mathcal{C}^{\text{ref}}(\hat{\boldsymbol{r}}_1, \hat{\boldsymbol{r}}_2, t)\big)\, dt\,, \\ \text{with} \quad W_{\mathfrak{a}}(\hat{\boldsymbol{r}}_1, \hat{\boldsymbol{r}}_2, t) &= \frac{w(t)\mathcal{C}^{\text{ref}}(\hat{\boldsymbol{r}}_1, \hat{\boldsymbol{r}}_2, t)}{\int_{-\infty}^{\infty} w(t')\mathcal{C}^{\text{ref}}(\hat{\boldsymbol{r}}_1, \hat{\boldsymbol{r}}_2, t')^2 dt'}\,. \end{aligned} \tag{9.19}$$

As it is the usual choice in helioseismology, we first use $\mathcal{C}^{\text{ref}} := \mathcal{C}_{\text{surf}}$ for Figure 26. However, $\mathcal{C}_{\text{int}}$ is supposed to be a better representation of the observed cross-covariance and we also use it as reference, $\mathcal{C}^{\text{ref}} := \mathcal{C}_{\text{int}}$, for Figure 27. For our numerical experiment, we fix $\hat{\boldsymbol{r}}_1$ the equator $\hat{\boldsymbol{r}}_1 = (\pi/2, 0)$ and vary $\hat{\boldsymbol{r}}_2$ in the form $\hat{\boldsymbol{r}}_2 = (\theta_2, 0)$. We represent $\delta\tau$ and $\delta\mathfrak{a}$ as functions of $\theta_2 \in [0, \pi/2]$. We note that when $\theta_2 \to 0$, we approach the 'limb' (or the edge) of the Sun.

In order to compute the weighting function W_τ in (9.18) and $W_{\mathfrak{a}}$ in (9.19), one needs a window function w in order to select the first-skip wave packet. We follow [21] to use w in the form of a rectangular function, of width 20 mins with center t_{ctr}

$$w(\theta_{\hat{\boldsymbol{r}}_1 \cdot \hat{\boldsymbol{r}}_2}\,,\, t) \;=\; \begin{cases} 1\,, & |t - t_{\text{ctr}}(\theta_{\hat{\boldsymbol{r}}_1 \cdot \hat{\boldsymbol{r}}_2})| \leq 10\text{min}\,; \\ 0\,, & \text{otherwise} \end{cases}\,. \tag{9.20}$$

The center $t_{\text{ctr}}(\theta_{\hat{\boldsymbol{r}}_1 \cdot \hat{\boldsymbol{r}}_2})$ is obtained using the ray approximation and is ploted in Figure 24. Similar numerical values for centers can be found in the second column of Table A.1 of [20]. The derivative of $\mathcal{C}_{\text{ref}}$ is computed using sixth-order finite differences. The integrals in frequencies are going from $-\omega_{\max}$ to $\omega_{\max}$ where $\omega_{\max}$ is the Nyquist frequency in the case of observations. For example, for HMI $\omega_{\max}/(2\pi) = 11.1$ mHz, see Section 8. Here, we use $\omega_{\max}/(2\pi) = 12$ mHz and integrate using the trapezoidal rule.

We have the following observations.

- Close to the equator the cross-covariances are close to each other and there is only a small time-lag as the formation height $r_{\text{fh}}(\hat{\boldsymbol{r}}_2)$ is close to the solar surface (8.26). However, getting closer to the limb ($\theta_2 \to 0$), the formation height is around 300 kms above the surface, generating a travel-time difference of about 0.3 s. This difference is significant as the measurements of travel-times to infer the meridional flow at the surface of the Sun are smaller than 1 s [21].

- On the other hand, depending on the formulation, the amplitude of the cross-covariance changes but there is no general trend depending on θ_2. The amplitude differences are up to 2% and are more difficult to interpret than travel-time measurements. Such measurements have not yet been used to infer the solar interior so it is not clear if this modeling error is significant or not.

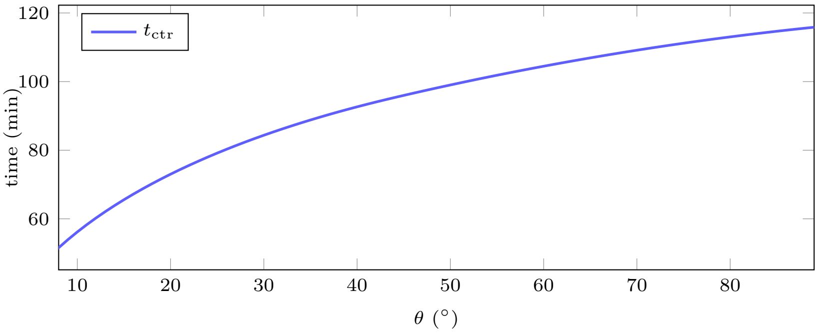

Figure 24: Function $t_{\mathrm{ctr}}(\theta)$ used for the computation of the weighting function w (9.20).

As mentioned above, since our numerical experiments currently use a simplified contribution function K, we expect more definitive conclusions with a more accurate contribution function, e.g. one computed from the opacity in the solar atmosphere. Nonetheless, we already observe that integrating over depth leads to significant differences compared to computations at a fixed height, see Figure 27.

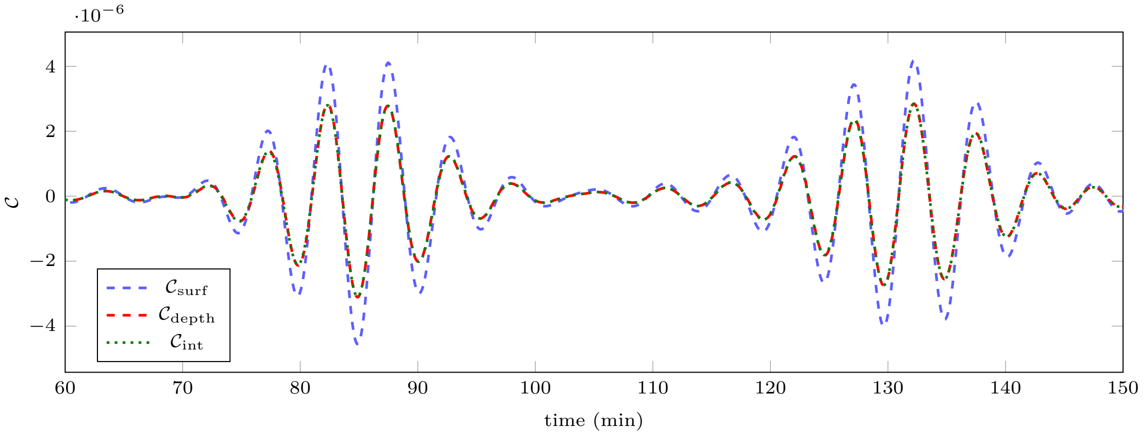

Figure 25: Comparison of the expectation value of the cross-covariance function $\mathcal{C}(\hat{\boldsymbol{r}}_1, \hat{\boldsymbol{r}}_2, t)$ between the points $\hat{\boldsymbol{r}}_1 = (\pi/2, 0)$ and $\hat{\boldsymbol{r}}_2 = (2\pi/3, 0)$ as a function of time for the different types of observables $\mathcal{C}_{\mathrm{surf}}$, $\mathcal{C}_{\mathrm{int}}$ and $\mathcal{C}_{\mathrm{depth}}$ as defined by (8.51)–(8.53) under the hypothesis of energy equipartition (8.38).

10 Conclusion

In this work, we have proposed a two-step algorithm to compute efficiently and accurately the full outgoing modal Green kernels for the scalar wave equation in local helioseismology under spherical symmetry. It gives $G_\ell(r, s)$ for all pairs of sources and receivers at a given frequency and harmonic degree from only two simulations. It is computationally way more efficient than the classical method (approach 1) which requires as many simulations as sources and it is more accurate as it treats analytically the singularity at the source location. Without this two-step algorithm, the full Green's kernel are expensive to compute which limited their use in local helioseismology.

Below are the tasks that were carried out in this work.

1. The implementation of the algorithm with the HDG discretization is validated with analytical solutions for the pure Atmo problem.
2. The algorithm with the HDG discretization and exact DtN coefficient is used to obtain high-definition modal Green kernels for realistic solar background.

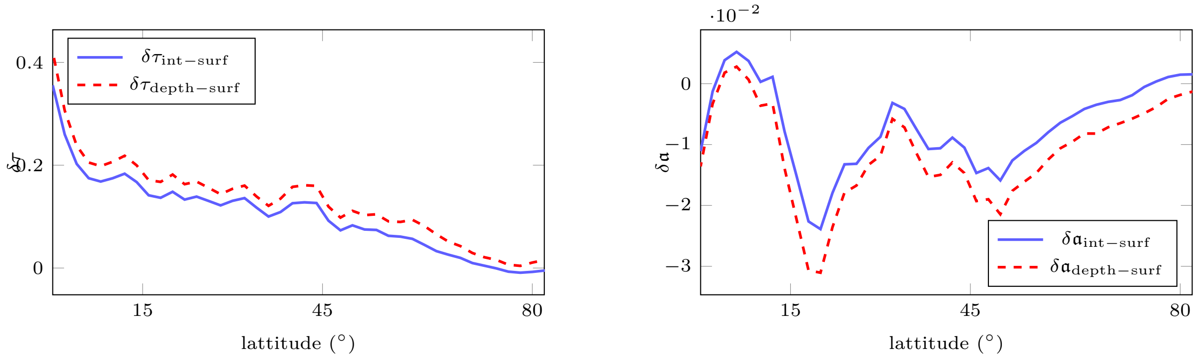

(a) Travel-time (b) Amplitude

Figure 26: Travel time $\delta\tau(\hat{\boldsymbol{r}}_1, \hat{\boldsymbol{r}}_2)$ (8.17) and amplitude $\delta\mathfrak{a}(\hat{\boldsymbol{r}}_1, \hat{\boldsymbol{r}}_2)$ (8.18) between $\mathcal{C}_{\text{surf}}$ and $\mathcal{C}_{\text{int}}$ or $\mathcal{C}_{\text{depth}}$. The point $\hat{\boldsymbol{r}}_1$ is fixed at the equator $\hat{\boldsymbol{r}}_1 = (\pi/2, 0)$ and the point $\hat{\boldsymbol{r}}_2 = (\theta_2, 0)$ is varying with $0 < \theta_2 < \pi/2$.

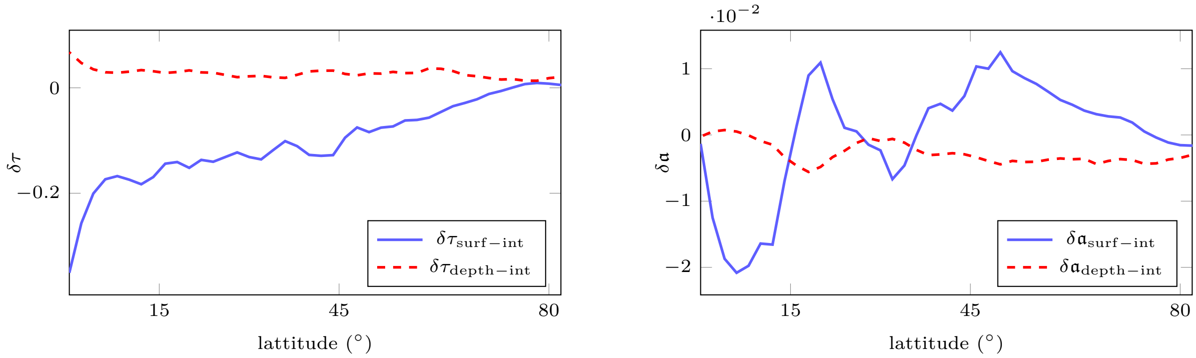

(a) Travel-time (b) Amplitude

Figure 27: Travel time $\delta\tau(\hat{\boldsymbol{r}}_1, \hat{\boldsymbol{r}}_2)$ (8.17) and amplitude $\delta\mathfrak{a}(\hat{\boldsymbol{r}}_1, \hat{\boldsymbol{r}}_2)$ (8.18) between $\mathcal{C}_{\text{int}}$ and $\mathcal{C}_{\text{surf}}$ or $\mathcal{C}_{\text{depth}}$. The point $\hat{\boldsymbol{r}}_1$ is fixed at the equator $\hat{\boldsymbol{r}}_1 = (\pi/2, 0)$ and the point $\hat{\boldsymbol{r}}_2 = (\theta_2, 0)$ is varying with $0 < \theta_2 < \pi/2$.

3. Explicit expressions of helioseismic products (power spectrum and cross-covariance) are derived in terms of Green's function under varying assumptions on the correlation of sources and different types of simulated observables.

4. We have investigated the influence of the radiation boundary conditions on the helioseismic products and confirmed the robustness of those obtained in [4, 5]. In particular, we have shown that among the family of high-frequency approximations of the RBC, the conditions that are independent of the harmonic mode provides high-accuracy results.

5. We have presented an application where the full Green kernel allows for a more physical treatment of the Sun's surface, being optically thin. We have shown that using depth-integrated observables lead to a significant travel-time difference compared to taking into account only the contributions from the surface.

Acknowledgments

This work is supported by the Inria associated-team Ants (Advanced Numerical meThods for helioSeismology) between project-team Inria Magique 3D and the Max Planck Institute for Solar System Research in Göttingen. FF is funded by the Austrian Science Fund (FWF) under the Lise Meitner fellowship M

2791-N. The numerical experiments have been performed as part of the GENCI resource allocation project AP010411013.

A Further discussion on modal Green's function

A.1 Modal Green's formula with Heaviside function

In this appendix, we characterize a Green function associated to operator L,

$$\mathsf{L}u \;:=\; -\big(a(r)\,u'\big)' \;+\; b(r)\,u\,, \tag{A.1}$$

on $(0,\infty)$. In particular, we derive the formula of the Green kernel built from two homogeneous solutions associated to L, employed in Subsection 4.2.2. We first introduce the needed notations. Denote by

$$\mathcal{D} \;:=\; \mathcal{C}_c^{\infty}(0,\infty)\,. \tag{A.2}$$

the space of smooth and compactly supported functions on $(0,\infty)$. We follow usual convention and consider the (translated) delta-distribution $\delta(r-s)$ given by

$$\langle \delta(r-s)\,,\,\phi(r)\rangle_{\mathcal{D}',\mathcal{D}} \;=\; \phi(s)\,, \tag{A.3}$$

and we denote by H the Heaviside function. We denote by $\mathcal{W}\{\psi(s)\,,\,\tilde{\psi}(s)\}$ the Wronskian of two functions ψ and $\tilde{\psi}$, i.e.,

$$\mathcal{W}\{\psi(s)\,,\,\tilde{\psi}(s)\} \;:=\; \psi(s)\,\tilde{\psi}'(s) \;-\; \tilde{\psi}(s)\,\psi'(s)\,. \tag{A.4}$$

We also write the left and right-hand-side limit of a function as,

$$f(s^{\pm}) \;:=\; \lim_{r\to s^{\pm}} f(r)\,. \tag{A.5}$$

For simplicity, we assume $a(r) > 0 \in \mathcal{C}^1(0,\infty)$ and $b(r) \in \mathcal{C}(0,\infty)$ with $b(r) \in \mathsf{O}(r^{-1})$ and $a(r)$ constant outside of a compact neighborhood of $r=0$.

Proposition 2. *A Green function G defined (A.8) is in $\mathcal{C}(0,\infty) \cap \mathcal{C}^2\big((0,s)\cup(s,\infty)\big)$. Its jump at $r=s$ is given by*

$$G'(s^-) \;-\; G'(s^+) \;=\; \frac{1}{a(s)}\,. \tag{A.6}$$

As a result, G has the form,

$$G_\ell(r,s) \;=\; \frac{-\mathrm{H}(s-r)\,\psi(r)\,\tilde{\psi}(s) \;-\; \mathrm{H}(r-s)\,\tilde{\psi}(r)\;\psi(s)}{a(s)\,\mathcal{W}(s)}\,, \tag{A.7}$$

where $\tilde{\psi}_\ell$ and ψ_ℓ are two homogeneous solutions associated to L, with $\mathsf{L}\tilde{\psi} = 0$ on $(0,s)$ and $\mathsf{L}\psi = 0$ on (s,∞), and $\mathcal{W}(s) := \mathrm{W}\{\psi(s)\,,\,\tilde{\psi}(s)\}$.

Proof. **Statement 1** By definition, $G(r) = G_s(r)$ is a distributional solution on $[0,\infty)$ to

$$-\big(a(r)\,G'\big)' \;+\; b(r)\,G \;=\; \delta(r-s)\,. \tag{A.8}$$

The regularity imposed on G is observed from the fact that two distributional derivations result in a delta distribution. In addition, G is a classical solution i.e. $\mathcal{C}^2$ on $(0,\infty)\setminus\{s\}$. Specifically,

$$-\big(a(r)\,G'\big)' \;+\; b(r)\,G \;=\; 0 \quad \text{on } (0,s)\,\cup\,(s,\infty)\,. \tag{A.9}$$

The derivatives in (A.8) are distributional derivatives, and for a test function $\phi \in \mathcal{C}_c^{\infty}(0,\infty)$, we have

$$\big\langle G\,,\,-(a(r)\,\phi'(r))' \;+\; b(r)\,\phi(r)\big\rangle_{\mathcal{D}',\mathcal{D}} \;=\; \phi(s)\,. \tag{A.10}$$

With G being a continuous function on $(0,\infty)$, its action can be written as

$$\mathbb{I} \;:=\; \big\langle G\,,\, -(a(r)\,\phi'(r))'\;,\; \phi(r)\big\rangle_{\mathcal{D}',\mathcal{D}} \;=\; \int_0^\infty G(r)\,\big(-(a(r)\phi')'\,dr\,; \tag{A.11a}$$

$$\Rightarrow \quad \mathbb{I} \;=\; \left(\int_0^s + \int_s^\infty\right) G(r)\,\big(-(a(r)\phi')'\,dr\,. \tag{A.11b}$$

and (A.10) can be written as

$$\mathbb{I} \;+\; \int_0^\infty b(r)\,\phi(r)\,ds \;=\; \phi(s)\,. \tag{A.12}$$

Integrate each integral by parts, we obtain

$$\mathbb{I} \;=\; \left(\int_0^s + \int_s^\infty\right) G'(r)\,a(r)\,\phi'(r)\,dr \;\underbrace{-\;G(s^-)\,a(s^-)\,\phi'(s^-)\;+\;G(s^+)\,a(s^+)\,\phi'(s+)}_{=\,0}\,. \tag{A.13}$$

Since G, a and ϕ are continuous at $r = r_s$, the above jump is zero. Continue to integrate the above integrals by parts

$$\mathbb{I} \;=\; -\left(\int_0^s + \int_s^\infty\right) (G'a(r))'\,\phi(r)\,dr \;+\; G'(s^-)\,a(s^-)\,\phi(s^-) \;-\; G'(s^+)\,a(s^+)\,\phi(s^+)\,. \tag{A.14}$$

Substitute this back in the left-hand-side of (A.12), we obtain

$$\begin{aligned} -\left(\int_0^s + \int_s^\infty\right) (G'a(r))'\,\phi(r)\,dr \;+\; \int_0^\infty b(r)\,\phi(r)\,dr \qquad\qquad& \\ +\; G'(s^-)\,a(s^-)\,\phi(s^-) \;-\; G'(s^+)\,a(s^+)\,\phi(s^+) \;=\; \phi(s)\,.& \end{aligned} \tag{A.15}$$

$$\Rightarrow \quad \underbrace{\left(\int_0^s + \int_s^\infty\right)\big(-(G'a(r))' \,+\, b(r)\big)\,\phi(r)\,dr}_{=0 \text{ due to (A.9)}} \;+\, G'(s^-)\,a(s^-)\,\phi(s^-) \;-\; G'(s^+)\,a(s^+)\,\phi(s^+) \;=\; \phi(s)\,. \tag{A.16}$$

We thus arrive at

$$G'(s^-)\,a(s^-)\,\phi(s^-) \;-\; G'(s^+)\,a(s^+)\,\phi(s^+) \;=\; \phi(s)\,. \tag{A.17}$$

Since $a > 0$ and with ϕ chosen so that $\phi(s) > 0$, we obtain the value of the jump of G' at $r = s$.

Statement 2 From its properties obtained in Statement 1, we next obtain (A.7). If we define

$$\psi(r) \;:=\; G|_{(0,s)} \quad,\quad \tilde{\psi}(r) \;:=\; G|_{(s,\infty)}\,, \tag{A.18}$$

using (A.9), we have that ψ and $\tilde{\psi}$ are two homogeneous solutions associated to L on $(0,s)$ and (s,∞) respectively. In addition, they satisfy the continuity and jump (A.6) at $r = s$,

$$\begin{pmatrix} \psi(s) & -\tilde{\psi}(s) \\ \psi'(s) & -\tilde{\psi}'(s) \end{pmatrix} \begin{pmatrix} 1 \\ 1 \end{pmatrix} \;=\; \begin{pmatrix} 0 \\ \frac{1}{a(s)} \end{pmatrix}. \tag{A.19}$$

$$\Rightarrow \quad \begin{pmatrix} 1 \\ 1 \end{pmatrix} \;=\; -\frac{1}{\mathcal{W}(s)} \begin{pmatrix} -\tilde{\psi}'(s) & \tilde{\psi}(s) \\ -\psi'(s) & \psi(s) \end{pmatrix} \begin{pmatrix} 0 \\ \frac{1}{a(s)} \end{pmatrix} \;=\; -\frac{1}{a(s)\,\mathcal{W}(s)} \begin{pmatrix} \tilde{\psi}(s) \\ \psi(s) \end{pmatrix}. \tag{A.20}$$

Thus

$$\begin{aligned} G(r,s) \;&=\; \mathrm{H}(s-r)\,\psi(r) \;+\mathrm{H}(r-s)\,\tilde{\psi}(r) \\ &=\; -H(s-r)\,\psi(r)\,\frac{\tilde{\psi}(s)}{a(s)\,\mathcal{W}(s)} \;-\; H(r-s)\,\tilde{\psi}(r)\,\frac{\psi(s)}{a(s)\,\mathcal{W}(s)}\,. \end{aligned} \tag{A.21}$$

□

Remark 10. *Instead of* (A.18)*, a more constructive approach to obtain G is specified by a boundary condition at $r=0$ and as $r\to\infty$. These boundary conditions determine a basis of family of homogeneous solutions $\{c\mathrm{y}_1\}$ and $\{d\mathrm{y}_2\}$ associated to L and these conditions and on $(0,s)$, (s,∞) respectively. Then*

$$G = \begin{cases} c\,\mathrm{y}_1(r) & ,\ 0\le r<s \\ d\,\mathrm{y}_2 & ,\ r>s \end{cases}, \tag{A.22}$$

with constants c and d are determined from the continuity and jump condition at $r=s$,

$$\begin{pmatrix} \mathrm{y}_1(s) & -\mathrm{y}_2(s) \\ \mathrm{y}_1'(s) & -\mathrm{y}_2'(s) \end{pmatrix} \begin{pmatrix} c \\ d \end{pmatrix} = \begin{pmatrix} 0 \\ \frac{1}{a(s)} \end{pmatrix} \tag{A.23}$$

$$\Rightarrow \begin{pmatrix} c \\ d \end{pmatrix} = -\frac{1}{\mathcal{W}\{\mathrm{y}_1\,,\,\mathrm{y}_2\}(s)} \begin{pmatrix} -\mathrm{y}_2'(s) & \mathrm{y}_2(s) \\ -\mathrm{y}_1'(s) & \mathrm{y}_1(s) \end{pmatrix} \begin{pmatrix} 0 \\ \frac{1}{a(s)} \end{pmatrix} = -\frac{1}{\mathcal{W}\{\mathrm{y}_1,\mathrm{y}_2\}(s)} \begin{pmatrix} \mathrm{y}_2(s) \\ y_1(s) \end{pmatrix}, \tag{A.24}$$

and

$$G(r,s) = -\mathrm{H}(s-r)\,\mathrm{y}_1(r)\,\frac{\mathrm{y}_2(s)}{\mathcal{W}\{\mathrm{y}_1,\mathrm{y}_2\}(s)} - \mathrm{H}(r-s)\,\mathrm{y}_2(r)\,\frac{\mathrm{y}_1(s)}{\mathcal{W}\{\mathrm{y}_1,\mathrm{y}_2\}(s)}. \tag{A.25}$$

△

A.2 Expansion of 3D kernel in spherical harmonics

Here we verify the expansion (4.11) of G,

$$\left(-\Delta_{\mathbf{x}} - \frac{\sigma^2(r)}{\mathfrak{c}^2(r)} + \mathsf{q}\right) G = \delta(\mathbf{x}-\mathbf{s}) \tag{A.26}$$

in terms of the spherical harmonics and the modal outgoing kernel G_ℓ given by (4.17). We recall the modal operator,

$$\mathsf{L}_\ell := -\frac{d^2}{dr^2} + \frac{Q(r)}{r^2} = -\frac{d^2}{dr^2} - \frac{\sigma^2(r)}{\mathfrak{c}^2(r)} + \mathsf{q}(r) + \frac{\ell(\ell+1)}{r^2}. \tag{A.27}$$

For $g\in L^2_c(\mathbb{R}^3)$, and $u=(-\Delta-\frac{\sigma^2(r)}{\mathfrak{c}^2(r)}+\mathsf{q})^{-1}$, we write u and g in their harmonic expansion, for $\mathbf{x}$ not on the z-axis,

$$u = \sum_{\ell=0}^{\infty}\sum_{m=-\ell}^{\ell} \frac{w_\ell^m}{r}\mathrm{Y}_\ell^m \quad , \quad g = \sum_{\ell=0}^{\infty}\sum_{m=-\ell}^{\ell} \frac{h_\ell^m}{r}\mathrm{Y}_\ell^m$$

with

$$\frac{w_\ell^m}{r} = \int_0^\pi\int_0^{2\pi} u(r,\theta,\phi)\,\overline{\mathrm{Y}_\ell^m}(\theta,\phi)\,\sin\theta\,d\phi\,d\theta\,.$$

Substitute the two expansions in the equation

$$\begin{aligned} &\left(-\Delta - \frac{\sigma^2(r)}{\mathfrak{c}^2(r)} + \mathsf{q}\right) u = g \\ \Rightarrow &\left(-\Delta - \frac{\sigma^2(r)}{\mathfrak{c}^2(r)} + \mathsf{q}\right) \sum_{\ell=0}^{\infty}\sum_{m=-\ell}^{\ell} \frac{w_\ell^m}{r}\mathrm{Y}_\ell^m = \sum_{\ell=0}^{\infty}\sum_{m=-\ell}^{\ell} g_\ell^m\mathrm{Y}_\ell^m\,, \end{aligned} \tag{A.28}$$

and we obtain

$$\mathsf{L}_\ell\, w_\ell^m = h_\ell^m \quad , \quad \text{with } h_\ell^m = r\,g_\ell^m\,.$$

The outgoing-ness of u, given by the outgoing resolvent, means that modal solutions w_ℓ^m are regular (i.e. it satisfies (4.13)) at $r=0$ and inherits the outgoing condition (4.14). This also implies it is given by the outgoing modal Green kernel G_ℓ (4.17),

$$w_\ell^m = \int_0^\infty G_\ell^m(r,\tilde r)\,h_\ell^m(\tilde r)\,\mathrm{d}\tilde r\,.$$

Injecting this gives,

$$\begin{aligned} u(\mathbf{x}) &= \frac{1}{|\mathbf{x}|}\sum_{\ell=0}^{\infty}\sum_{m=-\ell}^{\ell}\left(\int_0^{\infty} G_\ell^m(r,\tilde{r})\, h_\ell^m(\tilde{r})\,\mathrm{d}\tilde{r}\right)\mathrm{Y}_\ell^m(\theta,\phi)\\ &= \frac{1}{|\mathbf{x}|}\sum_{\ell=0}^{\infty}\sum_{m=-\ell}^{\ell}\left(\int_0^{\infty} G_\ell^m(r,\tilde{r})\,\left(\int_0^{\pi}\int_0^{2\pi}\tilde{r}\, g(\mathbf{y})\overline{\mathrm{Y}_\ell^m}(\tilde{\theta},\tilde{\phi})\,\sin\tilde{\theta}\, d\tilde{\phi}\, d\tilde{\theta}\right)\mathrm{d}\tilde{r}\right)\mathrm{Y}_\ell^m(\theta,\phi)\\ &= \int_{\mathbb{R}^3_{\mathbf{y}}}\left(\sum_{\ell=0}^{\infty}\sum_{m=-\ell}^{\ell}\frac{G_\ell^m(|\mathbf{x}|,|\mathbf{y}|)}{|\mathbf{x}|\,|\mathbf{y}|}\,\overline{\mathrm{Y}_\ell^m}(\theta_{\mathbf{y}},\phi_{\mathbf{y}})\,\mathrm{Y}_\ell^m(\theta_{\mathbf{x}},\phi_{\mathbf{x}})\right) g(\mathbf{y})\, d\mathbf{y} \end{aligned}$$

The second form of G comes from the property of the spherical harmonics, cf. [11, 2.29],

$$\sum_{m=-\ell}^{\ell}\mathrm{Y}_\ell^m(\theta_{\mathbf{x}},\phi_{\mathbf{x}})\,\overline{\mathrm{Y}_\ell^m(\theta_{\mathbf{y}},\phi_{\mathbf{y}})} \;=\; \frac{2\ell+1}{4\pi}\mathrm{P}_\ell(\cos\theta_{\mathbf{x}\cdot\mathbf{y}})\,. \tag{A.29}$$

For an L^2_{loc}, it suffices to have the definition off a set of measure zero. However, we can define the value of G for these values.

Source on z-axis but not at the origin For $\mathbf{y}_0$ on the z-axis but not the origin

$$G(\mathbf{x}\,,\,\mathbf{y}_0) \;:=\; \lim_{\epsilon\to 0^+}\frac{1}{2\pi\epsilon}\int_{C_\epsilon} G(\mathbf{x}\,,\,\mathbf{z})\;\mathrm{d}\sigma(\mathbf{z})\,, \tag{A.30}$$

where C_ϵ is the circle formed by the intersection of sphere of radius of $|\mathbf{y}|$ and the cylinder of radius ϵ aligned along the z-axis,

$$C_\epsilon \;:=\; \{\mathbf{x}\in\mathbb{R}^3 | |\mathbf{x}| = |\mathbf{y}_0|\}\;\bigcap\;\{\mathbf{x} = (x,y,z)\in\mathbb{R}^3 | x^2+y^2=\epsilon^2\}\,.$$

We consider the surface integral

$$\begin{aligned} \frac{1}{2\pi\epsilon}\int_{C_\epsilon} G(\mathbf{x}\,,\,\mathbf{z})\;\mathrm{d}\sigma(\mathbf{z}) &= \frac{1}{2\pi}\sum_{\ell=0}^{\infty}\sum_{m=-\ell}^{\ell}\frac{G_\ell^m(|\mathbf{x}|,|\mathbf{z}|)}{|\mathbf{x}|\,|\mathbf{z}|}\;\mathrm{Y}_\ell^m(\theta_{\mathbf{x}},\phi_{\mathbf{x}})\int_0^{2\pi}\overline{\mathrm{Y}_\ell^m}(\theta_{\mathbf{z}},\phi_{\mathbf{z}})\;d\phi_{\mathbf{z}}\\ &= \sum_{\ell=0}^{\infty}\frac{G_\ell^0(|\mathbf{x}|,|\mathbf{z}|)}{|\mathbf{x}|\,|\mathbf{z}|}\;\mathrm{Y}_\ell^0(\theta_{\mathbf{x}},\phi_{\mathbf{x}})\mathrm{Y}_\ell^0(\theta_{\mathbf{z}})\,. \end{aligned} \tag{A.31}$$

Since

$$\int_0^{2\pi} e^{\mathrm{i}\,m\,\phi}d\phi \;=\; 2\pi\delta_{m0}\,, \tag{A.32}$$

taking the limit as $\epsilon\to 0^+$, we obtain, for $\mathbf{y}_0\neq(0,0,0)$ on the z-axis

$$\boxed{G(x,\mathbf{y}_0) \;=\; \sum_{\ell=0}^{\infty}\frac{G_\ell^0(|\mathbf{x}|,|\mathbf{y}_0|)}{|\mathbf{x}|\,|\mathbf{y}_0|}\;\mathrm{Y}_\ell^0(\theta_{\mathbf{x}})\;\mathrm{Y}_\ell^0(0)\,.} \tag{A.33}$$

Source at the origin For $\mathbf{y}=(0,0,0)$, define

$$G(\mathbf{x}\,,\,\mathbf{y}_0) \;:=\; \lim_{\epsilon\to 0^+}\frac{1}{4\pi\epsilon^2}\int_{\mathbb{S}(0,\epsilon)} G(\mathbf{x}\,,\,\mathbf{z})\;\mathrm{d}\sigma(\mathbf{z})$$

We first simplify the integrand in the limit,

$$\begin{aligned}
\frac{1}{4\pi\epsilon^2}\int_{\mathbb{S}(0,\epsilon)} G(\mathbf{x}\,,\,\mathbf{z})\,\mathrm{d}\sigma(\mathbf{z}) &= \frac{1}{4\pi}\sum_{\ell=0}^{\infty}\sum_{m=-\ell}^{\ell}\frac{G_\ell^m(|\mathbf{x}|,\epsilon)}{|\mathbf{x}|\,\epsilon}\;\mathrm{Y}_\ell^m(\theta_{\mathbf{x}},\phi_{\mathbf{x}})\int_0^{\pi}\int_0^{2\pi}\overline{\mathrm{Y}_\ell^m}(\theta_{\mathbf{z}},\phi_{\mathbf{z}})\,\sin\theta_{\mathbf{z}}\,\mathrm{d}\phi_{\mathbf{z}}\,\mathrm{d}\theta_{\mathbf{z}} \\
&= \frac{1}{4\pi}\frac{G_0^0(|\mathbf{x}|,\epsilon)}{|\mathbf{x}|\,\epsilon} \\
\Rightarrow \quad G(\mathbf{x}\,,\,0) \;:=&\; \frac{1}{4\pi}\frac{1}{|\mathbf{x}|}\lim_{\epsilon\to 0^+} G_0^0(|\mathbf{x}|,\epsilon)\,.
\end{aligned} \tag{A.34}$$

On the other hand, for $\epsilon > 0$, $G_0^0(|\mathbf{x}|,\epsilon)$ is the outgoing distributional solution of,

$$\mathsf{L}_0\,G_0 \;=\; \delta(r-\epsilon) \quad , \quad \epsilon > 0\,.$$

and thus is given by,

$$G_0(r,s) \;=\; -\mathsf{H}(s-r)\;\tilde{\psi}_0(r)\;\frac{\psi_0(s)}{\mathcal{W}(s)} \;-\; \mathsf{H}(r-s))\;\psi_0(r)\;\frac{\tilde{\psi}_0(s)}{\mathcal{W}(s)}\,. \tag{A.35}$$

Here $\mathcal{W}(s) := \mathcal{W}\{\psi(s),\tilde{\psi}(s)\}$, the Wronskian. Note indicial roots of the equation is 0 and 1. The choice of ψ_0 is modulo a constant multiple. We can choose[9] ψ_0 so that (without changing the overall G_0^0)

$$\lim_{s\to 0}\frac{\tilde{\psi}_0(s)}{\mathcal{W}(s)} \;=\; -1\,. \tag{A.37}$$

The choice leads to,

$$\lim_{r>\epsilon,\epsilon\to 0^+} G_0(r\,,\,\epsilon) \;=\; \psi_0(r)\,.$$

In this way, we have reconciled with the direct method[10] to obtain G when $\mathbf{y} = (0,0,0)$.

A.3 Other variants of the modal Green functions

Variants independent on m As introduced in Section 4, we work with the modal Green function G_ℓ^m cf. (4.12) associated to operator L_ℓ (4.10) which does not depend on the index m,

$$\left(-\frac{d^2}{dr^2} \;+\; \frac{Q(r)}{r^2}\right)G_\ell \;=\; \delta(r-s)\,. \tag{A.38}$$

For this reason, we also write G_ℓ^m simply as G_ℓ,

$$G_\ell^m(r,s) \;=\; G_\ell(r,s)\,. \tag{A.39}$$

---

[9] With choice of $\tilde{\psi}_0$ fixed, consider $\psi_0 \;=\; d\,y_{\mathrm{reg}}$ where y_{reg} is a fixed regular homogeneous solution on $(0,\infty)$, and d a constant to be determined. For all nonzero d, using $\{\tilde{\psi}_0, dy_2\}$ in (A.35) gives the same expression of G_0^0, since $\mathcal{W}\{d\,y_{\mathrm{reg}}\,,\,\tilde{\psi}_0\} \;=\; d\,\mathcal{W}\{y_{\mathrm{reg}}\,,\tilde{\psi}_0\}$. We next choose d so that

$$\lim_{s\to 0}\frac{\tilde{\psi}_0(s)}{\mathcal{W}\{d\,y_{\mathrm{reg}}(s)\,,\,\tilde{\psi}_0(s)\}} \;=\; -1\,. \tag{A.36}$$

[10] In the latter approach, one starts with the equation 3D, $\left(-\Delta - \frac{\sigma^2(r)}{\mathfrak{c}^2(r)} + \mathsf{q}(r)\right)\Phi \;=\; \delta(x)$. Since Φ only has radial dependence, we look for $\Phi(\mathbf{x})$ of the form $\Phi(\mathbf{x}) \;=\; \frac{g(r)}{r}$ which solves $\left(-\frac{d}{dr^2} - \frac{\sigma^2(r)}{\mathfrak{c}^2(r)} + \mathsf{q}\right)g \;=\; \delta(r)$. Choose $g = \tilde{\psi}_0$, where $\tilde{\psi}_0$ an outgoing solution to L_0 on $(0,\infty)$.

One can also work with the unreduced unknown (employed in the HDG pre-formulation) $\tilde{G}_\ell = \frac{G_\ell}{r}$, which solves[11]

$$\left(-\frac{d^2}{dr^2} \;-\; \frac{2}{r}\frac{d}{dr} \;+\; \frac{Q(r)}{r^2}\right)\tilde{G}_\ell \;=\; \frac{1}{r}\delta(r-s) \tag{A.40a}$$

$$\Leftrightarrow \quad \left(-r^2\frac{d^2}{dr^2} \;-\; 2r\,\frac{d}{dr} \;+\; Q(r)\right)\tilde{G}_\ell \;=\; r\,\delta(r-s)\,. \tag{A.40b}$$

We also note the variant $\tilde{\tilde{G}}_\ell = \dfrac{G_\ell}{rs}$ which solves[12]

$$\left(-\frac{d^2}{dr^2} \;-\; \frac{2}{r}\frac{d}{dr} \;-\; \frac{Q(r)}{r^2}\right)\tilde{\tilde{G}}_\ell \;=\; \frac{1}{r\,s}\delta(r-s) \tag{A.41a}$$

$$\Leftrightarrow \quad \left(-\frac{d^2}{dr^2} \;-\; \frac{2}{r}\frac{d}{dr} \;-\; \frac{Q(r)}{r^2}\right)\tilde{\tilde{G}}_\ell \;=\; \frac{1}{r^2}\delta(r-s) \tag{A.41b}$$

$$\Leftrightarrow \quad \left(-r^2\frac{d^2}{dr^2} \;-\; 2r\frac{d}{dr} \;-\; Q(r)\right)\tilde{\tilde{G}}_\ell^m \;=\; \delta(r-s)\,. \tag{A.41c}$$

Variants dependent on m In applications, one usually works with a fixed source, and hence rather than considering $G(r,s)$ as a Schwartz kernel, one considers it as a function of receptor's position. In particular, for a fixed source $\mathbf{s}$, G is a function $\mathbf{x} \mapsto G(\mathbf{x},\mathbf{s})$ with $\mathbf{s}$ being a parameter, and expansion (4.11) gives the harmonic expansion,

$$G(\mathbf{x}\,,\,\mathbf{s}) \;=\; \sum_{\ell=0}^{\infty}\sum_{m=-\ell}^{\ell}\left(\frac{G_\ell(|\mathbf{x}|\,,|\,\mathbf{s}|)}{|\mathbf{x}|}\,\frac{\overline{\mathrm{Y}_\ell^m(\hat{\mathbf{s}})}}{|\mathbf{s}|}\right)\mathrm{Y}_\ell^m(\hat{\mathbf{x}}) \quad , \quad \text{for } \mathbf{x},\mathbf{s} \text{ not on the z-axis}\,. \tag{A.42}$$

In this perspective, one can work with the <u>scaled modal</u> Green function

$$r \;\mapsto\; \mathfrak{G}_\ell^m(r,s) \quad , \quad \text{with } s := |\mathbf{s}| \tag{A.43}$$

which solves

$$\left(-\frac{d^2}{dr^2} \;-\; \frac{Q(r)}{r^2}\right)\mathfrak{G}_\ell^m \;=\; \mathrm{Y}_\ell^m(\mathbf{s})\,\delta(r-s) \quad , \quad s := |\mathbf{s}|\,. \tag{A.44}$$

Equivalently, one can work with the <u>reduced scaled modal</u> Green function

$$r \;\mapsto\; \tilde{\mathfrak{G}}_\ell^m(\cdot,s) \quad , \quad s := |\mathbf{s}| \tag{A.45}$$

which solves

$$\begin{aligned} &\left(-\frac{d^2}{dr^2} \;-\; \frac{2}{r}\frac{d}{dr} \;+\; \frac{Q(r)}{r^2}\right)\tilde{\mathfrak{G}}_\ell^m = \frac{\mathrm{Y}_\ell^m(\hat{\mathbf{s}})}{s}\,\delta(r-s)\,; \\ \Leftrightarrow &\left(-\frac{d^2}{dr^2} \;-\; \frac{2}{r}\frac{d}{dr} \;+\; \frac{Q(r)}{r^2}\right)\tilde{\mathfrak{G}}_\ell^m = \frac{\mathrm{Y}_\ell^m(\hat{\mathbf{s}})}{r}\,\delta(r-s)\,; \end{aligned} \tag{A.46}$$

---

[11] This can be seen as follows. Replace G_ℓ in its ODE by $r\tilde{G}_\ell$, substitute in the ODE satisfied by G_ℓ(A.38)

$$-\frac{d^2}{dr^2}\,(r\,\tilde{G}_\ell) \;-\; \frac{Q(r)}{r^2}(r\tilde{G}_\ell) \;=\; \delta(r-s) \quad \Leftrightarrow \quad -r\frac{d}{dr}\tilde{G}_\ell \;-\; 2\frac{d}{dr}\tilde{G}_\ell \;-\; \frac{Q(r)}{r^2}(r\tilde{G}_\ell) \;=\; \delta(r-s)$$

$$\Rightarrow -\frac{d^2}{dr^2}\tilde{G}_\ell \;-\; \frac{2}{r}\frac{d}{dr}\tilde{G}_\ell \;-\; \frac{Q(r)}{r^2}\tilde{G}_\ell \;=\; \frac{1}{r}\delta(r-s)\,.$$

[12] Replace G_ℓ^m in its ODE by $rs\tilde{\tilde{G}}_\ell$, substitute in the ODE satisfied by G_ℓ (A.38),

$$-\frac{d^2}{dr^2}(r\,s\,\tilde{\tilde{G}}_\ell) \;-\; \frac{Q(r)}{r^2}(r\,s\,\tilde{\tilde{G}}_\ell) \;=\; \delta(r-s) \quad \Leftrightarrow \quad -r\,s\,\frac{d^2}{dr^2}\tilde{\tilde{G}}_\ell \;-\; 2\,s\,\frac{d}{dr}\tilde{\tilde{G}}_\ell^m \;-\; \frac{Q(r)}{r^2}(rs\tilde{\tilde{G}}_\ell^m) \;=\; \delta(r-s)$$

$$\Rightarrow -\frac{d^2}{dr^2}\tilde{\tilde{G}}_\ell \;-\; \frac{2}{r}\frac{d}{dr}\tilde{\tilde{G}}_\ell \;-\; \frac{Q(r)}{r^2}\tilde{\tilde{G}}_\ell \;=\; \frac{1}{r\,s}\delta(r-s)\,.$$

An equivalent form of (A.46) more convenient for numerical discretization is

$$\begin{aligned} &\left(-r^2\frac{d^2}{dr^2} \;-\; 2r\,\frac{d}{dr} \;+\; Q(r)\right)\,\tilde{\mathfrak{G}}_\ell^m \;=\; r\,\mathrm{Y}_\ell^m(\hat{\mathbf{s}})\,\delta(r-s)\,; \\ \Leftrightarrow\;&\left(-r^2\frac{d^2}{dr^2} \;-\; 2r\,\frac{d}{dr} \;+\; Q(r)\right)\,\tilde{\mathfrak{G}}_\ell^m \;=\; s\,\mathrm{Y}_\ell^m(\hat{\mathbf{s}})\,\delta(r-s)\,. \end{aligned} \tag{A.47}$$

Note that $r^2 d_r^2 - 2r\,dr$ is also written as $d_r r^2 d_r$. We also have the variant $\tilde{\tilde{\mathfrak{G}}}_\ell^m$ which solves

$$\left(-\frac{d^2}{dr^2} \;-\; \frac{2}{r}\,\frac{d}{dr} \;-\; \frac{Q(r)}{r^2}\right)\tilde{\tilde{\mathfrak{G}}}_\ell^m \;=\; \frac{1}{r\,s}\mathrm{Y}_\ell^m(\hat{\mathbf{s}})\,\delta(r-s) \tag{A.48a}$$

$$\Leftrightarrow\quad\left(-\frac{d^2}{dr^2} \;-\; \frac{2}{r}\,\frac{d}{dr} \;-\; \frac{Q(r)}{r^2}\right)\tilde{\tilde{\mathfrak{G}}}_\ell^m \;=\; \frac{1}{r^2}\mathrm{Y}_\ell^m(\hat{\mathbf{s}})\,\delta(r-s) \tag{A.48b}$$

$$\Leftrightarrow\quad\left(-r^2\frac{d^2}{dr^2} \;-\; 2r\frac{d}{dr} \;-\; Q(r)\right)\tilde{\tilde{\mathfrak{G}}}_\ell^m \;=\; \mathrm{Y}_\ell^m(\hat{\mathbf{s}})\,\delta(r-s)\,. \tag{A.48c}$$

Unlike $G_\ell, \tilde{G}_\ell$ and $\tilde{\tilde{G}}_\ell$ which do not depend on m, $\mathfrak{G}_\ell^m$,$\tilde{\mathfrak{G}}_\ell^m$ and $\tilde{\tilde{\mathfrak{G}}}$ do. We give a list of summary of their relations,

$$G_\ell^m(r,s) \;=\; G_\ell(r,s) \quad;\quad \tilde{G}_\ell^m(r,s) \;=\; \frac{G_\ell^m(r,s)}{r} \quad;\quad \tilde{\tilde{G}}_\ell^m(r,s) \;=\; \frac{G_\ell^m(r,s)}{r\,s}\,; \tag{A.49a}$$

$$\mathfrak{G}_\ell^m(r,s) \;=\; \overline{\mathrm{Y}_\ell^m(\hat{\mathbf{s}})}\,G_\ell^m(r,s) \quad,\quad \tilde{\mathfrak{G}}_\ell^m(r,s) \;=\; \frac{\mathfrak{G}_\ell^m(r,s)}{r} \;=\; \overline{\mathrm{Y}_\ell^m(\hat{\mathbf{s}})}\,\frac{G_\ell(r\,,\,s)}{r}\,; \tag{A.49b}$$

$$\tilde{\tilde{\mathfrak{G}}}_\ell^m(r,s) \;=\; \frac{\mathfrak{G}_\ell^m(r,s)}{r\,s} \;=\; \overline{\mathrm{Y}_\ell^m(\hat{\mathbf{s}})}\,\frac{G_\ell(r\,,\,s)}{r\,s} \tag{A.49c}$$

Corresponding harmonic expansions In terms of these modal kernels, the harmonic expansion of the 3D Green kernel G, for $\mathbf{x}$ and $\mathbf{y}$ not on the z-axis, is

$$G(\mathbf{x},\mathbf{y}) \;=\; \frac{1}{|\mathbf{x}|\,|\mathbf{y}|}\sum_{\ell=0}^{\infty}\sum_{m=-\ell}^{\ell} G_\ell^m(|\mathbf{x}|\,,|\,\mathbf{y}|)\;\mathrm{Y}_\ell^m(\hat{\mathbf{x}})\;\overline{\mathrm{Y}_\ell^m(\hat{\mathbf{y}})} \;\overset{(2.27)}{=}\; \frac{1}{|\mathbf{x}|\,|\mathbf{y}|}\sum_{\ell=0}^{\infty} G_\ell(|\mathbf{x}|\,,|\,\mathbf{y}|)\;\frac{(2\ell+1)}{4\pi}\mathrm{P}_\ell(\cos\theta_{\mathbf{x}\cdot\mathbf{y}}) \tag{A.50a}$$

$$=\; \frac{1}{|\mathbf{y}|}\sum_{\ell=0}^{\infty}\sum_{m=-\ell}^{\ell} \tilde{G}_\ell^m(|\mathbf{x}|\,,|\,\mathbf{y}|)\;\mathrm{Y}_\ell^m(\hat{\mathbf{x}})\;\overline{\mathrm{Y}_\ell^m(\hat{\mathbf{y}})} \;=\; \frac{1}{|\mathbf{y}|}\sum_{\ell=0}^{\infty} \tilde{G}_\ell(|\mathbf{x}|\,,|\,\mathbf{y}|)\;\frac{(2\ell+1)}{4\pi}\mathrm{P}_\ell(\cos\theta_{\mathbf{x}\cdot\mathbf{y}}) \tag{A.50b}$$

$$=\; \sum_{\ell=0}^{\infty}\sum_{m=-\ell}^{\ell} \tilde{\tilde{G}}_\ell^m(|\mathbf{x}|\,,|\,\mathbf{y}|)\;\mathrm{Y}_\ell^m(\hat{\mathbf{x}})\;\overline{\mathrm{Y}_\ell^m(\hat{\mathbf{y}})} \;=\; \sum_{\ell=0}^{\infty} \tilde{\tilde{G}}_\ell(|\mathbf{x}|\,,|\,\mathbf{y}|)\;\frac{(2\ell+1)}{4\pi}\mathrm{P}_\ell(\cos\theta_{\mathbf{x}\cdot\mathbf{y}}) \tag{A.50c}$$

where $\theta_{\mathbf{x}\cdot\mathbf{y}}$ is the angle between $\mathbf{x}$ and $\mathbf{y}$, i.e.

$$\cos\theta_{\mathbf{x}\cdot\mathbf{y}} \;=\; \frac{\mathbf{x}\cdot\mathbf{y}}{|\mathbf{x}|\,|\mathbf{y}|}\,. \tag{A.51}$$

Using the scaled version, the harmonic expansion of $G(\mathbf{x},\mathbf{y})$ takes the form,

$$\begin{aligned} G(\mathbf{x},\mathbf{y}) &= \frac{1}{|\mathbf{x}|\,|\mathbf{y}|}\sum_{\ell=0}^{\infty}\sum_{m=-\ell}^{\ell} \mathfrak{G}_\ell^m(|\mathbf{x}|\,,|\,\mathbf{y}|)\ \mathrm{Y}_\ell^m(\hat{\mathbf{x}}) && \text{(A.52a)}\\ &= \frac{1}{|\mathbf{y}|}\sum_{\ell=0}^{\infty}\sum_{m=-\ell}^{\ell} \tilde{\mathfrak{G}}_\ell^m(|\mathbf{x}|\,,|\,\mathbf{y}|)\ \mathrm{Y}_\ell^m(\hat{\mathbf{x}}) && \text{(A.52b)}\\ &= \sum_{\ell=0}^{\infty}\sum_{m=-\ell}^{\ell} \tilde{\tilde{\mathfrak{G}}}_\ell^m(|\mathbf{x}|\,,|\,\mathbf{y}|)\ \mathrm{Y}_\ell^m(\hat{\mathbf{x}})\,. && \text{(A.52c)} \end{aligned}$$

When $\mathbf{y}$ is on the z-axis, then only the mode with $m \neq 0$ are involved in both (A.52) and (A.50). This affects the expressions (A.52) using the scaled modal kernel more, since in (A.50) the expression using P_ℓ is applicable despite the position of $\mathbf{y}$,

$$\begin{aligned} G(\mathbf{x},\mathbf{y}) &= \frac{1}{|\mathbf{x}|\,|\mathbf{y}|}\sum_{\ell=0}^{\infty} \mathfrak{G}_\ell^0(|\mathbf{x}|\,,|\,\mathbf{y}|)\ \mathrm{Y}_\ell^0(\hat{\mathbf{x}}) && \text{(A.53a)}\\ &= \frac{1}{|\mathbf{y}|}\sum_{\ell=0}^{\infty} \tilde{\mathfrak{G}}_\ell^0(|\mathbf{x}|\,,|\,\mathbf{y}|)\ \mathrm{Y}_\ell^0(\hat{\mathbf{x}}) && \text{(A.53b)}\\ &= \sum_{\ell=0}^{\infty} \tilde{\tilde{\mathfrak{G}}}_\ell^0(|\mathbf{x}|\,,|\,\mathbf{y}|)\ \mathrm{Y}_\ell^0(\hat{\mathbf{x}})\,. && \text{(A.53c)} \end{aligned}$$

B Further remarks on Whittaker functions

B.1 Connection formula for Whittaker functions

Connection formula for Whittaker M The identity for the derivative of M can be obtained from [28] as follows. From [28, Eq. (13.15.15)], we have

$$\frac{d^n}{dz^n}\left(e^{\frac{1}{2}z}\, z^{\mu-\frac{1}{2}}\, \mathrm{M}_{\kappa,\mu}(z)\right) \;=\; (-1)^n(-2\mu)_n\, e^{\frac{1}{2}z}\, z^{\mu-\frac{1}{2}(n+1)}\, \mathrm{M}_{\kappa-\frac{1}{2}n,\mu-\frac{1}{2}n}(z)\,. \tag{B.1}$$

Take $n=1$ and $\mu=\ell+1/2$ in (B.1). The left-hand-side is

$$\frac{d}{dz}\left(e^{\frac{1}{2}z}\, z^{\ell}\, \mathrm{M}_{\kappa,\ell+1/2}(z)\right) \;=\; \frac{1}{2}e^{\frac{1}{2}z}\, z^{\ell}\, \mathrm{M}_{\kappa,\ell+1/2}(z) \;+\; \ell e^{\frac{1}{2}z}\, z^{\ell-1}\, \mathrm{M}_{\kappa,\ell+1/2}(z) \;+\; e^{\frac{1}{2}z}\, z^{\ell}\, \frac{d}{dz}\mathrm{M}_{\kappa,\ell+1/2}(z)\,. \tag{B.2}$$

Using the definition $(a)_n = \dfrac{\Gamma(a+n)}{\Gamma(a)}$ identity $(-a)_n = (-1)^n(a-n+1)_n$, cf. [28, Eq. (5.2.6)],

$$\begin{aligned} \Big(-2\big(\ell+\tfrac{1}{2}\big)\Big)_1 \;=\; \Big(-2\ell-1\Big)_1 \;=\; (-1)((2\ell+1)-1+1)_1 \;=\; -(2\ell+1)_1 \;=\; -\frac{\Gamma(2\ell+2)}{\Gamma(2\ell+1)}\\ =-\frac{(2\ell+1)!}{(2\ell)!} = -(2\ell+1). \end{aligned} \tag{B.3}$$

The right-hand side is

$$(-1)(-2\big(\ell+\tfrac{1}{2}\big))_1\, e^{\frac{1}{2}z}\, z^{\ell+\frac{1}{2}-\frac{1}{2}(1+1)}\, \mathrm{M}_{\kappa-\frac{1}{2},\ell+1/2-\frac{1}{2}}(z) \;=\; (2\ell+1)e^{\frac{1}{2}z}\, z^{\ell-1/2}\, \mathrm{M}_{\kappa-\frac{1}{2},\ell}(z). \tag{B.4}$$

By dividing both sides (i.e. (B.2) and (B.4)) by $e^{\frac{1}{2}z}z^{\ell}$, we obtain

$$\frac{1}{2}\,\mathrm{M}_{\kappa,\ell+1/2}(z) \;+\; \frac{\ell}{z}\,\mathrm{M}_{\kappa,\ell+1/2}(z) \;+\; \frac{d}{dz}\mathrm{M}_{\kappa,\ell+1/2}(z) \;=\; \frac{(2\ell+1)}{\sqrt{z}}\,\mathrm{M}_{\kappa-\frac{1}{2},\ell}(z), \tag{B.5}$$

which can be written as

$$\frac{d}{dz}\mathrm{M}_{\kappa,\ell+1/2}(z) \;=\; -\left(\frac{1}{2} \;+\; \frac{\ell}{z}\right)\,\mathrm{M}_{\kappa,\ell+1/2}(z) + \frac{(2\ell+1)}{\sqrt{z}}\,\mathrm{M}_{\kappa-\frac{1}{2},\ell}(z). \tag{B.6}$$

Connection formula for Whittaker $\mathcal{M}$ One can obtain the identity for $\mathcal{M}$ by dividing both sides by $\Gamma(2\ell+2)$

$$\mathcal{M}'_{\kappa,\ell+1/2}(z) \;=\; \left(-\frac{1}{2} \;-\; \frac{\ell}{z}\right)\mathcal{M}_{\kappa,\ell+1/2}(z) \;+\; \frac{(2\ell+1)}{\sqrt{z}}\,\frac{\Gamma(2\ell+1)}{\Gamma(2\ell+2)}\,\mathcal{M}_{\kappa-\frac{1}{2},\ell}(z).$$

Using the identity that $\Gamma(2\ell+2) = (2\ell+1)\,\Gamma(2\ell+1)$, the right-hand side further simplifies as

$$\mathcal{M}'_{\kappa,\ell+1/2}(z) \;=\; \left(-\frac{1}{2} \;-\; \frac{\ell}{z}\right)\mathcal{M}_{\kappa,\ell+1/2}(z) \;+\; \frac{1}{\sqrt{z}}\,\mathcal{M}_{\kappa-\frac{1}{2},\ell}(z). \tag{B.7}$$

Connection formula for Whittaker W We start from [28, Eq. (13.15.25)], with one-time differentiation,

$$\frac{d}{dz}\left(e^{-\frac{1}{2}z}\,z^{\mu-\frac{1}{2}}\,\mathrm{W}_{\kappa,\mu}(z)\right) \;=\; -e^{-\frac{1}{2}z}\,z^{\mu-1}\,\mathrm{W}_{\kappa+\frac{1}{2},\mu-\frac{1}{2}}(z)\,. \tag{B.8}$$

The left-hand-side gives

$$e^{-\frac{1}{2}z}z^{\mu-\frac{1}{2}}\left(\left(-\frac{1}{2} \;+\; \frac{\mu-\frac{1}{2}}{z}\right)\mathrm{W}_{\kappa,\mu}(z) \;+\; \mathrm{W}'_{\kappa,\mu}(z)\right) \tag{B.9}$$

Put this expression back into (B.8) and divide both sides by $e^{-\frac{1}{2}z}z^{\mu-\frac{1}{2}}$

$$\left(-\frac{1}{2} \;+\; \frac{\mu-\frac{1}{2}}{z}\right)\mathrm{W}_{\kappa,\mu}(z) \;+\; \mathrm{W}'_{\kappa,\mu}(z) \;=\; -\frac{1}{\sqrt{z}}\,\mathrm{W}_{\kappa+\frac{1}{2},\mu-\frac{1}{2}}(z)\,. \tag{B.10}$$

After rearrangement, we obtain

$$\boxed{\mathrm{W}'_{\kappa,\mu}(z) \;=\; \left(\frac{1}{2} \;-\; \frac{\mu-\frac{1}{2}}{z}\right)\mathrm{W}_{\kappa,\mu}(z) \;-\; \frac{1}{\sqrt{z}}\,\mathrm{W}_{\kappa+\frac{1}{2},\mu-\frac{1}{2}}(z)\,.} \tag{B.11}$$

We can also start from [28, Eq. (13.15.26)], with one-time differentiation,

$$z\,\frac{d}{z}\,z\left(e^{-\frac{1}{2}z}\,z^{\kappa-1}\,\mathrm{W}_{\kappa,\mu}(z)\right) \;=\; -e^{-\frac{1}{2}z}\,z^{\kappa}\,\mathrm{W}_{\kappa+1,\mu}(z)\,. \tag{B.12}$$

The left-hand-side gives

$$\begin{aligned} &z\,e^{-\frac{1}{2}z}\,z^{\kappa-1}\left(\left(1 \;-\; \frac{z}{2} + (\kappa-1)\right)\mathrm{W}_{\kappa,\mu}(z) \;+\; z\,\mathrm{W}'_{\kappa,\mu}(z)\right)\\ &= \; e^{-\frac{1}{2}z}\,z^{\kappa}\left(\left(\kappa \;-\; \frac{z}{2}\right)\mathrm{W}_{\kappa,\mu}(z) \;+\; z\,\mathrm{W}'_{\kappa,\mu}(z)\right) \end{aligned} \tag{B.13}$$

Put this back into (B.12) and divide both sides by $e^{-\frac{1}{2}z}\,z^{\kappa}$

$$\left(\kappa \;-\; \frac{z}{2}\right)\mathrm{W}_{\kappa,\mu}(z) \;+\; z\,\mathrm{W}'_{\kappa,\mu}(z) \;=\; -\,\mathrm{W}_{\kappa+1,\mu}(z)\,. \tag{B.14}$$

After rearrangement and divide both sides by z, we obtain

$$\boxed{\mathrm{W}'_{\kappa,\mu}(z) \;=\; \left(\frac{1}{2} \;-\; \frac{\kappa}{z}\right)\mathrm{W}_{\kappa,\mu}(z) \;-\; \frac{1}{z}\mathrm{W}_{\kappa+1,\mu}(z)} \tag{B.15}$$

B.2 Relation to Bessel functions

Following [23, p.305], the Whittaker functions are related to the Bessel functions by

$$\begin{aligned}
\mathrm{M}_{0,\mu}(\mathrm{i}\,\tilde{z}) \;&=\; \Gamma(1+\mu)\,2^{2\mu}\,e^{-\mathrm{i}\frac{\pi}{4}(2\mu-1)}\,\tilde{z}^{1/2}\,\mathrm{J}_{\mu}(-\frac{\tilde{z}}{2})\,;\\
\mathrm{W}_{0,\mu}(\mathrm{i}\,\tilde{z}) \;&=\; \frac{\sqrt{\pi}}{2}\;\tilde{z}^{\frac{1}{2}}\;e^{-\mathrm{i}\frac{\pi}{4}(1+2\mu)}\;\mathrm{H}^{(2)}_{\mu}\left(\frac{\tilde{z}}{2}\right)\;;\\
\mathrm{W}_{0,\mu}(-\mathrm{i}\,\tilde{z}) \;&=\; \frac{\sqrt{\pi}}{2}\;\tilde{z}^{\frac{1}{2}}\;e^{\mathrm{i}\frac{\pi}{4}(1+2\mu)}\;\mathrm{H}^{(1)}_{\mu}\left(\frac{\tilde{z}}{2}\right)\;.
\end{aligned} \tag{B.16}$$

The spherical Bessel functions z_ℓ are solutions to

$$\left(-\frac{d^2}{dz^2}\;-\;\frac{2}{z}\frac{d}{dz}\;-\;1\;+\;\frac{\ell(\ell+1)}{z^2}\right)\mathrm{z}_\ell\;=\;0\,, \tag{B.17}$$

while general Bessel functions Z_ν are solutions to

$$\left(-\frac{d^2}{dz^2}\;-\;\frac{1}{z}\frac{d}{dz}\;-\;1\;+\;\frac{\nu}{z^2}\right)\mathrm{Z}_\nu=0. \tag{B.18}$$

The spherical Bessel functions of the first kind are denoted by j_ℓ, second y_ℓ and third $\mathrm{h}^{(1)}_\ell=\mathrm{j}_\ell+\mathrm{i}\mathrm{y}_\ell$ and $\mathrm{h}^{(2)}_\ell=\mathrm{j}_\ell-\mathrm{i}\mathrm{y}_\ell$, cf. [28, 10.47.3–10.47.6]

$$\begin{aligned}
\mathrm{j}_\ell(z) \;&=\; \sqrt{\frac{1}{2}\frac{\pi}{z}}\,\mathrm{J}_{\ell+\frac{1}{2}}(z) \;=\; (-1)^{\ell}\sqrt{\frac{1}{2}\frac{\pi}{z}}\,\mathrm{Y}_{-\ell-\frac{1}{2}}(z)\,;\\
\mathrm{h}^{(1)}_\ell(z) \;&=\; \sqrt{\frac{1}{2}\frac{\pi}{z}}\;\mathrm{H}^{(1)}_{\ell+\frac{1}{2}}(z)\,.
\end{aligned} \tag{B.19}$$

They can be defined explicitly, cf. [28, 10.49.1–10.49.7]. In particular, for a specifically defined series $a_k(\ell+\frac{1}{2})$ cf. [28, 10.49.1],

$$\mathrm{h}^{(1)}_\ell \;=\; e^{\mathrm{i}z}\sum_{k=0}^{\ell}\mathrm{i}^{k-\ell-1}\frac{a_k(\ell+\frac{1}{2})}{z^{k+1}}\,.$$

When $\tilde{z}:=2\,\mathsf{k}\,r$, and $\mu=\ell+\frac{1}{2}$, then

$$e^{-\mathrm{i}\frac{\pi}{4}(2\mu-1)}\;=\;e^{-\mathrm{i}\frac{\pi}{4}2\ell}\;=\;e^{-\mathrm{i}\frac{\pi}{2}\ell}\;=\;(-\mathrm{i})^{\ell}\quad,\quad e^{\pm\,\mathrm{i}\frac{\pi}{4}(1+2\mu)}\;=\;e^{\pm\,\mathrm{i}\frac{\pi}{2}(\ell+1)}$$

and (B.16) simplifies to

$$\begin{aligned}
\mathrm{M}_{0,\ell}(\mathrm{i}\,2\,\mathsf{k}\,r) \;&=\; \Gamma(\ell+\tfrac{3}{2})\,2^{2\ell+1}\,(-\mathrm{i})^{\ell}\,(2\,\mathsf{k}\,r)^{1/2}\;\mathrm{J}_{\ell+1/2}(-\mathsf{k}\,r)\\
&=\; \sqrt{\pi}\,\Gamma(\ell+\tfrac{3}{2})\,2^{2\ell+1}\,(-1)^{\ell}\,\mathrm{i}^{\ell+1}\,(2\,\mathsf{k}\,r)\;\mathrm{j}_\ell(-\mathsf{k}\,r)\\
&=\; \sqrt{\pi}\,\Gamma(\ell+\tfrac{3}{2})\,2^{2\ell+1}\,\mathrm{i}^{\ell+1}\,(2\,\mathsf{k}\,r)\;\mathrm{j}_\ell(\mathsf{k}\,r)\,.
\end{aligned} \tag{B.20}$$

In the last equation, we have also used $\mathrm{j}_n(z)=(-1)^n\mathrm{j}_n(z)$, cf. [28, 10.47.14]. The relation between the Whittaker W and the Bessel functions (B.16) simplifies to

$$\begin{aligned}
\mathrm{W}_{0,\ell+1/2}(\mathrm{i}\,2\,\mathsf{k}\,r) \;&=\; \frac{\sqrt{\pi}}{2}\;(2\,\mathsf{k}\,r)^{\frac{1}{2}}\;\mathrm{i}^{-\ell-1}\;\mathrm{H}^{(2)}_{\ell+\frac{1}{2}}\,(\mathsf{k}\,r)\;=\;\frac{\mathsf{k}\,r}{\mathrm{i}^{\ell+1}}\mathrm{h}^{(2)}_\ell(\mathsf{k}\,r)\,;\\
\mathrm{W}_{0,\ell+1/2}(-\mathrm{i}\,2\,\mathsf{k}\,r) \;&=\; \frac{\sqrt{\pi}}{2}\;(2\,\mathsf{k}\,r)^{\frac{1}{2}}\;\mathrm{i}^{\ell+1}\;\mathrm{H}^{(1)}_{\ell+\frac{1}{2}}\,(\mathsf{k}\,r)\;=\;\mathrm{i}^{\ell+1}\,\mathsf{k}\,r\,\mathrm{h}^{(1)}_\ell(\mathsf{k}\,r)\,.
\end{aligned} \tag{B.21}$$

References

[1] A. D. Agaltsov, T. Hohage, and R. G. Novikov, *Global uniqueness in a passive inverse problem of helioseismology*, arXiv e-prints, (2019).

[2] S. Agmon, M. Klein, et al., *Analyticity properties in scattering and spectral theory for Schrödinger operators with long-range radial potentials*, Duke Mathematical Journal, 68 (1992), pp. 337–399.

[3] H. Barucq, J. Chabassier, M. Duruflé, L. Gizon, and M. Leguèbe, *Atmospheric radiation boundary conditions for the Helmholtz equation*, ESAIM: Mathematical Modelling and Numerical Analysis, 52 (2018), pp. 945–964.

[4] H. Barucq, F. Faucher, and H. Pham, *Outgoing solutions to the scalar wave equation in helioseismology*, Research Report RR-9280, Inria Bordeaux Sud-Ouest ; Project-Team Magique3D, August 2019.

[5] ——, *Outgoing solutions adn radiation boundary conditions for the ideal atmospheric scalar wave equation in helioseismology*, ESAIM: Mathematical Modelling and Numerical Analysis, to appear (2020).

[6] V. G. Böning, M. Roth, W. Zima, A. C. Birch, and L. Gizon, *Sensitivity kernels for flows in time–distance helioseismology: Extension to spherical geometry*, The Astrophysical Journal, 824 (2016), p. 49.

[7] R. Burston, L. Gizon, and A. C. Birch, *Interpretation of helioseismic travel times*, Space Science Reviews, 196 (2015), pp. 201–219.

[8] J. Chabassier and M. Durufle, *High Order Finite Element Method for solving Convected Helmholtz equation in radial and axisymmetric domains. Application to Helioseismology*, Research Report RR-8893, Inria Bordeaux Sud-Ouest, Mar. 2016.

[9] J. Christensen-Dalsgaard, W. Däppen, S. Ajukov, E. Anderson, H. Antia, S. Basu, V. Baturin, G. Berthomieu, B. Chaboyer, S. Chitre, et al., *The current state of solar modeling*, Science, 272 (1996), pp. 1286–1292.

[10] E. A. Coddington, *An introduction to ordinary differential equations*, Dover Publisher, 1961.

[11] D. Colton and R. Kress, *Inverse acoustic and electromagnetic scattering theory*, vol. 93, Springer Science & Business Media, 2012.

[12] Y. C. de Verdiere, *Mathematical models for passive imaging I: general background*, arXiv e-prints, (2006), pp. math–ph/0610043.

[13] A. R. Edmonds, *Angular momentum in quantum mechanics*, (1960).

[14] D. Fournier, M. Leguèbe, C. S. Hanson, L. Gizon, H. Barucq, J. Chabassier, and M. Duruflé, *Atmospheric-radiation boundary conditions for high-frequency waves in time-distance helioseismology*, Astronomy & Astrophysics, 608 (2017), p. A109.

[15] L. Gizon, H. Barucq, M. Duruflé, C. S. Hanson, M. Leguèbe, A. C. Birch, J. Chabassier, D. Fournier, T. Hohage, and E. Papini, *Computational helioseismology in the frequency domain: acoustic waves in axisymmetric solar models with flows*, Astronomy & Astrophysics, 600 (2017), p. A35.

[16] L. Gizon and A. Birch, *Time-distance helioseismology: the forward problem for random distributed sources*, The Astrophysical Journal, 571 (2002), p. 966.

[17] L. Gizon and A. C. Birch, *Local helioseismology*, Living Reviews in Solar Physics, 2 (2005), p. 6.

[18] J. W. Harvey, F. Hill, R. P. Hubbard, J. R. Kennedy, J. W. Leibacher, J. A. Pintar, P. A. Gilman, R. W. Noyes, A. M. Title, J. Toomre, R. K. Ulrich, A. Bhatnagar, J. A. Kennewell, W. Marquette, J. Patron, O. Saa, and E. Yasukawa, *The Global Oscillation Network Group (GONG) Project*, Science, 272 (1996), pp. 1284–1286.

[19] F. Johansson, *Arb: efficient arbitrary-precision midpoint-radius interval arithmetic*, IEEE Transactions on Computers, 66 (2017), pp. 1281–1292.

[20] Z.-C. Liang, A. C. Birch, T. L. Duvall, L. Gizon, and J. Schou, *Comparison of acoustic travel-time measurements of solar meridional circulation from sdo/hmi and soho/mdi*, Astronomy & Astrophysics, 601 (2017), p. A46.

[21] Z.-C. Liang, L. Gizon, A. C. Birch, T. L. Duvall, and S. P. Rajaguru, *Solar meridional circulation from twenty-one years of SOHO/MDI and SDO/HMI observations. Helioseismic travel times and forward modeling in the ray approximation*, Astronomy & Astrophysics, 619 (2018), p. A99.

[22] P. Magain, *Contribution functions and the depths of formation of spectral lines*, Astronomy & Astrophysics, 163 (1986), pp. 135–139.

[23] W. Magnus, F. Oberhettinger, and R. P. Soni, *Formulas and theorems for the special functions of mathematical physics*, vol. 52, Springer Science & Business Media, 2013.

[24] K. Mandal, J. Bhattacharya, S. Halder, and S. M. Hanasoge, *Finite-frequency Sensitivity Kernels in Spherical Geometry for Time-Distance Helioseismology*, The Astrophysical Journal, 842 (2017), p. 89.

[25] P. Monk et al., *Finite element methods for Maxwell's equations*, Oxford University Press, 2003.

[26] K. Nagashima, D. Fournier, A. C. Birch, and L. Gizon, *The amplitude of the cross-covariance function of solar oscillations as a diagnostic tool for wave attenuation and geometrical spreading*, Astronomy & Astrophysics, 599 (2017), p. A111.

[27] K. Nagashima, B. Löptien, L. Gizon, A. C. Birch, R. Cameron, S. Couvidat, S. Danilovic, B. Fleck, and R. Stein, *Interpreting the helioseismic and magnetic imager (HMI) multi-height velocity measurements*, Solar Physics, 289 (2014), pp. 3457–3481.

[28] F. W. Olver, D. W. Lozier, R. F. Boisvert, and C. W. Clark, *NIST handbook of mathematical functions hardback and CD-ROM*, Cambridge University Press, 2010.

[29] A. D. Poularikas, *Transforms and applications handbook*, CRC press, 2010.

[30] C. S. Rosenthal, J. Christensen-Dalsgaard, Å. Nordlund, R. F. Stein, and R. Trampedach, *Convective contributions to the frequencies of solar oscillations*, Astronomy & Astrophysics, 351 (1999), pp. 689–700.

[31] P. H. Scherrer, R. S. Bogart, R. I. Bush, J. T. Hoeksema, A. G. Kosovichev, J. Schou, W. Rosenberg, L. Springer, T. D. Tarbell, A. Title, C. J. Wolfson, I. Zayer, and MDI Engineering Team, *The Solar Oscillations Investigation - Michelson Doppler Imager*, Solar Physics, 162 (1995), pp. 129–188.

[32] J. Schou, P. H. Scherrer, R. I. Bush, R. Wachter, S. Couvidat, M. C. Rabello-Soares, R. S. Bogart, J. T. Hoeksema, Y. Liu, T. L. Duvall, D. J. Akin, B. A. Allard, J. W. Miles, R. Rairden, R. A. Shine, T. D. Tarbell, A. M. Title, C. J. Wolfson, D. F. Elmore, A. A. Norton, and S. Tomczyk, *Design and Ground Calibration of the Helioseismic and Magnetic Imager (HMI) Instrument on the Solar Dynamics Observatory (SDO)*, Solar Physics, 275 (2012), pp. 229–259.

[33] R. Snieder, K. Mehta, M. Miyazawa, I. Vasconcelos, J. Sheiman, R. Calvert, A. Bakulin, and A. Venkataraman, *Applications of seismic interferometry to seismic field data*, Acoustical Society of America Journal, 121 (2007), pp. 3123–3123.

[34] J. E. Vernazza, E. H. Avrett, and R. Loeser, *Structure of the solar chromosphere. iii-models of the euv brightness components of the quiet-sun*, The Astrophysical Journal Supplement Series, 45 (1981), pp. 635–725.

[35] D. Yang, *Modeling experiments in helioseismic holography*, PhD thesis, The Goerg-August-Universität Göttingen, 2018.

[36] Y. D. Zhugzhda, J. Staude, and G. Bartling, *Spectral darkening functions of solar p-modes - an effective tool for helioseismology.*, Astronomy & Astrophysics, 305 (1996), p. L33.

RESEARCH CENTRE
BORDEAUX – SUD-OUEST

200 avenue de la Vieille Tour
33405 Talence Cedex

Publisher
Inria
Domaine de Voluceau - Rocquencourt
BP 105 - 78153 Le Chesnay Cedex
inria.fr

ISSN 0249-6399